

## ABSTRACT

Title of Dissertation:      **EXPERIMENTS WITH ULTRACOLD  
STRONTIUM IN COMPACT GRATING  
MAGNETO-OPTICAL TRAP GEOMETRIES**

**Ananya Sitaram  
Doctor of Philosophy, 2022**

Dissertation Directed by: **Dr. Gretchen K. Campbell  
Department of Physics**

In this thesis, we present the construction of a new apparatus for conducting experiments with ultracold strontium. The new apparatus is designed with a high-flux atomic source, a custom science chamber optimized for optical access, high-current Bitter electromagnets, and an updated computer control system. We discuss in depth the implementation of an insulated-gate bipolar transistor (IGBT) for fast current control of the magnetic field coils. We also present the design of JQI AutomatioN for Experiments (JANE): a programmable system on chip (PSoC)-based pseudoclock device that we use as the main clocking device for our experiments.

Next, we report the realization of the first magneto-optical trap (MOT) of an alkaline-earth atom with a tetrahedral trap geometry produced by a nanofabricated diffraction grating. We have demonstrated a broad-line MOT in bosonic  $^{88}\text{Sr}$  and fermionic  $^{87}\text{Sr}$ . We trap approximately  $4 \times 10^7$  atoms of  $^{88}\text{Sr}$  and achieve temperatures of around 6 mK,

with a trap lifetime of around 1 s.

Finally, we demonstrate sawtooth wave adiabatic passage (SWAP) in a narrow-line grating MOT of  $^{88}\text{Sr}$  atoms. In the narrow-line MOT, we trap approximately  $3 \times 10^6$  atoms, with an average temperature of  $3.4 \mu\text{K}$  and a trap lifetime of 0.77 s. We also discuss the possibility for a narrow-line grating MOT of the fermionic isotope. Our work with strontium grating MOTs is a step in the direction of compact quantum devices with alkaline-earth atoms.

EXPERIMENTS WITH  
ULTRACOLD STRONTIUM IN COMPACT  
GRATING MAGNETO-OPTICAL TRAP GEOMETRIES

by

Ananya Sitaram

Dissertation submitted to the Faculty of the Graduate School of the  
University of Maryland, College Park in partial fulfillment  
of the requirements for the degree of  
Doctor of Philosophy  
2022

Advisory Committee:

Professor Steven L. Rolston, Co-Chair  
Dr. Gretchen K. Campbell, Co-Chair/Advisor  
Professor Mario Dagenais, Dean's Representative  
Dr. Ian B. Spielman  
Professor Alicia J. Kollár

© Copyright by  
Ananya Sitaram  
2022

## Acknowledgments

I am extremely grateful to everyone who helped to make this thesis possible. Thank you to my advisor, Gretchen Campbell, for being such a great advisor over the past six years and also for being a part of the start of my AMO career, as my advisor for the SURF program back in 2014. Peter Elgee and I built the new strontium lab together and have been partners on the strontium experiment for all six years. It's been a long road, and I'm happy for both of us that we made it through. I'd also like to thank Daniel Barker for all of the support and knowledge he has passed down about strontium and many other topics over the past few years. Alessandro Restelli, the electronics expert of the JQI, has taught me everything I know about electronics. I would not have been able to accomplish all that I did without his help and I've learned so much from him. To the new strontium group members, Sara Ahanchi and Tim Li, thank you and also good luck – I know you both will do great things in grad school. I'd also like to thank previous strontium group members Benjamin Reschovsky, Neal Piseni, Hiro Miyake, and Alex Hesse, as well as ErNa group members Monica Gutierrez Galan, Swarnav Banik, Hector Sosa Martinez, Yanda Geng, and Shouvik Mukherjee, and all the CPRK group members over the years.

I am indebted to all of the great advisors and professors that I had during undergrad: Nick Bigelow, Chris Oates, Steve Eckel, Alex Iosevich, Steve Gonek, and many more. Thank you to the members of Professor Bigelow's CAT group for all of the support and

encouragement and for sparking my interest in atomic physics: Justin Schultz, Azure Hansen, Maitreyi Jayaseelan, Joe Murphree, Marek Haruza, and Steven Torrisi. Thank you also to the “Wolfs Pack”, my Rochester physics friends who got me through many nights of tough problem sets.

Finally, I want to thank my friends and family, who mean so much to me. My parents have been so incredibly supportive my whole life and have always both encouraged and facilitated my interest in science. Thank you to both of my lovely Ajjis. Thank you to my sister, Meghna, for being the best younger sister and also my best friend. Thank you to all of my friends, who I would not have gotten through the past six years without: Noor Shah, Jon Curtis, Swaksha Rachuri, Anant Dalela, Blake Sha, Grahya Guntur, Kristin Neil, Tori Delaney, Nathaniel Drake, Andrew Fuentes, Steven Torrisi, Laurel Brown, Christine Mooney, Charlotte Kwon, Tara Hanley, Meghan Fullman, and Nicole Grady. You’re all real ones. Last, but not least, thank you to my cat, Jane, for being the best emotional support animal a PhD student could ask for.

## Table of Contents

Acknowledgements	ii
Table of Contents	iv
List of Tables	vii
List of Figures	viii
Chapter 1: Introduction	1
1.1 Laser Cooling and Trapping	1
1.2 Properties of Strontium	3
1.3 Bosonic Blue MOT	6
1.4 Fermionic Blue MOT	8
1.5 Bosonic Red MOT	10
1.6 Fermionic Red MOT	12
1.7 Optical Dipole Trap	14
1.8 Box Trap Experiments	15
1.9 Grating Magneto-Optical Traps	18
1.10 Thesis Outline	21
Chapter 2: Experimental Apparatus	23
2.1 Vacuum System	23
2.1.1 AOSense Source	25
2.2 Blue Laser System	26
2.2.1 Blue Spectroscopy Laser	26
2.2.2 Blue Cooling Laser	28
2.3 Repump Lasers	29
2.3.1 679 nm Repump	29
2.3.2 707 nm Repump	31
2.4 Red Laser System	31
2.4.1 Red Cavity Laser	32
2.4.2 Red Cooling and Stirring Lasers	33
2.5 Dipole Trap Lasers	34
2.6 Clock Laser	36
2.7 Optical Setups	36
2.8 Magnetic Field Coils	40

2.9	Design of Fast Coil Current Control	41
2.9.1	Experimental Requirements	41
2.9.2	Typical Circuit	42
2.9.3	New Circuit Schematic	44
2.9.4	IGBT Driver Circuit	46
2.9.5	Testing 100 A Shutoff	46
2.9.6	Tuning of the PI Controller	47
2.9.7	Derivative Action	51
2.9.8	Voltage Limiter and Superdiode	53
2.9.9	Characterization of Magnetic Field	56
2.9.10	Optoisolation of MOSFETs	57
2.9.11	Conclusion	59
Chapter 3: JQI AutomatiON for Experiments (JANE)		60
3.1	Computer Control	60
3.2	Publication: Programmable System on Chip for controlling an atomic physics experiment	62
3.2.1	Abstract	62
3.2.2	Introduction	62
3.2.3	System Overview	65
3.2.4	Hardware Features	68
3.2.5	Firmware Development	72
3.2.6	Discussion	78
Chapter 4: Experimental Procedure		80
4.1	Blue MOT	80
4.1.1	Experimental Sequence	80
4.1.2	Absorption Imaging	81
4.2	Red MOT	84
4.2.1	Experimental Sequence	84
4.2.2	Electron Shelving Spectroscopy	86
4.2.3	Red MOT Search	87
4.3	Dipole Trap	89
4.3.1	Alignment	89
4.3.2	Cross Dipole Trap	91
Chapter 5: Strontium Grating Magneto-Optical Trap		92
5.1	Publication: Confinement of an alkaline-earth element in a grating magneto optical trap	93
5.1.1	Abstract	93
5.1.2	Introduction	93
5.1.3	Apparatus	95
5.1.4	Results	99
5.1.5	Discussion	106
5.2	Broad Line Grating MOT in $^{87}\text{Sr}$	108

Chapter 6: Narrow Line Sr Grating MOT	111
6.1 Sawtooth Wave Adiabatic Passage (SWAP) Cooling . . . . .	111
6.2 SWAP in a MOT . . . . .	113
6.3 Simulations of SWAP in a Grating MOT . . . . .	115
6.4 Changes to the Apparatus . . . . .	118
6.5 Results . . . . .	122
6.5.1 Experimental Procedure . . . . .	123
6.5.2 Demonstration of SWAP . . . . .	125
6.6 Future Work . . . . .	128
6.7 Conclusion and Outlook . . . . .	130
Bibliography	132

## List of Tables

1.1	Properties of Strontium Isotopes . . . . .	3
1.2	Zeeman shifts of hyperfine states of $^{87}\text{Sr}$ . . . . .	9
3.1	List of opcodes . . . . .	74

## List of Figures

1.1	Strontium Level Diagram . . . . .	5
1.2	Force and Potential Energy in Red MOT . . . . .	11
1.3	Zeeman shifts of Fermionic Red MOT Hyperfine States . . . . .	12
1.4	Schematic of Box Trap Experiment . . . . .	16
1.5	Grating MOT Tetrahedral Geometry . . . . .	18
1.6	Blue Grating MOT Force Profile . . . . .	19
1.7	Red Grating MOT Force Profile . . . . .	20
2.1	Model of Main Apparatus . . . . .	24
2.2	Optical setup for AOSense Source . . . . .	25
2.3	Optics Setup for Blue Spectroscopy Laser . . . . .	27
2.4	Optics Setup for Blue Cooling Laser . . . . .	28
2.5	Optics Setup Repump Lasers . . . . .	30
2.6	Optics Setup for Red Cavity Laser . . . . .	32
2.7	Horizontal View of Science Chamber Optics . . . . .	38
2.8	Vertical View of Science Chamber Optics . . . . .	39
2.9	Bitter Coils . . . . .	40
2.10	Typical Circuit for MOT Field Coils . . . . .	42
2.11	New Circuit Schematic for MOT Field Coils . . . . .	44
2.12	IGBT Driver Circuit Schematic . . . . .	45
2.13	Current Shutoff from 100A . . . . .	46
2.14	Block Diagram for Measurement of Open Loop Transfer Function . . . . .	49
2.15	Bode Plots of Open Loop Transfer Function . . . . .	50
2.16	Derivative Component of Current Control Circuit . . . . .	52
2.17	Varistor Derating Curve . . . . .	53
2.18	Superdiode Circuit Schematic . . . . .	54
2.19	Schematic of Combined Current and Voltage Control . . . . .	55
2.20	Measurement of Magnetic Field Gradient . . . . .	56
2.21	Test Setup for Bitter Coils . . . . .	57
2.22	Optoisolation of MOSFETs . . . . .	58
2.23	Circuit schematic of optoisolator. . . . .	59
3.1	Schematic of the Labscript Suite . . . . .	60
3.2	Overall schematic of PSoC-based pattern generator . . . . .	66
3.3	Termination networks on carrier board . . . . .	69
3.4	Breakout board layout and PCB design . . . . .	70

3.5	Time Domain Reflectometry measurement of breakout board . . . . .	71
3.6	Illustration of the memory in the FPGA . . . . .	73
3.7	Bank switching and compiler check algorithms . . . . .	76
4.1	Blue MOT Experiment Sequence . . . . .	81
4.2	Absorption Imaging Example . . . . .	83
4.3	Image Gaussian Fit Example . . . . .	84
4.4	Red MOT Experiment Sequence . . . . .	85
4.5	Resonance Rings . . . . .	87
4.6	Red MOT Absorption Images . . . . .	88
4.7	Dipole Trap Alignment Absorption Images . . . . .	90
4.8	Cross Dipole Trap Absorption Images . . . . .	90
5.1	Sr Grating MOT apparatus cutaway sketch . . . . .	96
5.2	Grating MOT Loading Sequences . . . . .	100
5.3	Grating MOT atom number vs. detuning . . . . .	101
5.4	MOT loading parameters as a function of $I/I_{\text{sat}}$ . . . . .	102
5.5	MOT loading parameters as a function of source current . . . . .	104
5.6	Temperature measurement of atomic cloud . . . . .	105
5.7	$^{88}\text{Sr}$ and $^{87}\text{Sr}$ position offsets and axial force profiles . . . . .	109
6.1	SWAP Cooling Mechanism . . . . .	112
6.2	SWAP in a MOT . . . . .	114
6.3	SWAP Simulations using PyLCP . . . . .	117
6.4	Grating MOT Optical Setup . . . . .	119
6.5	Updated Grating MOT Vacuum System . . . . .	121
6.6	Absorption images of Blue and Red grating MOTs . . . . .	123
6.7	Experimental Procedure for grating MOT . . . . .	124
6.8	SWAP MOT Data . . . . .	126
6.9	Temperature Measurement of red grating MOT . . . . .	127
6.10	Lifetime of the red grating MOT . . . . .	128
6.11	Force Profiles without Stirring Laser . . . . .	129
6.12	$^{87}\text{Sr}$ Stirring in a Grating MOT . . . . .	129

## Chapter 1: Introduction

### 1.1 Laser Cooling and Trapping

The study of atoms and their structure and properties has long been a topic of interest in the scientific community. Before the invention of the laser in 1960 [1], studying gases of atoms was difficult because their average speeds on the order of 300 m/s, the speed of sound, at room temperature [2]. The Doppler shift and relativistic time dilation cause broadening of the spectral lines in thermal atoms, making spectroscopy and precision applications like atomic clocks extremely difficult. The thermal velocity of atoms can be reduced as the square root of the temperature by refrigeration, but at the temperatures at which atoms would have velocities under 1 m/s, most species would have condensed, with vapor pressures too low to have many atoms still in the gas phase. The idea to use laser light to manipulate atoms [3] and to slow an atomic beam with laser light was first proposed in 1978 [4] and makes use of momentum transfer when an atom absorbs a photon. If an atom with velocity  $v$  is irradiated by a counter-propagating laser beam, it absorbs a photon with momentum  $p = \hbar k$  where  $\hbar = h/2\pi$ . Once the photon is absorbed, the atom can then re-emit the photon in a random direction. The absorption causes a decrease in velocity of  $v_{rec} = \hbar k/m$  in the direction the atom was propagating, while the contribution of the emitted photon to the atom's momentum averages to zero

since the direction of photon emission has a symmetric random distribution [2]. We also find that for the laser to be resonant with an atomic transition while propagating towards the atom, the frequency  $\omega$  of the laser light must be detuned from resonance by  $kv$  due to the Doppler shift. After receiving some amount of momentum kicks depending on the natural linewidth  $\Gamma/2\pi$  of the transition being addressed, the atom will be Doppler shifted out of resonance. This gave rise to the idea to use a magnetic field to shift the energy levels in an atom so as to keep them on resonance with a fixed-frequency laser, and the invention of the Zeeman slower [5]. The concepts described above will be the basis for many of the cooling and trapping methods that will be described in future sections.

If we are able to cool atoms to sufficiently low temperatures, when the de Broglie wavelength  $\lambda_{dB} = h/p$  is on the order of atom-atom interaction distance, where  $h$  is Planck's constant and  $p$  is the particle's momentum, the quantum nature of these atoms is revealed [2]. Thus, advancements in laser cooling and trapping of atoms have led to many discoveries and innovations, including, but not limited to, the production of Bose-Einstein condensates (BEC) [6, 7], degenerate Fermi gases (DFG) [8], advances in quantum information [9] and quantum simulation [10], as well as precision measurement and quantum metrological devices like atomic clocks [11, 12]. In this thesis, we will focus on laser cooling and trapping of strontium atoms, in particular. In the following sections, we will elaborate on the properties of strontium, the procedure for cooling and trapping strontium, and background information for experiments that will be discussed further in later chapters.

Isotope	Spin Statistics	Abundance	Nuclear Spin	Scattering Length
$^{88}\text{Sr}$	Boson	82.58%	0	$-2a_0$
$^{87}\text{Sr}$	Fermion	7.00%	9/2	$96a_0$
$^{86}\text{Sr}$	Boson	9.86%	0	$823a_0$
$^{84}\text{Sr}$	Boson	0.56%	0	$123a_0$

Table 1.1: Spin statistics, abundance, nuclear spin, and scattering length of the four stable isotopes of strontium. Abundances are from Ref. [13] and scattering lengths are from Refs. [14, 15]

## 1.2 Properties of Strontium

Strontium is an element with two valence electrons (an alkaline-earth element), and as a consequence, it has both singlet and triplet states, as shown in Fig. 1.1. Normally, transitions between singlet and triplet states are forbidden because of the  $\Delta S = 0$  selection rule, but mixing between the  $^1P_1$  and  $^3P_1$  wavefunctions makes it so that the  $^1S_0 \rightarrow ^3P_1$  (intercombination line) transition is weakly allowed with a narrow linewidth of around 7.5 kHz. In addition, the ground state of alkaline-earth and alkaline-earth-like atoms (such as Ytterbium) have zero electronic angular momentum, or  $J = 0$ . Thus, the  $^1S_0 \rightarrow ^3P_0$  transition is doubly forbidden by the  $J = 0 \rightarrow J = 0$  selection rule, as well as the  $S$  selection rule. This makes the  $^1S_0 \rightarrow ^3P_0$  transition extremely weakly allowed with an even narrower natural linewidth than the intercombination line, on the order of mHz for the fermionic isotope. Such a narrow linewidth makes this transition ideal for optical atomic clocks, which rely on the precision of its oscillator, in this case a sample of alkaline-earth atoms [11, 12], and thus, this transition is often referred to as the

“clock transition”.

Strontium has four stable isotopes, and their spin statistics, relative abundances, nuclear spins, and scattering lengths are summarized in Table 1.1. The spin statistics and scattering length of a species are crucial to understanding its potential to be cooled to degeneracy. A particle’s spin informs its scattering properties. As such, bosons can only scatter in the odd partial waves ( $s, d, g\dots$ ), and fermions can only scatter in the even partial waves ( $p, f, h\dots$ ). Since the higher partial waves get frozen out at low temperatures ( $T \sim 0$  K), this has implications for gases of identical fermions [16]. While  $^{84}\text{Sr}$  has such a low abundance, its scattering length is favorable for evaporative cooling [17], and it was the first isotope of strontium to be cooled to degeneracy [18, 19]. The most abundant isotope  $^{88}\text{Sr}$  has a very small scattering length, and while the scattering length of the spin-polarized fermion  $^{87}\text{Sr}$  is favorable, it barely collides at low temperatures. These two isotopes have been cooled to degeneracy using sympathetic cooling, or species mixtures [20–22]. Due to the very large scattering length of  $^{86}\text{Sr}$ , one runs into issues with three body loss collisions when trying to evaporatively cool in an optical dipole trap, but this was also eventually overcome [23]. Because of its high nuclear spin  $I = 9/2$ , in  $^{87}\text{Sr}$  the the electronic angular momentum and the nuclear spin are completely decoupled between the ground ( $^1\text{S}_0$ ) and clock ( $^3\text{P}_0$ ) states [24]. This gives this isotope  $SU(N)$  symmetry, where  $N$  can be as high as  $2I + 1$ , and there have been many theoretical proposals to study this highly symmetric system [25–28], as well as an experimental realization [29].

Strontium is a solid metal at room temperature and has a low vapor pressure, and thus must be heated to 400-500 °C to achieve sufficient atomic flux. We use a

Zeeman slower and a 2D MOT confining stage to bring the average velocity of the atoms in the beam down to a speed that can be trapped in a broad-line MOT on the  $^1S_0 \rightarrow ^1P_1$  transition. In the following sections, we will elaborate on the full cooling and trapping procedure for  $^{88}\text{Sr}$  and  $^{87}\text{Sr}$ . In the final two sections, we will discuss a proposed experiment with  $^{87}\text{Sr}$  that can hopefully be done in our group in the future, as well as the theory behind the grating magneto-optical trap experiments that will be discussed in Chapters 5 and 6 of this thesis.

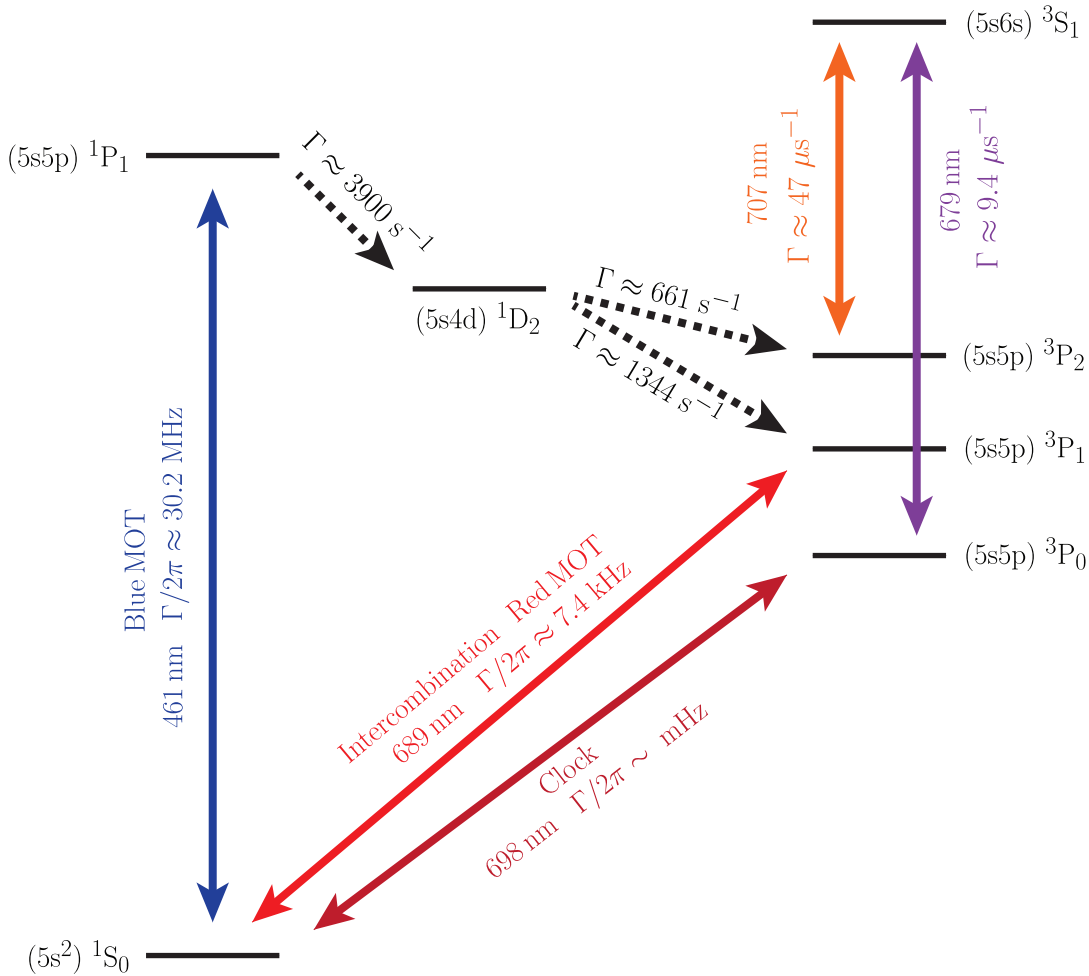


Figure 1.1: Strontium level diagram of all the relevant transitions addressed in our experiment. Transitions linewidths and decay rates are taken from Refs. [30–34].

### 1.3 Bosonic Blue MOT

A typical magneto-optical trap (MOT) consists of a quadrupole magnetic field and a six-beam optical molasses. The six laser beams are three pairs of counterpropagating circularly polarized beams. A MOT relies on the Zeeman effect and Doppler effect to cool and trap atoms. As mentioned earlier, the ground state ( $^1S_0$ ) of strontium has  $J = 0$ , and the excited state ( $^1P_1$ ) of the MOT transition has  $J = 1$ . We refer to this as the blue MOT, as the transition is at a wavelength of 461 nm. With the quadrupole magnetic field, we will get Zeeman splitting of the excited state into three different states,  $|-\rangle$ ,  $|e\rangle$ , and  $|+\rangle$ . The  $\sigma^+$  and  $\sigma^-$  polarized laser beams address the  $|+\rangle$  and  $|-\rangle$  states, respectively. If the frequency of the laser beam is red-detuned from the transition frequency such that  $\omega_L = \omega_0 - \delta$ , then the atoms will see the frequency as Zeeman shifted onto resonance if the light is propagating towards it. The atom absorbs a photon, and when it releases a photon due to spontaneous emission, the photon will scatter in any random direction. This causes a net momentum kick of  $\hbar k$  towards the center of the trap. On the other hand, a laser beam that is red-shifted and co-propagating with the atom will be seen as Zeeman shifted further away from resonance by the atom, and the excitation probability is even less, causing preferential momentum kicks towards the center of the trap.

The force from two counter-propagating laser beams along one axis is given by

$$\vec{F} = \hbar \vec{k} \Gamma_{sc}, \quad (1.1)$$

where  $\hbar$  is Planck's constant  $h/2\pi$  and  $\Gamma_{sc}$  is the scattering rate of the transition, given

by:

$$\Gamma_{sc} = \pm \frac{\gamma s/2}{1 + s + [2(\delta \mp \omega_D \mp \mu' B/\hbar)/\gamma]^2}. \quad (1.2)$$

In Eq. 1.2,  $\gamma$  is the decay rate of the transition,  $s = I/I_{sat}$  is the saturation parameter,  $I_{sat} = \pi \hbar c \gamma / 3 \lambda^3$  is the saturation intensity,  $\omega_D = -\vec{k} \cdot \vec{v}$  is the Doppler shift,  $\delta = \omega_0 - \omega_L$  is the detuning of the laser light with respect to the transition frequency  $\omega_0$ , and  $\mu' = (g_e m_e - g_g m_g) \mu_B$  is the effective magnetic moment. The Landé g-factors and magnetic quantum numbers for the ground and excited states are given by  $g_g, m_g$  and  $g_e, m_e$ , respectively. The Doppler-limited temperature of the MOT is expressed as

$$T_D = \frac{\hbar \Gamma}{2k_B}. \quad (1.3)$$

In Eq. 1.3,  $\Gamma$  is the natural linewidth of the transition. For the 461 nm transition on which we operate the blue MOT in strontium,  $T_D \approx 730 \mu\text{K}$ , which is still too hot to load into an optical dipole trap.

The  $^1S_0 \rightarrow ^1P_1$  transition is a quasi-closed transition, as there is a small branching ratio to the  $^1D_2$  state, as shown in Fig. 1.1. This allows atoms to decay to the  $^3P$  manifold, where they can get trapped in the long-lived  $^3P_0$  and  $^3P_2$  states, and they will no longer be capture by the MOT. To mitigate this issue, repump lasers on these states are often used. A common repumping scheme, and the one that we have used in this thesis, involves a 679 nm repump laser to address the  $^3P_0 \rightarrow ^3S_1$  transition, and a 707 nm laser to address the  $^3P_2 \rightarrow ^3S_1$ , so that atoms can then return to the ground state. Atoms that decay from  $^1D_2$  into  $^3P_1$  decay relatively quickly back to the ground state and so a repump laser

out of this state is not required, although this has been implemented previously in our research group [35]. Some research groups have also used different repumping schemes that address the  $^3D_2$  states [16, 36]. Although the ground state in strontium has angular momentum  $J = 0$ , the metastable state  $^3P_2$  does not, and the  $m_J = 1, 2$  sublevels are magnetically trapped by the MOT quadrupole field [37]. Thus, atoms can accumulate in this magnetic trap if the repump beams are initially left off and recaptured in the MOT once they are turned on. This technique has been utilized to sequentially load different isotopes of strontium [16], and enhanced loading into the metastable reservoir has been shown in Ref. [35].

## 1.4 Fermionic Blue MOT

For the fermionic isotope,  $^{87}\text{Sr}$ , we get hyperfine splittings because of its nuclear spin  $I = 9/2$ . For the ground state,  $^1S_0$ ,  $J = 0$  so  $F$  can only be  $9/2$ , but for the excited  $^1P_1$  state, we have  $F = 7/2, 9/2, 11/2$ . The splittings for the hyperfine states are on the order of the linewidth of the blue MOT transition, 30.2 MHz [33], shown in Table 1.2. Because we must have  $F' = F + 1$  for a stable MOT, we operate the fermionic blue MOT on the  $F = 9/2 \rightarrow F' = 11/2$  transition. Due to the fact that the hyperfine splittings are not resolved within the linewidth of the transition, there is unintended scattering on the  $F = 9/2 \rightarrow F' = 9/2$  transition, and this decreases the efficiency of the cooling of the blue MOT for  $^{87}\text{Sr}$ .

The hyperfine splittings for the states in  $^{87}\text{Sr}$  can be calculated using the following equation:

State	F	$g_F$	$\Delta E_{\text{HFS}}/h$ (MHz)
$^1S_0$	9/2	0	0
$^1P_1$	7/2	-2/9	36.8
	9/2	4/99	-23.5
	11/2	2/11	-4.9
$^3P_0$	9/2	0	0
$^3P_1$	7/2	-1/3	1414.12
	9/2	2/33	283.86
	11/2	3/11	-1179.29
$^3P_2$	5/2	-6/7	2371.22
	7/2	-1/7	1597.14
	9/2	2/11	618.69
	11/2	51/143	-551.52
	13/2	6/13	-1898.08
$^3S_1$	7/2	-4/9	2981
	9/2	8/99	542
	11/2	4/11	-2439

Table 1.2: Hyperfine splittings and g-factors of relevant states in the fermionic isotope,  $^{87}\text{Sr}$ . The hyperfine splittings are calculated relative to a theoretical isotope with  $I = 0$ , and the g-factors ignore the effect of the nuclear g-factor.

$$\Delta E_{HFS}/h = \frac{A}{2}K + \frac{Q}{2} \frac{\frac{3}{4}K(K+1) - I(I+1)J(J+1)}{I(2I-1)J(2J-1)} \quad (1.4)$$

In Eq. 1.4,  $A$  and  $Q$  are the magnetic and electric quadrupole constants, respectively,  $I = 9/2$  is the nuclear spin, and  $K = F(F+1) - I(I+1) - J(J+1)$  [24, 38]. The values for  $A$  and  $Q$  can be found in Refs [39–42]. The hyperfine splittings for the relevant states in  $^{87}\text{Sr}$  are summarized in Table 1.2.

The repumping for the fermionic isotope is complicated by the hyperfine structure. As we can see from Table 1.2, both the  $^3\text{P}_2$  and  $^3\text{S}_1$  states have hyperfine splittings. Thus, for the 707 nm repump laser, the frequency must be modulated to cover as many of the allowed hyperfine transitions as possible. In our experiment, we have generally followed the hyperfine repumping scheme discussed in Ref. [43].

## 1.5 Bosonic Red MOT

Because the blue MOT only cools the atoms down to the milli-Kelvin level, a second stage MOT is necessary on the intercombination line,  $^1\text{S}_0 \rightarrow ^3\text{P}_1$ . We refer to the second stage MOT as the red MOT since the transition corresponds to 689 nm. For this transition, the natural linewidth is much narrower, around 7.5 kHz, and thus the recoil frequency,  $\omega_R = \hbar k^2/2M$ , or  $\omega_R/2\pi = 4.5$  kHz, is of the same order [44]. In this case, the MOT does not operate according to the same dynamics as are explained by semiclassical Doppler theory, and the relevant quantities are the detuning, the recoil frequency, and the power-broadened linewidth,  $\Gamma' = \Gamma\sqrt{1+S}$  since the saturation intensity of the red MOT transition is only  $3 \mu\text{W}/\text{cm}^2$  [45, 46]. In the red MOT, gravity is also no longer negligible,

as the MOT cooling force is only around  $16\times$  the force from gravity. Since the maximum cooling force is  $F = \hbar k \Gamma / 2$ , with the linewidth in the kHz range, the capture velocity of the red MOT is much lower than the average velocity of an atom in the blue MOT. To capture more velocity classes of atoms from the blue MOT, the frequency of the red MOT laser beams is modulated over a span of 2-8 MHz. The force for several laser frequencies and the effect of gravity on the potential energy in the vertical direction are both shown in Fig. 1.2. Because of gravity, the MOT forms where the cooling force and force from gravity are balanced out, and this causes the MOT to sag in the center. This will be shown in Chapter 4.

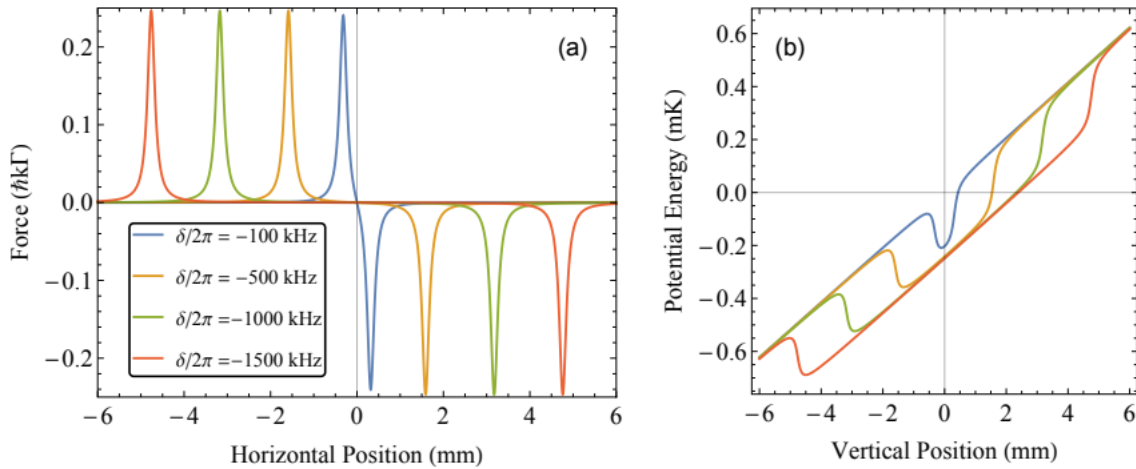


Figure 1.2: Figure taken from Ref. [38]. (a) Force vs. position in the red MOT with the red MOT laser at various detunings,  $\delta$ . (b) Potential energy from the MOT force and gravity in the vertical direction for the same detunings as in (a). Both graphs were made with the following parameters: saturation parameter  $s = 36$ , velocity  $v = 0$ , and a magnetic field gradient of 1.5 G/cm.

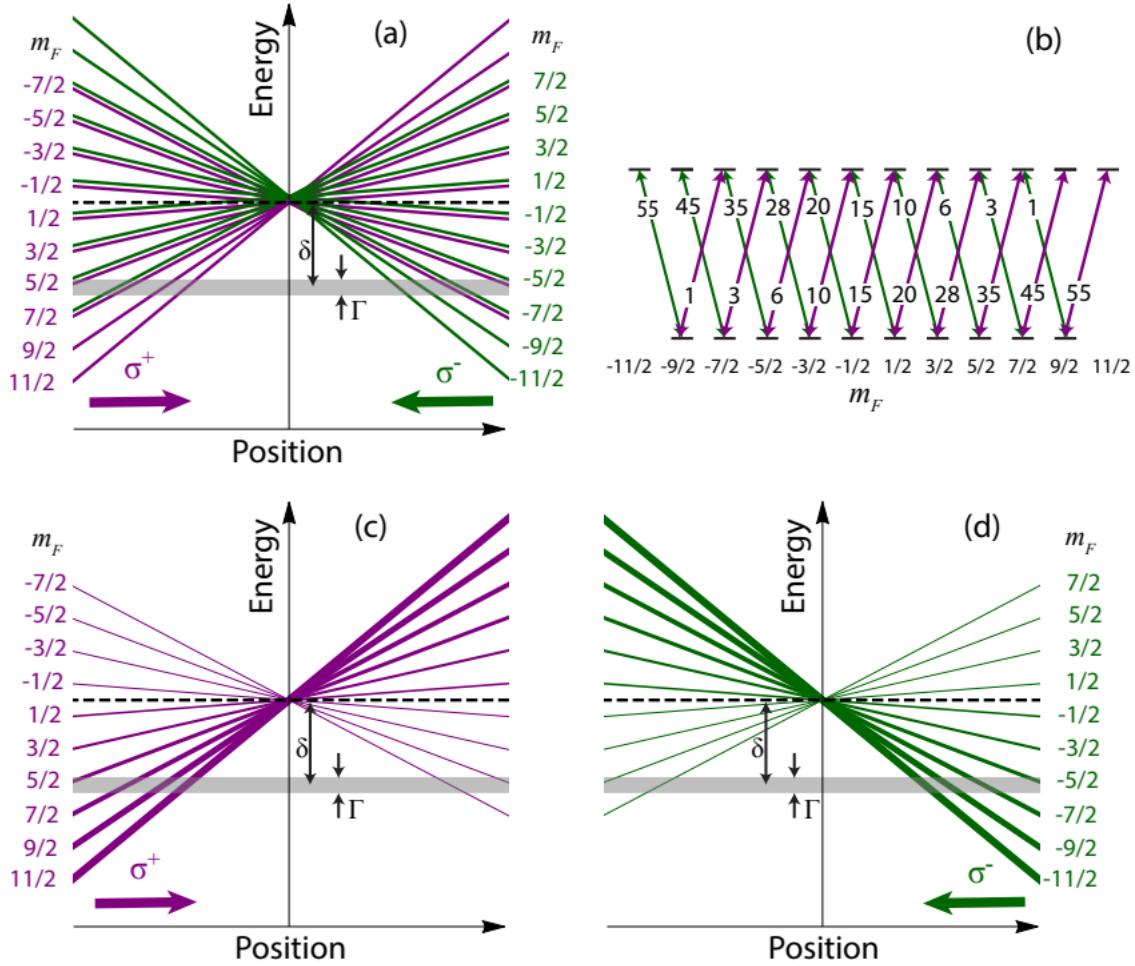


Figure 1.3: Figure taken from Ref. [38]. (a) All possible  $\sigma^+$  (purple) and  $\sigma^-$  (green) transitions are shown.  $\delta$  shows the detuning of the laser and  $\Gamma$  is the natural linewidth of the transition (translucent gray band). (b) All possible hyperfine transitions with associated squared Clebsch-Gordan coefficients, normalized so that the smallest coefficient is unity. (c) and (d) are the same as (a), except separated by  $\sigma^+$  and  $\sigma^-$  and with weighted lines based on the Clebsch-Gordan coefficient for that transition.

## 1.6 Fermionic Red MOT

For the fermionic isotope, the red MOT is more complicated because of the hyperfine structure. Since we are operating the red MOT on the  $^1S_0 \rightarrow ^3P_1$  ( $F = 9/2 \rightarrow F' = 11/2$ ) transition, the ground state  $^1S_0$  is split into 10 states with  $m_F = -9/2, -7/2, \dots, 7/2, 9/2$ , and the excited state  $^3P_1$  is split into 12 states with  $m_F = -11/2, -9/2, \dots, 9/2, 11/2$ . We

can have  $\sigma^{+(-)}$  transitions such that  $\Delta m_F = +(-)1$ . There is a large mismatch in Landé g-factor for the ground and excited states, creating a large difference in Zeeman shift sensitivity, causing unstable MOT operation. In Fig. 1.3(a), we can see the Zeeman shifts of all the possible final  $m_F$  states, with  $\sigma^+$  transitions shown in purple and  $\sigma^-$  transitions shown in green. The translucent gray bar represents the natural linewidth of the transition and indicates where an atom is resonant with the laser beams. If we have our  $\sigma^+$  MOT beam propagating from the left and the  $\sigma^-$  MOT beam propagating from the right, with a detuning  $\delta$  and natural linewidth of the transition  $\Gamma$ , the Zeeman shifting of the hyperfine states causes an atom to be resonant with light that will push it towards the center of the trap, as well as light that will kick it out of the trap. For example, if we have an atom in the  $m_F = 9/2$  ground state, the atom can absorb a  $\sigma^+$  photon to go to the  $m_F = 11/2$  excited state, or a  $\sigma^-$  photon to go to the  $m_F = 7/2$  excited state, shown in Fig. 1.3(b). If the atom is located at a position to the left of the trap center, it will be resonant with the  $\sigma^+$  beam that will excite it to  $m_F = 11/2$  and push it towards the trap center, but there is also a position where it will be resonant with the  $\sigma^-$  beam that will take it to  $m_F = 7/2$  and push it further to the left and away from the trap center. This will be the case for many of the hyperfine states and is shown more clearly in Fig. 1.3(c) and (d).

In order to get a stable restoring force in the fermionic red MOT, we employ a second “stirring” laser on the  $F = 9/2 \rightarrow F' = 9/2$  transition to re-randomize the populations of the ground state  $m_F$  levels. This was first demonstrated in Ref. [47]. The Landé g-factor of the  $F' = 9/2$  state is much smaller than that of the  $F = 11/2$  excited state, and thus the disparity in Zeeman shift sensitivity on this stirring transition is less than that of the cooling transition, making atoms in the trap resonant with this laser over a much

larger trapping volume. The g-factors and Zeeman shifts are summarized in Table 1.2.

## 1.7 Optical Dipole Trap

Because the ground state of strontium has  $J = 0$ , we are unable to use a magnetic trap, and the final stages of cooling are done using an optical dipole trap. Optical dipole traps typically use far-detuned light and make use of the optical dipole force. This is a much weaker interaction than in radiation pressure traps, allowing the trap not to be limited by light-induced mechanisms [48]. Considering the induced dipole moment of an atom with polarizability  $\alpha$  in an electric field  $\vec{E}$ , the dipole potential and scattering rate can be written as in Ref. [48]:

$$U_{dip} = \frac{3\pi c^2}{2\omega_0^3} \frac{\Gamma}{\Delta} I, \quad (1.5)$$

$$\Gamma_{sc} = \frac{3\pi c^2}{2\hbar\omega_0^3} \left( \frac{\Gamma}{\Delta} \right)^2 I. \quad (1.6)$$

In Eqn. 1.5 and Eqn. 1.6,  $c$  is the speed of light,  $\Gamma$  is the on-resonance damping rate,  $I$  is the intensity of the light, and the magnitude of the detuning,  $|\Delta|$  is much less than the transition frequency  $\omega_0$ . This gives the following relation between the dipole potential and the scattering rate:

$$\hbar\Gamma_{sc} = \frac{\Gamma}{\Delta} U_{dip}. \quad (1.7)$$

From Eqn. 1.5, we can see that if the light is red-detuned from the transition ( $\Delta < 0$ ),

then the dipole potential is negative, and the trap is attractive, whereas if the light is blue-detuned ( $\Delta > 0$ ), the potential is positive and the trap is repulsive. Our experiment and future proposed experiment would use both of these types of traps. From the above equations, we can also see that the dipole potential scales as  $I/\Delta$ , whereas the scattering rate scales as  $I/\Delta^2$ , hence why most dipole traps use a large detuning and high intensity to keep the scattering rate as low as possible for a given potential depth [48]. In our experiment we use both 1064 nm and 813 nm light for our dipole traps, which are both far red-detuned from the strong  $^1S_0 \rightarrow ^1P_1$  transition in strontium.

## 1.8 Box Trap Experiments

One exciting area of research with ultracold atoms involves quantum magnetism and spin models to gain insight into many-body phenomena [27, 49, 50]. The most common approach to these studies involves preparing a Mott insulator in an optical lattice and using the internal states of the atoms in each lattice sites to define the effective spin [49, 51]. However, the superexchange spin-spin interactions in such systems are relatively weak [49], and it is therefore very difficult to achieve the low temperatures (in the pK range [52]) and decoherence rates necessary to observe superexchange-based quantum magnetism.

Ultracold atoms can be prepared in specific internal spin states with very high precision, so it is easier to achieve much lower spin temperatures than it is to achieve motional temperatures. Thus, we can avoid the issue of high motional temperatures by creating a system in which the spin and motional degrees of freedom are decoupled. Such

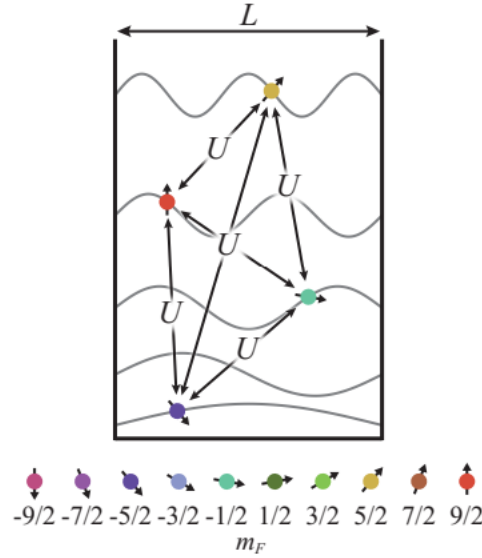


Figure 1.4: Figure taken from Ref. [52]. Illustration of the realization of an  $SU(N)$ -symmetric system in a 1D infinite square well box trap potential with width  $L$ . In the case of weak interaction energy  $U$  between atoms occupying different orbitals of the box trap, atoms cannot jump between the energy levels of the box trap, but the effective spin-spin interaction has infinite range.

a system requires a Hamiltonian  $\hat{H}$  that is independent of which orbitals are occupied, and has  $S_n$  permutation symmetry. There have been proposals to realize this type of system using an infinite square well anharmonic trap in one dimension, with tight confinement in the other directions using an optical dipole trap [27]. In addition to the  $S_n$  permutation symmetry, alkaline-earth atoms have  $SU(N)$  symmetry, and we can tune  $N$  between 2 and  $2I + 1$ , where for  $^{87}\text{Sr}$ ,  $I = 9/2$ . If we take  $\hat{z}$  as the axial coordinate and consider an infinite square well with width  $L$ , then the interaction energy for atoms in the box potential is given by:

$$U = 4\pi\hbar\omega_{\perp}a_{gg} \int_0^L \phi_j(z)\phi_k(z)\phi_{j'}(z)\phi_{k'}(z) dz \quad (1.8)$$

In Equation 1.8, a potential with frequency  $\omega_{\perp}$  freezes out motion in the transverse

direction,  $a_{gg}$  is the 3D scattering length, and  $(j, k)$  and  $(j', k')$  indicate the initial and final states of the interacting atoms, respectively. For the infinite square well with width  $L$ , we have the eigenstates  $\phi_j = \sqrt{2/L} \sin(j\pi z/L)$  and eigenenergies  $E_j = (\hbar\pi j/L)^2/2M$ . The interaction energy  $U$  reduces to the following expression when we consider that the integral goes to 0 unless  $j \pm k = \pm(j' \pm k')$  and conservation of energy requires that  $j^2 + k^2 = j'^2 + k'^2$  [27, 52]:

$$U = \frac{4\pi a_{gg} \hbar \omega_{\perp}}{L} \quad (1.9)$$

This interaction energy is independent of  $j$  and  $k$ . Now, we have the following Hamiltonian for the system:

$$\hat{H} = -U \sum_{j < k} \hat{s}_{jk} \quad (1.10)$$

Above,  $\hat{s}_{jk} \equiv \hat{c}_{jp}^{\dagger} \hat{c}_{jq} \hat{c}_{kp}^{\dagger} \hat{c}_{kq}$  and  $\hat{c}_{jp}^{\dagger}$  creates an atom in orbital state  $\phi_j(z)$  with nuclear spin  $p$ . The interactions described by the Hamiltonian in Equation 1.10 are spin exchange interactions of atoms in a lattice, but in this case the interactions are infinite range since the “lattice” sites are the energy levels of the infinite square well box trap [52]. This system can be realized experimentally with  $^{87}\text{Sr}$  using two magic-wavelength 813 nm dipole traps in the  $\hat{x}$  and  $\hat{y}$  directions to create the 1D system. The box trap can be created using a repulsive trap blue-detuned from the  $^1\text{S}_0 \rightarrow ^1\text{P}_1$  transition. The interaction energy in Eq. 1.9 must be smaller than the single-particle energy separations, which constrains the values of  $L$  and  $\omega_{\perp}$ . Ref. [27] proposes a blue-detuned Gaussian beam trap with a waist of 30  $\mu\text{m}$  projected onto a rectangular mask with width 10  $\mu\text{m}$ . Using this type of

spin interaction system, many experiments are possible, including spectrum estimation of density operators using Ramsey spectroscopy [28, 53] and production of Greenberger-Horne-Zeilinger (GHZ) states using the clock state, with applications to metrology and clock precision [27, 54, 55]. Certain design aspects of our experimental apparatus were informed by the intention to perform these types of experiments, and this will be discussed in Chapter 2.

## 1.9 Grating Magneto-Optical Traps

As there are more advancements with quantum devices, there is an interest in creating miniaturized versions of these devices that are portable and field-deployable.

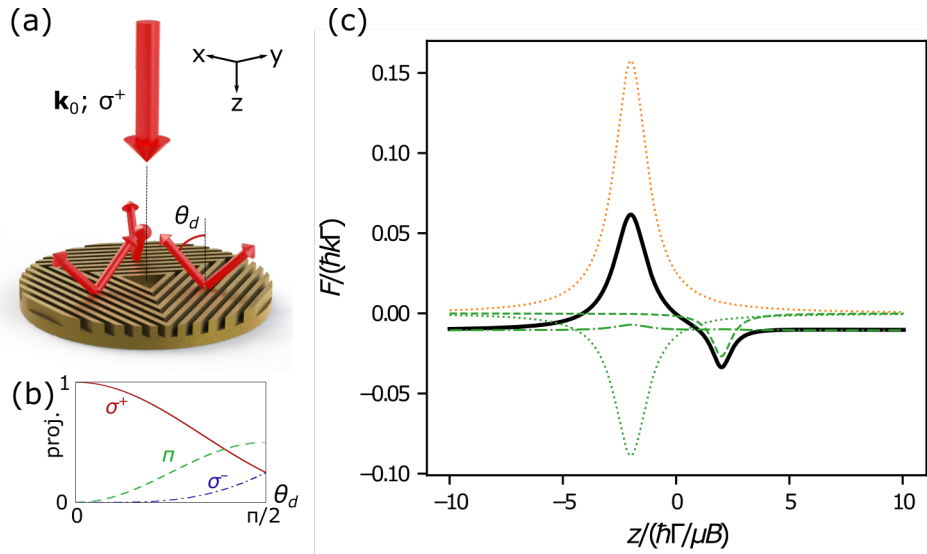


Figure 1.5: Illustration of the tetrahedral grating MOT. (a) Incident beam with  $\hat{k}$  vector  $k_0$  and  $\sigma^+$  polarization hits a grating with three sections, creating three diffracted beams with diffraction angle  $\theta_d$ . (b) Relative intensity of  $\sigma^+$ ,  $\sigma^-$ , and  $\pi$  polarized light after diffraction off the grating as a function of diffraction angle  $\theta_d$ . (c) Force as a function of axial position from each polarization component. Incoming  $\sigma^+$  polarized beam is shown in orange and the force from the  $\sigma^-$  (dashed),  $\sigma^+$  (dotted), and  $\pi$  (dashed-dot) polarized components of the diffracted beams is shown by the green dashed/dotted lines. The total force is shown with the black trace.

Creating compact atomic physics systems has gained interest, and one strategy of miniaturizing these systems is by cutting down on the conventional six laser beams used to form a MOT. A tetrahedral MOT has beams whose  $\hat{k}$  vectors intersect at approximately  $109.5^\circ$  instead of  $90^\circ$  like a conventional six-beam MOT [56,57]. One can create this geometry by using one input laser beam and a diffraction grating [58,59]. If a laser beam propagating in the  $\hat{z}$  direction is normally incident on a grating chip with three sections arranged in a triangle, shown in Fig. 1.5(a), we will get three diffracted first order beams at diffraction angle  $\theta_d$  creating a tetrahedral shaped trap.

There are a couple of important differences in the dynamics of a tetrahedral MOT as compared to a conventional MOT. A conventional MOT relies on the Zeeman shift of atomic sublevels and purely circularly polarized light to give atoms momentum kicks towards the center of the trap. In a tetrahedral MOT using a diffraction grating chip, the  $\hat{k}$  vectors of the diffracted beams are not along the quantization axis of the magnetic field, so

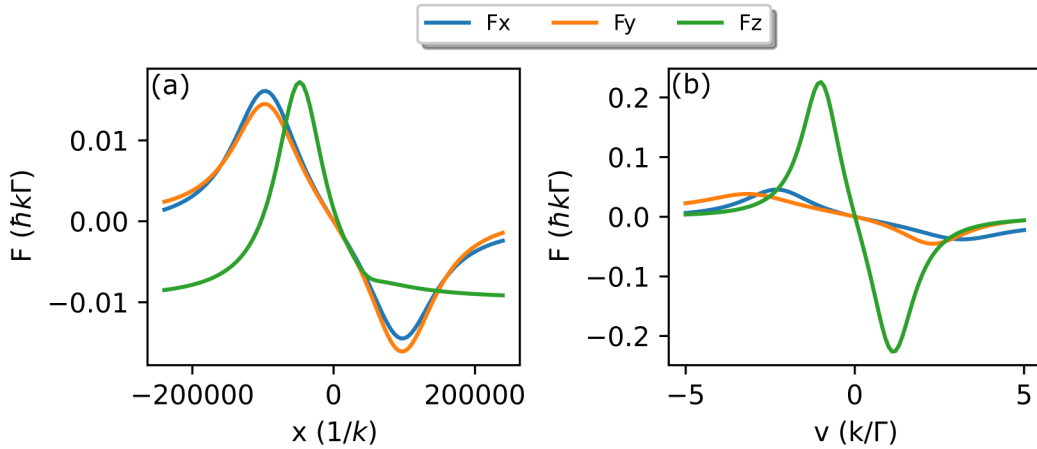


Figure 1.6: Force profiles for a blue grating MOT of  $^{88}\text{Sr}$  as a function of position (a) and velocity (b) along all three axes. Force is in units of  $\hbar k \Gamma$ , where  $\Gamma$  is the linewidth of the blue MOT transition. The label ‘x’ denotes the position in the  $\hat{x}$  (blue),  $\hat{y}$  (orange), and  $\hat{z}$  (green) directions. The transverse force resembles that of a typical MOT, while the  $\hat{z}$  force has a negative offset, causing the MOT to form above the magnetic field zero.

we must rely on the projection of the diffracted order onto the quantization axis, and the diffracted beams have a mixture of  $\sigma^+$ ,  $\sigma^-$ , and  $\pi$  polarization components instead of the purely reflected  $\sigma^-$  polarization. Fig. 1.5(b) shows how the scrambling of the polarization is dependent on  $\theta_d$ , and we can see that for much of the allowed values of  $\theta_d$ , the dominant polarization is the incorrect circular polarization  $\sigma^+$ . In Fig. 1.5(c), we see that this has the effect of weakening the spacial force from the incoming  $k_0$  laser beam. There is also a significant component of  $\pi$  polarized light, which produces an offset that makes the spatial force cross zero.

Because of its many applications to precision measurement and metrology [12, 60, 61], as well as quantum sensing and atom interferometry [62, 63], it is useful to make a compact cold atom system using strontium. In Fig. 1.6, we see a simulation using PyLCP [64] of the force created by a tetrahedral-like trap geometry for the blue MOT in

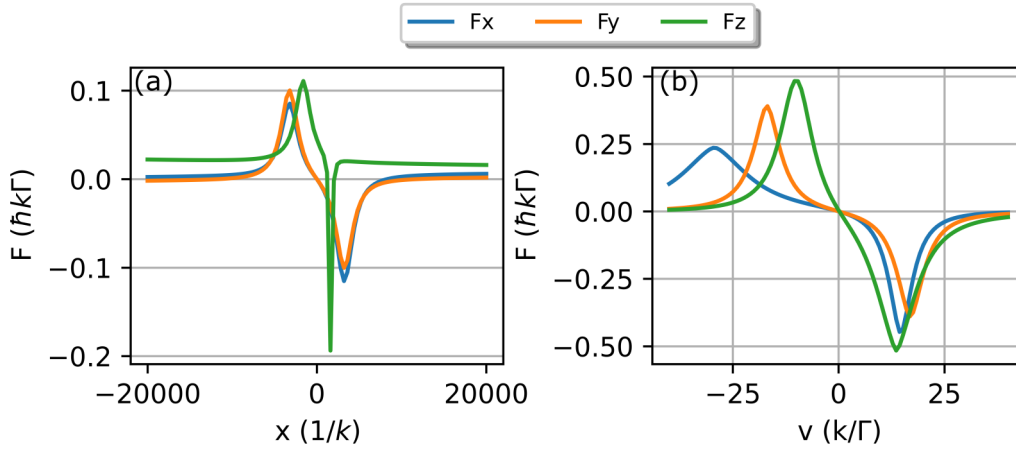


Figure 1.7: Force profiles for a red grating MOT of  $^{88}\text{Sr}$  as a function of position (a) and velocity (b) along all three axes. Force is in units of  $\hbar k \Gamma$ , where  $\Gamma$  is the linewidth of the blue MOT transition. The label ‘x’ denotes the position in the  $\hat{x}$  (blue),  $\hat{y}$  (orange), and  $\hat{z}$  (green) directions. In the force vs. position plot, the force from gravity has been incorporated. The transverse force resembles that of a typical MOT, while the  $\hat{z}$  force has an offset, causing the MOT to form above the magnetic field zero.

$^{88}\text{Sr}$ . While the force in the transverse directions resembles the force in a conventional six-beam MOT, the axial force has a negative offset, shifting the zero crossing of the force profile. This means that the MOT will form displaced slightly from the magnetic field zero. The displacement of from the field is different for the fermionic isotope than it is for  $^{88}\text{Sr}$ , and this will be discussed further in Chapter 5. We also see that in the force profile with respect to velocity, the transverse trapping force is relatively weak, and this causes grating MOTs to generally have an anisotropic temperature. We will also expand on this more in Ch. 5.

Again using PyLCP to simulate the forces present in the red MOT in  $^{88}\text{Sr}$ , we again see that the MOT will form above the field zero, based on the traces in Fig. 1.7. Another interesting feature of the axial force for the red grating MOT is the difference in width of the upward and downward peaks. This difference occurs because the incoming MOT beam has much more power than the diffracted beams, causing the upward peak to be power broadened, while the downward peak from the diffracted beams is not. The red grating MOT for both  $^{88}\text{Sr}$  and  $^{87}\text{Sr}$  will be discussed in more detail in Chapter 6.

## 1.10 Thesis Outline

In the remainder of this thesis, I will discuss various projects I have worked on throughout my PhD. In Chapter 2, I will give the details of the construction of our new apparatus for cooling and trapping strontium atoms, including the vacuum system, laser systems, magnetic field coils, and electronics. In Chapter 3, I will discuss the computer control of our experiment and the design of a programmable system on chip (PSoC)-based

pseudoclock device for controlling atomic physics experiments. Chapter 4 will include the progress made on the new strontium apparatus towards the box trap experiments mentioned in Section 1.8. In Chapter 5 and Chapter 6, I will present the realization of the first grating magneto-optical trap of an alkaline-earth atom and the demonstration of sawtooth wave adiabatic passage (SWAP) in a narrow-line grating MOT of strontium.

## Chapter 2: Experimental Apparatus

In this chapter, we will delve into the details of the main experimental apparatus that we built to do quantum simulation experiments with ultracold strontium, including the vacuum system, laser systems, magnetic field coils and the design of the coil current control electronics. The computer control and the design of a main pseudoclock device that is used to control the experiment will be discussed in Chapter 3.

### 2.1 Vacuum System

In Fig. 2.1, the vacuum system of the main apparatus is shown. The apparatus consists of the strontium source from AOSense, the pump body with NEG pump and ion pump attached, and the science chamber. The pump body is an 8 inch to 6 inch four way reducer cross that attaches to a 6 inch nipple connected to the science chamber, the integrated non-evaporable getter (NEG)/ion pump, and the ion pump attached at the bottom. The pump body also has a custom port for attaching an ion gauge. We use an ion pump with a pumping speed of 75 L/s and a NEG/ion pump with 1000 L/s pumping for  $N_2$  and 20 L/s pumping on non-reactive species, and both pumps are used to pump down the vacuum system. We achieve a final vacuum pressure of  $1 \times 10^{11}$  torr. We use a custom main science chamber, designed by previous graduate student Neal Pisenti, with three

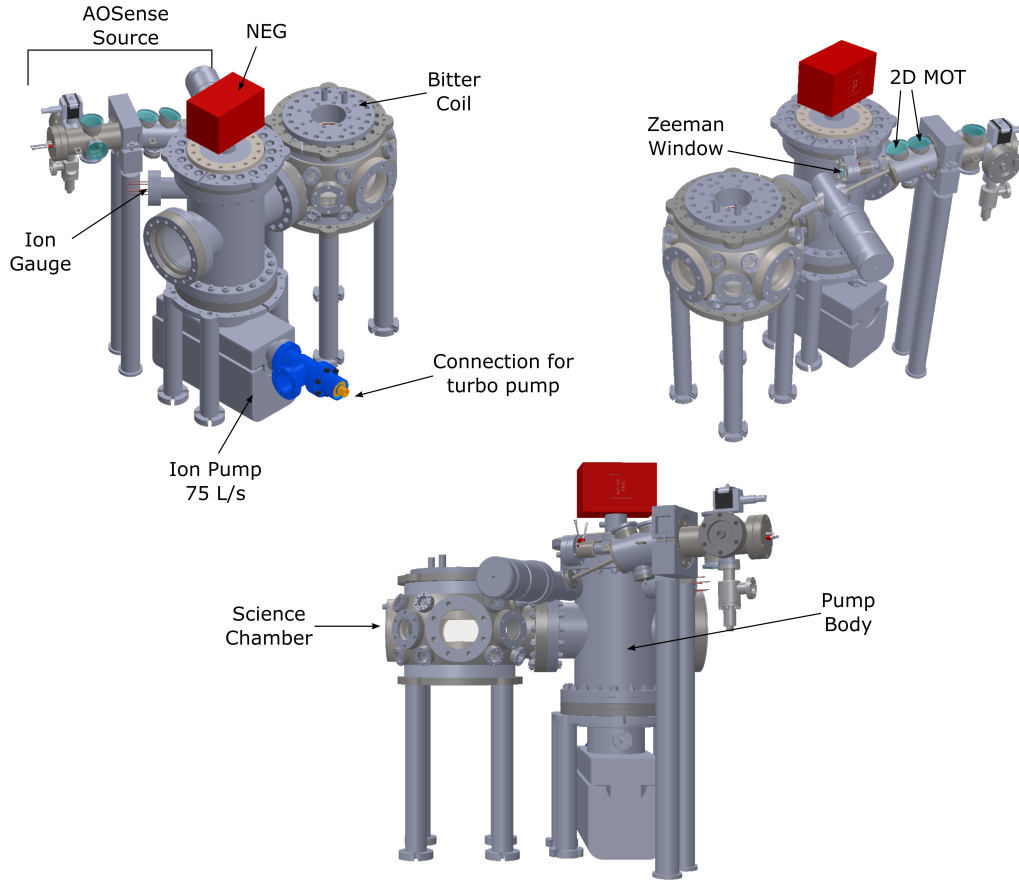


Figure 2.1: Model of vacuum apparatus from three different views. The AOSense source is pointed out specifically, as well as other key components.

4.5 inch viewports along the  $\hat{x}$  and  $\hat{y}$  directions. The fourth viewport (6 inch), on the  $\hat{y}$  axis, is located on the far side of the pump body. The science chamber also has a number of smaller viewports (2.75 and 1.33 inch) to optimize optical access. All viewports except for two have an anti-reflection (AR) coating for wavelengths of up to around  $1.2 \mu\text{m}$ . On the top and bottom of the science chamber, we have two 2.69 inch recessed bucket windows, which allow space for the Bitter coils that create our MOT field. The vacuum chamber is held up by lead-damped posts. We have custom breadboards with cutouts to fit around the vacuum system that hold all of the optics for the experiment. More details about the design of this system can be found in Ref. [46].

### 2.1.1 AOSense Source

We use the AOSense “Beam II” commercial atomic source. The AOSense source consists of a short permanent magnet Zeeman slower and a dual 2D MOT that provides transverse confinement. In Fig. 2.2, the atomic beam is shown with a green line. To release strontium atoms from the source, we heat the oven to around 430 °C. The Zeeman slower beam counterpropagates towards the atomic beam, through the Zeeman slower

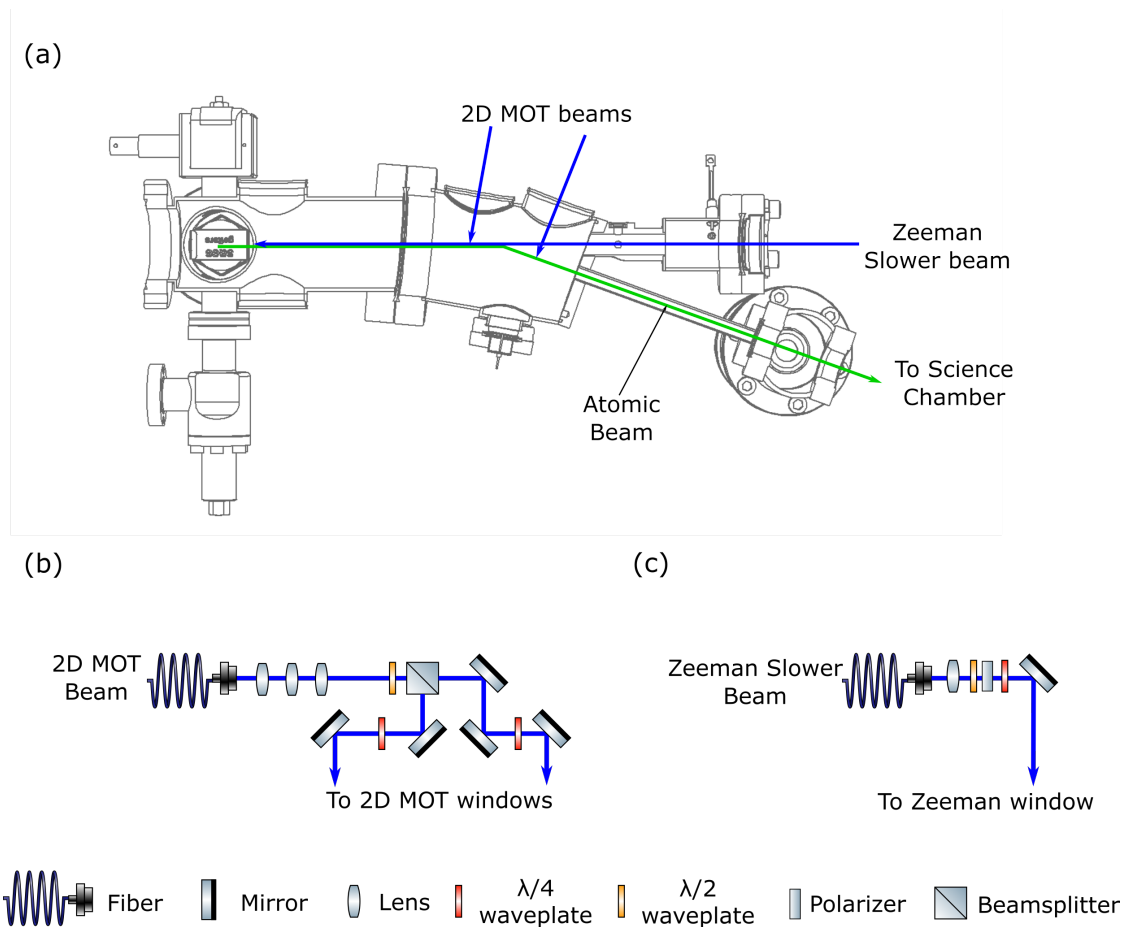


Figure 2.2: Optical setup for AOSense Source. (a) Cutaway sketch of the source showing atomic beam (green line) being slowed by the Zeeman slower beam (blue) and deflected down to the science chamber with the 2D MOT beams (blue) stage. Internal optics and permanent magnets are not shown. (b) Beam launch optics for the 2D MOT beams. Both beams are incident normal to the 2D MOT windows. (c) Beam launch optics for the Zeeman slower beam.

window, which is kept at a temperature of around 340 °C to prevent buildup of strontium. For the 2D MOT beams, the light is split between the two windows using a half waveplate and a polarizing beamsplitter (PBS) and circular polarization is ensured using quarter wave plates on both arms. The polarization purity of the Zeeman slower beam is also controlled using half and quarter waveplates, as well as a polarizer. The angling of the 2D MOT with respect to the science chamber allows the 2D MOT to act as an atomic beam shutter. The source contains in-vacuum permanent magnets, as well as internal optics to complete the 2D MOT, not pictured.

## 2.2 Blue Laser System

After the atoms are initially slowed/cooled with the Zeeman slower and 2D MOT stages, they enter the main science chamber, where we implement a first MOT stage on the broad  $^1S_0 \rightarrow ^1P_1$  transition at 461 nm. This transition has a linewidth of approximately 32 MHz. We use polarization rotation spectroscopy with a strontium hollow cathode lamp to lock our “blue spectroscopy laser” and beatnote lock the “blue cooling laser” to the blue spectroscopy laser.

### 2.2.1 Blue Spectroscopy Laser

The primary laser in our 461 nm laser system is a TOPTICA DL Pro laser. We lock this laser using Doppler-free polarization spectroscopy with a hollow-cathode lamp (Hamamatsu L2783- 38NE-SR) [65]. Light from the DL Pro is initially split with a PBS between the beatnote lock with the blue cooling laser and the rest of the optical setup.

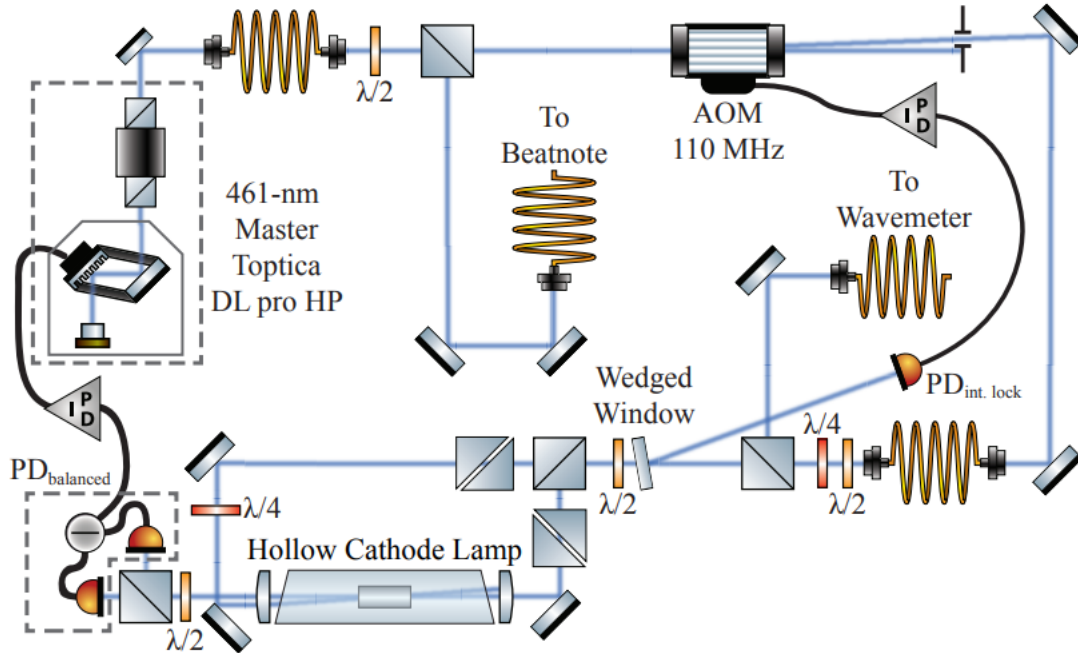


Figure 2.3: Spectroscopy setup for the primary 461 nm laser. Figure is taken from Ref. [52]. Light from the Toptica DL Pro HP is sent through a 110 MHz AOM and the shifted order is sent to a polarization spectroscopy setup. The light is split into a pump and probe beam and polarized with a PBS and Glan polarizer. The probe beam is split onto the two inputs of a balanced photodiode after passing through the hollow-cathode lamp, and the output is sent through a PID circuit that feeds back to the laser. Light is picked off along the way before the AOM to be sent to the wavemeter, and for intensity locking with feedback to the AOM. The hollow-cathode lamp is surrounded by a Mu-Metal box to prevent Zeeman shifts from stray magnetic fields.

From there, the light is shifted using a 110 MHz AOM and the 1st order diffraction is sent to the polarization rotation spectroscopy setup. A small amount of the light is picked off and used for an intensity lock. The light is polarized using a PBS and a Glan polarizer to ensure polarization purity and the strong pump beam is circularly polarized with a quarter waveplate before passing through the hollow-cathode lamp. A weak probe beam counterpropagates through the hollow-cathode lamp, and we get differential saturation of the  $\sigma^+$  and  $\sigma^-$  transitions of the 461 nm transition. This differential saturation is detected using a balanced photodetector, and the error signal is sent to a JQI PID box (designed by

J. Tiamsuphat), which feeds back to the laser.

### 2.2.2 Blue Cooling Laser

Our blue cooling laser is a frequency-doubled TOPTICA SHG Pro laser with first harmonic wavelength of 922 nm and output light at 461 nm. We use a series of half waveplates and PBS cubes to split the output of the laser into four arms that are sent to different parts of the experiment. On one arm, we shift the light with a 173 MHz AOM to create the light sent to the 2D MOT, and we use the 0th order beam from this AOM for

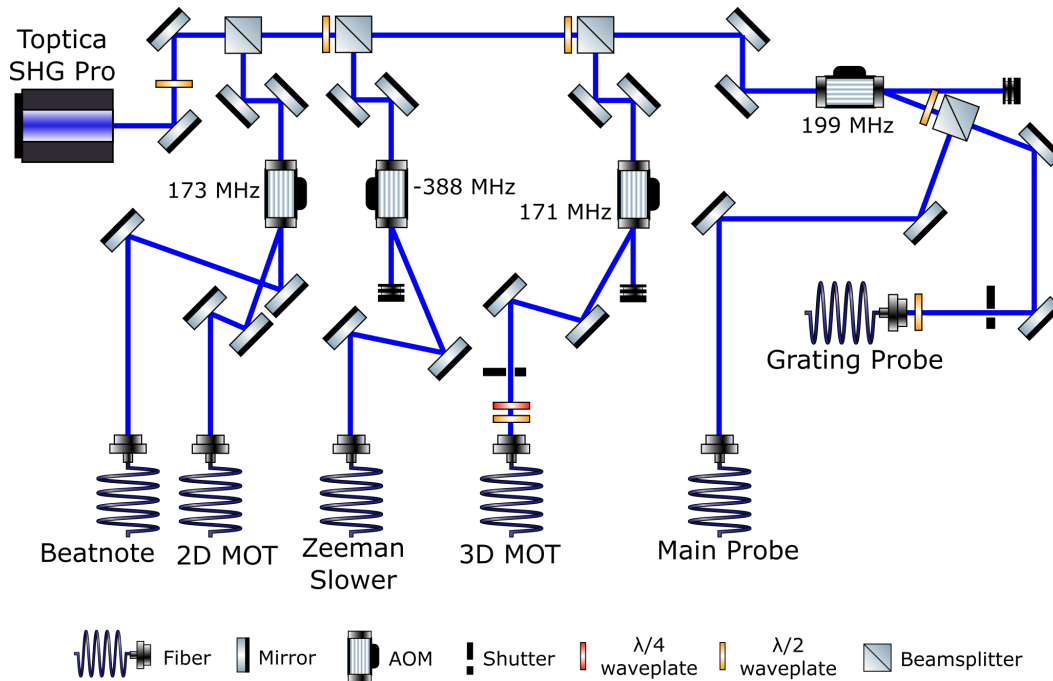


Figure 2.4: Optical setup for the blue cooling laser. Light is split off at multiple stages using a half waveplate and PBS. At each stage, the light is shifted using an AOM. We use a 173 MHz AOM and send the 0th order to a fiber splitter for the beatnote lock with the blue spectroscopy laser. The 1st order diffraction is sent to the 2D MOT. The original laser light from the Toptica SHG Pro is shifted 388 MHz down in frequency to be sent to the Zeeman slower. We shift the frequency up 171 MHz for the 3D MOT and we use an SRS shutter on this arm, along with a quarter and half waveplate to control coupling into the fiber. Finally, the laser is shifted 199 MHz up to generate light for the probe beams for both the main apparatus and the grating MOT apparatus.

the beatnote lock with the spectroscopy laser. The next arm of the laser output is shifted down by 388 MHz and is sent to the Zeeman slower. For the blue 3D MOT, we shift the laser output using a 171 MHz AOM and couple the light into a  $4 \times 4$  fiber splitter, giving around 9 mW of power per 3D MOT beam at the experiment table. We use an SRS shutter on this arm to allow for full extinguishing of the MOT beams. The final component of the Toptica SHG Pro output is shifted 199 MHz and is used for the probe beams for absorption imaging on our main apparatus and the grating MOT apparatus.

## 2.3 Repump Lasers

Atoms in the blue MOT can decay from the  $^1P_1$  state into the metastable states  $^3P_0$ ,  $^3P_1$ , and  $^3P_2$  through the  $^1D_2$  state. To prevent atoms from getting stuck in these metastable states, we use repump lasers to pump atoms out of the  $^3P_0$  and the  $^3P_2$  states. The atoms are excited to the  $^3S_1$  and are able to decay back down to the ground state  $^1S_0$  from there. In this section, an overview of both repumps is given, but more details about the design of these lasers can be found in Ref. [52].

### 2.3.1 679 nm Repump

The 679 nm repump laser addresses the  $^3P_0 \rightarrow ^3S_1$  transition. The laser is an external cavity diode laser (ECDL) using the Littman-Metcalf configuration. After sending the light through an optical isolator, we use a 207 MHz AOM to shift the frequency of the laser, and send the 0th order beam to a Toptica WS-7 wavemeter through a multimode fiber switch and the 1st order beam to the experiment. We lock the frequency of the laser

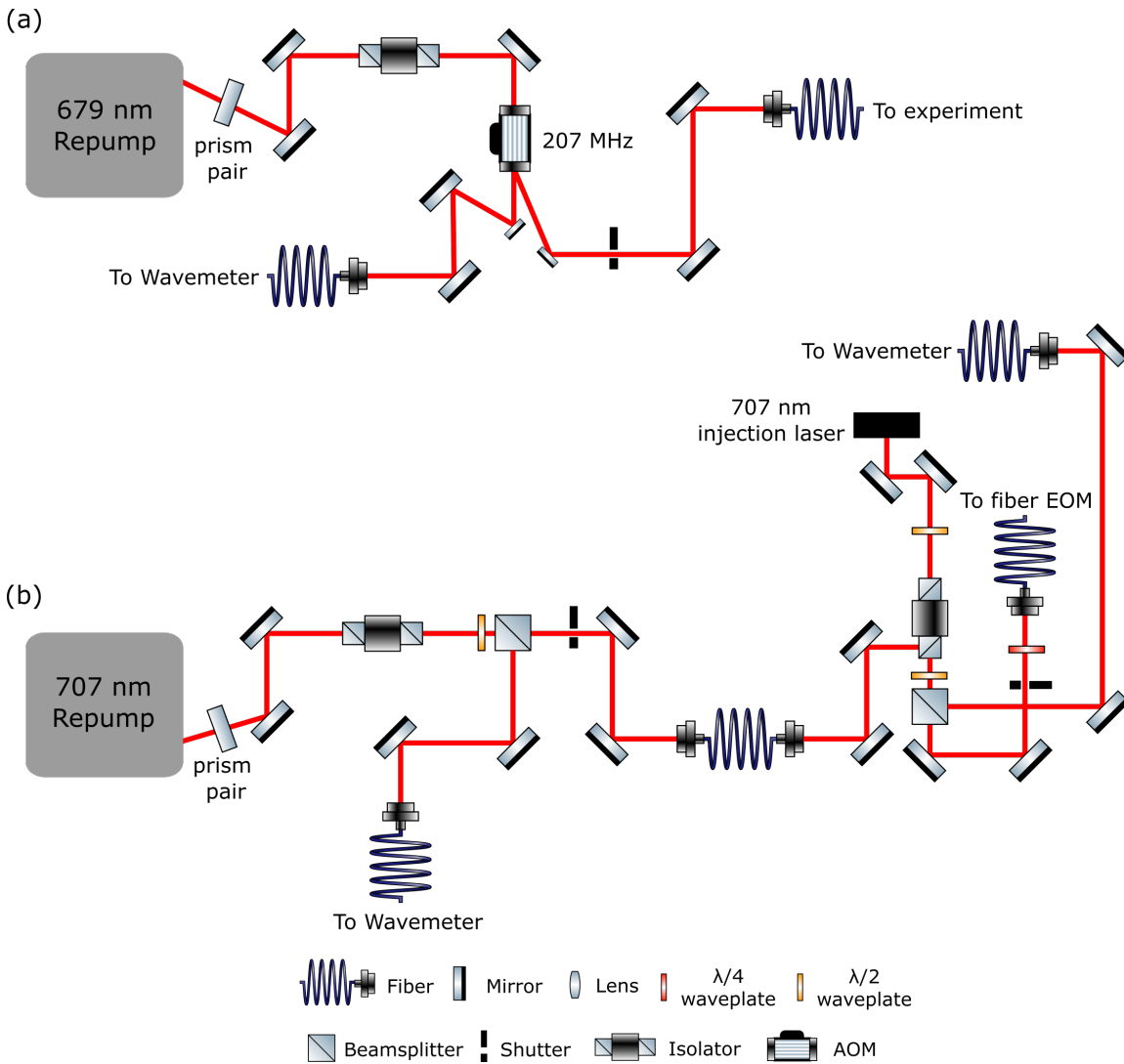


Figure 2.5: Optical setup for the repump lasers. (a) Optics for 679 nm repump. Light passes through a prism pair to modify the shape of the beam and then an optical isolator, before the frequency is shifted by a 207 MHz AOM and sent to the experiment. (b) Optics for 707 nm repump. Light passes through a prism pair and an optical isolator before it is split off to be sent to the wavemeter and sent to the 707 nm injection laser setup. Light from the 707 nm ECDL seeds the injection laser, which allows for more power to be sent to the fiber EOM, and then to the experiment.

using a Python program (written by new graduate student Yanda Geng) that reads from the wavemeter and feeds back to the voltage sent to the piezo-electric transducer (PZT) of the laser. We operate the laser at 441.33255 THz for  $^{88}\text{Sr}$  and at 441.33011 THz for  $^{87}\text{Sr}$ . After coupling the light into a fiber, we get around 2 mW of 679 nm light going into

the main chamber, through one of the mini-viewports. The power sent to the experiment can be extinguished using an SRS shutter. The optical setup for the 679 nm repump laser is shown in Fig. 2.5(a).

### 2.3.2 707 nm Repump

The 707 nm repump laser addresses the  $^3P_2 \rightarrow ^3S_1$  transition, and the optical setup is shown in Fig 2.5(b). Similar to the 679 nm repump, this laser is also an ECDL with the Littman-Metcalf configuration. The frequency of the 707 nm repump is also controlled by the same Python program that uses the frequency reading from the wavemeter and feeds back to the PZT voltage. The frequency of this laser is locked to 423.91366 THz for  $^{88}\text{Sr}$  and 423.91300 THz for  $^{87}\text{Sr}$ .

Because of the hyperfine structure of  $^{87}\text{Sr}$ , we must modulate the frequency of the 707 nm repump laser to address as many hyperfine transitions as possible. To do this, we use a fiber electro-optic modulator (EOM) that is controlled using an Arduino-based microcontroller that controls a high-frequency DDS from Analog Devices [46]. To increase the power sent to the experiment, we seed an injection-locked laser with light from the 707 nm ECDL before coupling the light into the EOM. Using the injection-locked system, we get around 4 mW of 707 nm light at the chamber.

## 2.4 Red Laser System

The red laser system is used to address the red MOT transition, or the  $^1P_0 \rightarrow ^3P_1$  transition. Because of the relatively narrow linewidth of this transition, around 7.5 kHz,



and FALC servo modules . The Toptica DL Pro laser has a measured linewidth of around 100 kHz and the ULE cavity has a finesse of 240,000, giving us a locking linewidth of around 6 kHz, which is sufficient for the intercombination transition. We keep the cavity under vacuum with a pressure of around  $5 \times 10^{-8}$  torr. Light from the DL Pro is doubled passed through a 1 GHz AOM before being split to be sent to the cavity and the beatnote lock with the red cooling laser. We split off a small amount of the light before the GHz AOM to send to the red injection (stirring) laser. The 1 GHz AOM allows us to access the intercombination line for all of the isotopes of strontium, as well as the  $F = 9/2 \rightarrow F' = 11/2$  hyperfine transition for  $^{87}\text{Sr}$ . The light sent to the beatnote lock with the red cooling laser is passed through a 99:1 fiber splitter, and the 1% arm is sent to be monitored by the wavemeter. To access the  $^{88}\text{Sr } ^1\text{P}_0 \rightarrow ^3\text{P}_1$  transition, we lock the cavity to a resonance at 434.82700 THz on the wavemeter.

## 2.4.2 Red Cooling and Stirring Lasers

The red cooling laser for the bosonic isotopes is a homemade ECDL using the design by Daniel Steck [67] with a long cavity (10 cm), and is thus referred to as the “Long Steck” laser in the lab, and throughout this thesis. The Long Steck laser is locked using a beatnote lock with the red cavity laser using a JQI PLL beatnote circuit. The frequency of the Long Steck is shifted using an 80 MHz AOM to bring it within 3 MHz of the intercombination transition. The detuning of the laser can be coarsely adjusted (10s of MHz) by changing the beatnote between the cavity laser and the cooling laser, and finely adjusted using the voltage controlled oscillator (VCO) in the AOM driver electronics. To

provide optimal transfer from the blue MOT to the red MOT, we broaden the frequency of the trapping laser by modulating the RF frequency supplied by the 80 MHz AOM. To control the detuning and broadening at the same time, the locking electronics of the AOMs are able to switch the RF control source rapidly between a voltage controlled oscillator (VCO) and a direct digital synthesizer (DDS). The light is coupled into a  $4\times 4$  fiber splitter to then be sent to the science chamber. We get approximately  $600\ \mu\text{W}$  of power in each of the red MOT cooling beams.

For  $^{87}\text{Sr}$ , we must use both a cooling laser and a stirring laser to re-randomize the populations of the hyperfine states, as described in Chapter 1. In this case, we use the Long Steck as the stirring laser and an injection-locked laser diode as the cooling laser. Schematics for the optical setups of the red cooling and stirring lasers and further details about the design and construction can be found in Refs. [38,46,52].

## 2.5 Dipole Trap Lasers

After the red MOT stage, we load our atoms into an optical dipole trap. For the dipole trap, we currently use a red-detuned trap generated by a 1064 nm 30W fiber laser (IPG YLR-30-1064-LPSF). Light from the fiber laser is split between the two different transverse arms of the dipole trap using polarizing beamsplitters. Each arm is passed through an AOM to allow for fast extinguishing of the beam, while we use homemade mechanical shutters to fully extinguish any residual light. Both arms of the dipole trap are coupled into large mode area (LMA) fibers to be sent to the experiment table. A schematic of this optical setup can be found in Refs. [38,46,52].

For each arm of the dipole trap (first and cross), we get around 3-4 W of power at the experiment table. We aim for a beam waist of around  $30 \mu\text{m}$  at the center of the science chamber, where the atoms are located, and therefore must choose the lenses before the chamber accordingly. Based on the distance to the center of the science chamber, the NA of the LMA fibers, and our desired beam waist, we calculate that we need a 400 mm lens before the chamber for our dipole trap in the  $\hat{x}$  direction and a 200 mm lens before the chamber for our cross dipole trap in the  $\hat{y}$  direction. We place both of these lenses on translation stages to allow for precise adjustment of the lens position, and thereby the focus of the dipole trap. A small amount of the light is picked off and sent to a photodiode for intensity locking using an FPGA-based servo [68]. We eventually intend on switching the dipole traps to the magic wavelength for strontium, 813 nm. To generate this wavelength, we plan to use an M2 SolsTiS laser system and 532 nm pump laser. The lens values were chosen with 813 nm in mind, but still work well enough for 1064 nm despite the chromatic aberrations.

To perform the box trap experiments discussed in Chapter 1, we must implement a repulsive dipole trap that is blue-detuned from the  $^1S_0 \rightarrow ^1P_1$  (461 nm) transition. In previous attempts of this kind of experiment, a 445 nm Nichia diode laser has been used, but there were issues with the mode of this laser. In the future, we will probably use the old Toptica SHG Pro laser inherited from the previous iteration of the Sr lab, if we are able to detune it from 461 nm enough. To create the desired box trap confinement in the  $\hat{z}$  direction, we plan to use a custom chrome mask from Front Range Photomask that will project a repulsive box trap with around  $30 \mu\text{m}$  of separation between sheets of blue light. For this experiment, we would have transverse confinement in just one direction using

one of the transverse dipole traps we have already set up for 813 nm light.

## 2.6 Clock Laser

The 698 nm clock laser addresses the  $^1S_0 \rightarrow ^3P_0$  transition, which has a very small linewidth, on the order of mHz. Thus, the laser that will probe this transition must be extremely precise. Similar to the red cooling laser, the clock laser is an ECDL and it is locked to a ULE cavity under a vacuum pressure of approximately  $5 \times 10^{-8}$  torr. The cavity's vacuum chamber is mounted on a Minus-K vibration stage and is also enclosed in a padded box to minimize mechanical and thermal variations. A Pound-Drever-Hall lock stabilizes the laser to the ULE Fabry-Perot cavity. The light is coupled to a broadband fiber EOM to span the difference between the transition frequency and the cavity resonances. Finally, we use an 80 MHz AOM to allow for fine adjustments of the detuning of the laser and for fast extinguishing of the beam. Further details of the design of the clock laser, including schematics of the optical setup, can be found in Ref. [46].

## 2.7 Optical Setups

Figure 2.7, shows a horizontal layout of the beam launch optics for the blue MOT, red MOT, dipole trap, and probe beams sent to the science chamber. Each blue MOT beam is collimated with a 75 mm focal length lens, and each red MOT beam is collimated with a 35 mm focal length lens. This gives an approximate beam waist of 9 mm for the blue MOT beams and around 4.2 mm for the red MOT beams. We do not include a telescope to resize our MOT beams. We combine the blue and red MOT beams on

dichroic mirrors that transmit blue light and reflect red light. The blue and red MOT beams are circularly polarized with a quarter waveplate before entering the chamber on both sides. We use a 400 mm (200 mm) focal length lens to give the dipole trap in the  $\hat{x}$  ( $\hat{y}$ ) direction a 30  $\mu\text{m}$  waist at the center of the science chamber. We use a pickoff mirror to split off a small amount of the power in the blue MOT and dipole trap beams for intensity locking. A flipper mirror is used to switch between using the horizontal probe beam and the retroreflection of the cross dipole trap beam. The horizontal imaging system uses a Grasshopper CCD camera. We do absorption imaging on the  $^1\text{S}_0 \rightarrow ^1\text{P}_1$  transition with  $2\times$  magnification.

In Figure 2.8, we can see the optical setup of the vertical beams sent to the science chamber. Similar to the horizontal blue (red) beam launch, we use a 75 mm (35 mm) collimating lens, and the MOT beams are combined on a dichroic mirror. The probe beam for the vertical high-resolution imaging system is sent along the same path as the MOT beams, and we use a PIXIS camera from Princeton Instruments. We use a high NA lens stack for the vertical imaging system. The high NA lens stack design is based on Ref. [69] and consists of four 2” lenses with precise spacing. The lens stack has an approximate overall focal length of 40 mm. More details about the design of the lens stack can be found in Peter Elgee’s thesis. A vertical 813 nm dipole trap beam can be added to this setup by swapping the steering mirror just above the chamber with a dichroic that reflects blue and red light and transmits infrared wavelengths. The pickoff mirror indicates where the future blue dipole box trap can be added.

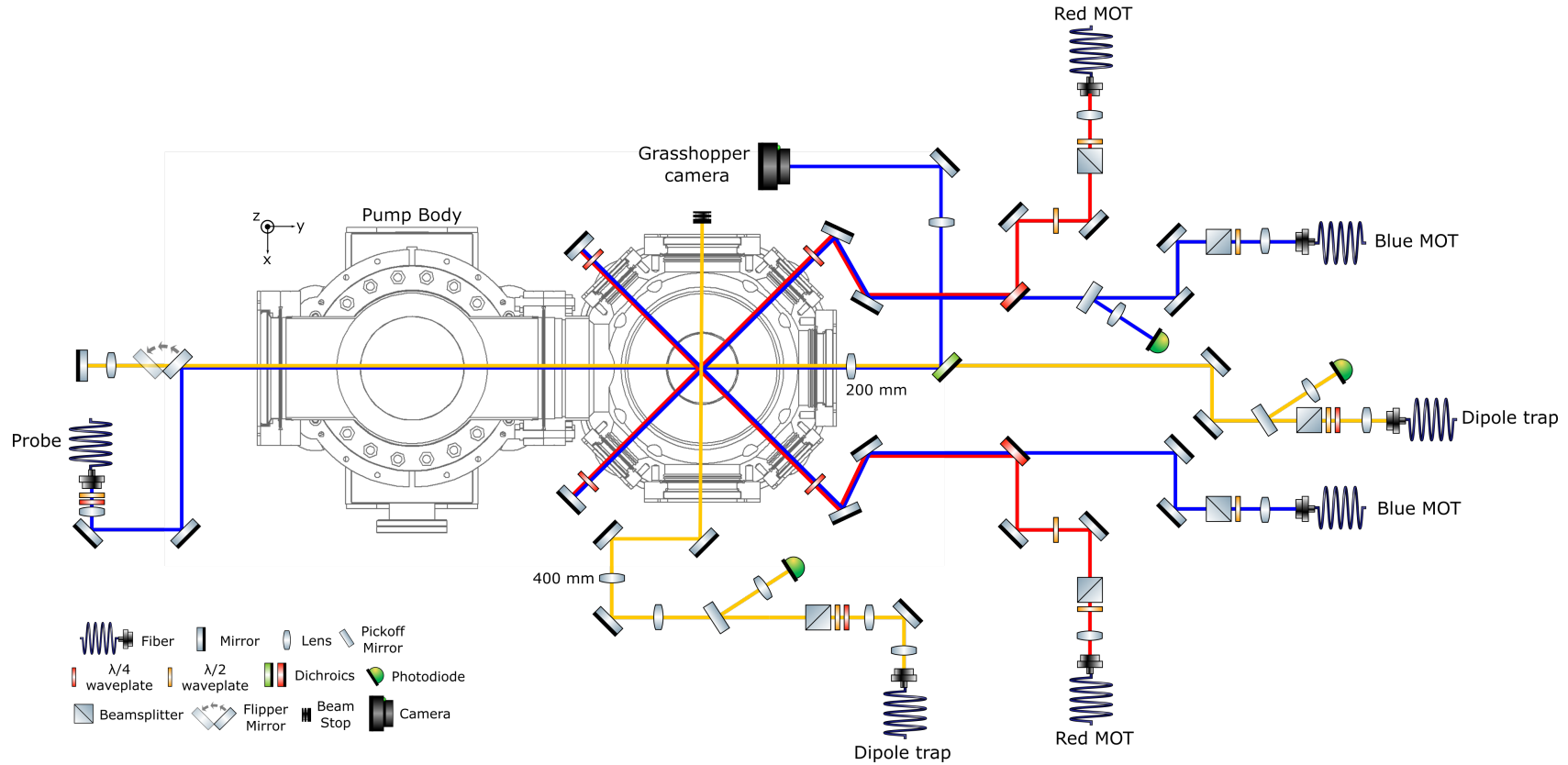


Figure 2.7: Horizontal schematic of the optics leading to the science chamber. Each blue MOT beam is collimated with a 75 mm focal length lens, and each red MOT beam is collimated with a 35 mm focal length lens. This gives an approximate beam waist of 9 mm for the blue MOT beams and around 4.2 mm for the red MOT beams. We do not include a telescope to resize our MOT beams. We combine the blue and red MOT beams on dichroic mirrors that transmit blue light and reflect red light. We use a 400 mm (200 mm) focal length lens to give the dipole trap in the  $\hat{x}$  ( $\hat{y}$ ) direction a  $30 \mu\text{m}$  waist at the center of the science chamber. We use a pickoff mirror to split off a small amount of the power in the blue MOT and dipole trap beams for intensity locking. A flipper mirror is used to switch between using the horizontal probe beam and the retroreflection of the cross dipole trap beam. The horizontal imaging system uses a Grasshopper CCD camera.

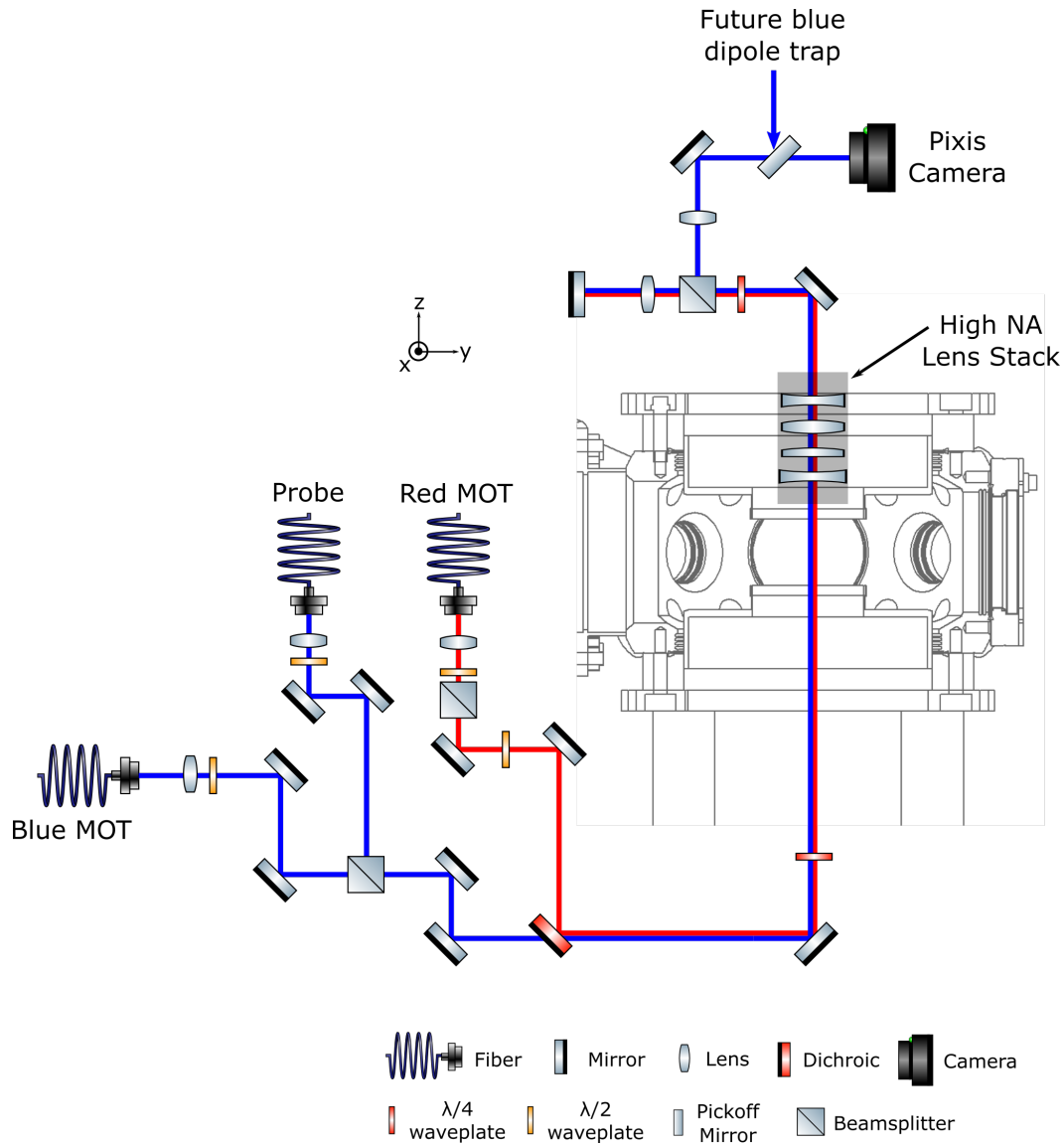


Figure 2.8: Vertical schematic of the optics leading to the science chamber. Similar to the horizontal blue (red) beam launch, we use a 75 mm (35 mm) collimating lens, and the MOT beams are combined on a dichroic mirror. The probe beam for the vertical high-resolution imaging system is sent along the same path as the MOT beams, and we use the PIXIS camera from Princeton Instruments. We use a high NA lens stack for the vertical imaging system. A vertical dipole trap beam can be added to this setup by swapping the steering mirror just above the chamber with a dichroic that reflects blue and red light and transmits infrared wavelengths. Pickoff mirror indicates where future blue dipole box trap will be added.

## 2.8 Magnetic Field Coils

When choosing a design for the coils that would create our MOT field, we wanted a system that would allow us to achieve high magnetic fields with efficient water cooling. Although the blue MOT for strontium only requires a magnetic field gradient of around 50 - 60 G/cm, orbital-induced Feshbach resonances in alkaline-earth and alkaline-earth-like elements have been of interest, and these experiments would require a moderately high magnetic field (greater than 100 G) [70–72]. For this reason, we went with a Bitter coil design. A Bitter electromagnet is constructed from interlocking copper disks with water cooling channels between each layer, allowing the water cooling to occur in parallel (rather than serially) and much more efficient dissipation of heat. Our coils were designed by visiting student Alex Hesse and are based on the designs in Refs. [73, 74]. A CAD rendering of the Bitter coil design is shown in Fig. 2.9. Our coils have two concentric stacks of copper disks with spacers between each layer for insulation. The cooling water

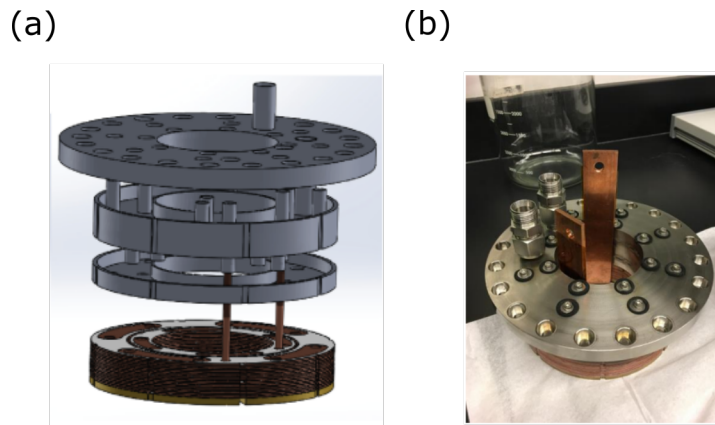


Figure 2.9: Pictures of the Bitter coil design for creating the MOT field. (a) Exploded view of a CAD rendering of the Bitter coil design. (b) Fully assembled bitter coil. We ended up using flat copper leads to deliver the current to the coils instead of the thin brass ones in the original design since the brass leads broke very easily.

passes through the vertical cutouts that are present in all the layers. We supply current to the coils via flat copper bars that are attached to the brass bottom layer of the coil. Initially, we used thin brass leads, but had to change the design since it was difficult to clamp the coil together tight enough without snapping the brass bars. Each coil was also coated in epoxy to prevent water leakage (not pictured). To cancel out stray fields in the red MOT, we have three sets of shim coils in a Helmholtz configuration along the  $\hat{x}$ ,  $\hat{y}$ , and  $\hat{z}$  axes. For the shim coils, we use thin rectangular wire with a  $2.1 \text{ mm} \times 0.7 \text{ mm}$  cross-section.

## 2.9 Design of Fast Coil Current Control

In this section, we will discuss the design of the current control electronics for our magnetic field coils. This is a design that I worked on during my earlier years in grad school, and much of this information is taken from my candidacy paper, with some slight modifications.

### 2.9.1 Experimental Requirements

As described in Chapter 1, strontium requires two different MOT cooling stages before loading into a dipole trap: the blue MOT and the red MOT. This means that the transfer efficiency of atoms from the blue MOT to the red MOT is very important. This is complicated by the fact that the blue MOT and the red MOT operate with very different magnetic field gradients. The blue MOT operates around  $55 \text{ G/cm}$ , whereas the red MOT operates around  $3 \text{ G/cm}$ . After the blue MOT has loaded completely, there is a Doppler

cooling phase, which involves ramping the power in the blue MOT beams down and the magnetic field gradient up to compress the atomic cloud before transitioning to the red MOT. In order to retain as many atoms as possible during the transfer from the blue MOT to the red MOT, we must switch the magnetic field very quickly between those two gradients. Typically, the field gradient must be switched in under 1 ms, so the electronics that control the current in our magnetic field coils must have the bandwidth and stability to facilitate this change in the gradient.

### 2.9.2 Typical Circuit

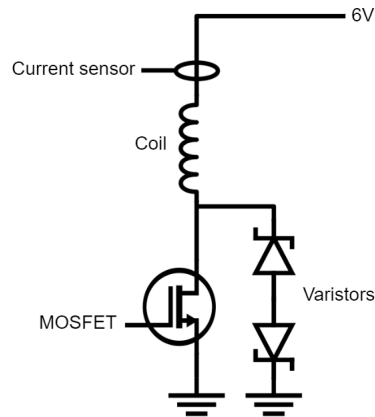


Figure 2.10: The typical setup for current control for MOT field coils. The coil is usually attached to a power supply on one end and a bank of MOSFETs on the other end. A current sensor detects the current flowing through the circuit just before the coil. A set of varistors protects the bank of MOSFETs from voltage spikes.

A typical setup for the current control of magnetic field coils for a MOT is shown in Fig. 2.10. The coil that creates the magnetic field is connected to a voltage power supply on one end and a bank of MOSFETs on the other end. Varistors protect the MOSFETs from voltage spikes. A proportional-integral (PI) circuit uses the signal from the current sensor to control the current running through the circuit. A coil of inductance  $L$  can be

described by the equation:

$$\frac{dI}{dt} = \frac{V}{L} \quad (2.1)$$

This means the rate of change for the current is limited by the voltage, given that the inductance of the coil is fixed. So, the time for the current to turn on, or reach a specified value, is limited by the voltage supply at 6V in Figure 2.10. Considering a coil with  $L = 200 \mu\text{H}$ , the rate of the current rising in this system is limited to:

$$\frac{dI}{dt} = \frac{6 \text{ V}}{200 \mu\text{H}} \approx 30 \text{ A/ms} \quad (2.2)$$

This somewhat slow rate of change for the current to turn on is adequate for our experiment. The ramp-up of the magnetic field is over a time period of 75 ms, giving plenty of time for the current in the coils to reach the desired value. The rate of the current turning off, however, must be much faster, as described in Section 2.9.1. For this circuit, we again use equation 2.1 to find the rate of change. This time, the voltage is limited by the clamping voltage of the varistors. In our experiment, we have chosen varistors with a voltage threshold of 30V. This gives:

$$\frac{dI}{dt} = \frac{6 \text{ V} - 30 \text{ V}}{200 \mu\text{H}} = -120 \text{ A/ms} \quad (2.3)$$

This is the rate at which we can shut down the current, and therefore the magnetic field, in a typical experiment, such as our previous experimental setup. In our previous setup, with this rate of current shutdown, we were able to achieve transfer efficiencies

of approximately 10% between the blue MOT and the red MOT. With this project, the objective is to increase the rate at which we can extinguish the current running through the coils in an effort improve this transfer efficiency.

### 2.9.3 New Circuit Schematic

To improve the turn-off time of the current, we propose the following alternative setup.

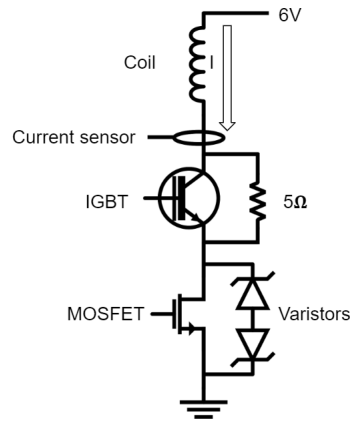


Figure 2.11: The new circuit schematic is similar to the previous one, but differs in that we include an IGBT protected by a 5 ohm resistor after the coil and before the bank of MOSFETs. The current sensor is placed between the coil and the IGBT.

We include an Insulated Gate Bipolar Transistor (IGBT) between the coils and the MOSFETs. An IGBT is a transistor that combines high input impedance and high switching speeds with low saturation voltage. These properties make it ideal as a semiconductor switching device. In this setup, we use the IGBT as a switch. The IGBT is closed (i.e. current is flowing through the circuit) when we are ramping the current up or the current is being held at a constant value. When the current is ramping down, the IGBT is opened, stopping current flow through the circuit. Since the IGBT is able to handle voltage spikes

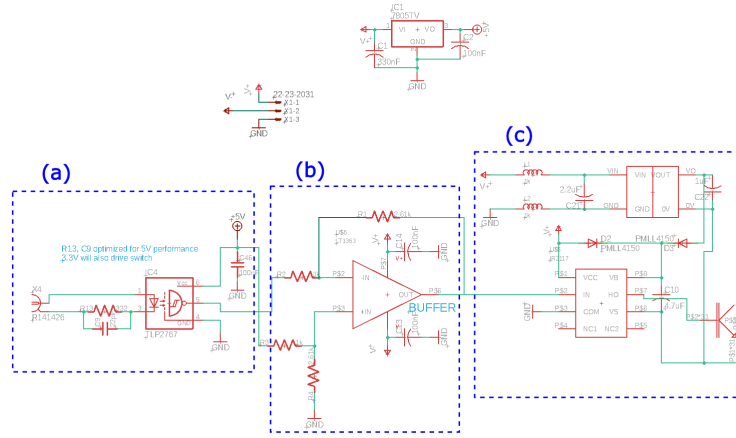


Figure 2.12: Schematic for IGBT driver circuit. (a) The optocoupler with passive components optimizing it for 5 V TTL input. (b) High-slew rate op-amp translates voltage from 5 V TTL logic to 0 to 10 V signal. (c) IR2117STRPBF [76] chip drives the gate of the IGBT.

of up to  $\sim 1.2$  kV the current turn-off time can be significantly reduced.

Returning to Eq. 2.1, we can calculate the turn-off slope for the current in this new configuration. In this case, we have a 5 ohm resistor across the IGBT. When the IGBT is opened, this limits the voltage to  $V = I_{max} \cdot 5\Omega$ . If we are turning off the current from 100 A, then  $I_{max} = 100$  A, and the voltage is limited to 750 V. Plugging this in Eq. 2.1, we get:

$$\frac{dI}{dt} = \frac{6 \text{ V} - 750 \text{ V}}{200 \mu\text{H}} = -3720 \text{ A/ms} \quad (2.4)$$

This turn-off rate for the current is  $\approx 31$  times higher than that from the previous circuit. In this setup, an IGBT driver circuit controls the IGBT like a switch and a PI board controls the current using the reading from the current sensor [75].

## 2.9.4 IGBT Driver Circuit

The IGBT driving circuit consists of three main sections, designated in Fig. 2.12 by (a), (b), and (c). The first section contains an optocoupler, which provides full isolation for the control electronics. The passive components around this element were chosen to optimize the circuit for a 5 V TTL input, but 3.3 V will also drive the circuit. Next in the circuit, we use a high-slew rate op-amp as a voltage translator to convert the optocoupler's 5 V TTL logic to a 0 to 10 V signal. This conversion is required by the IR2117STRPBF [76] that we chose to drive the gate of IGBTs and makes up the third section of this circuit.

## 2.9.5 Testing 100 A Shutoff

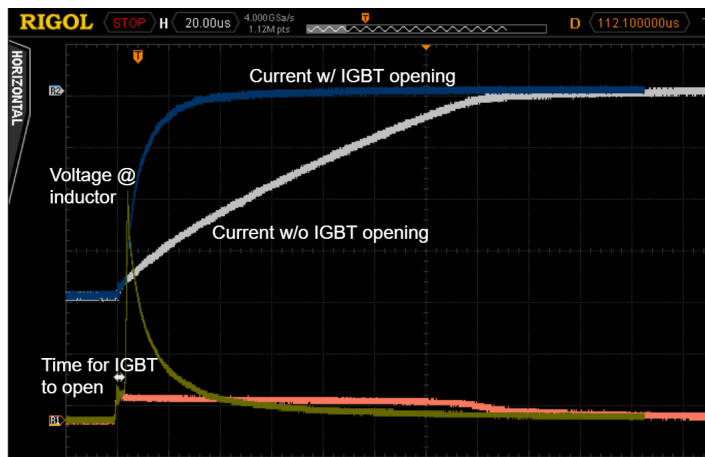


Figure 2.13: The traces depict the current and the voltage at the inductor for the two cases: IGBT opening and IGBT not opening. The current and voltage with the IGBT opening are depicted by the blue and the mustard lines, respectively. The current and voltage without the IGBT opening are depicted by the gray and the coral lines, respectively. The voltage scale is 100 V per division and the current scale is 25 A per division. The current scale is inverted. The time scale on the horizontal axis is 20  $\mu$ s per division. As expected, the rate of change of the current is significantly faster with the addition of the IGBT.

After constructing the IGBT driver circuit, we tested the effect of the addition of the IGBT to the current control system. We took measurements of the time it took for the current running through one coil to reach 0 A from 100 A with and without the switching of the IGBT. These tests were done with a test setup of one coil connected to a power supply via welding cables. The current running through the circuit was measured by a Danisense current sensor (model DS200ID [75]) placed around the welding cables. An additional high-voltage probe was placed on the setup to measure the voltage at the inductor (just before the IGBT) as well.

Figure 2.13 shows that when the IGBT is opened while the current is shutting off, the current reaches 0 A much faster than if the IGBT is kept closed. The blue trace (when the IGBT opens) reaches 0 A in approximately  $30 \mu\text{s}$ , whereas, without the IGBT opening, it would take this test setup almost  $140 \mu\text{s}$  to reach 0 A. We can also see that the spike in voltage at the inductor is much larger when the IGBT is opened, as expected. The voltage spike we measured was approximately 400 V, which is well within the tolerance of the IGBT.

### 2.9.6 Tuning of the PI Controller

The proportional-integral (PI) circuit that controls the current was designed by Dan Barker, a former student of the strontium experiment, who now works at NIST. The circuit was designed with Dan's experiment at NIST in mind, so there were some modifications to be made so that it was ideal for our experiment as well.

A PI circuit is a feedback loop circuit that uses proportional and integral elements

to control a system [77]. The control signal can be defined as follows:

$$u(t) = u_{bias}(t) + K_c e(t) + \frac{K_c}{\tau_I} \int_0^t e(t) dt \quad (2.5)$$

In Eq. 2.5,  $u(t)$  is the controller output,  $u_{bias}$  is the initial condition,  $K_c$  is the controller gain, and  $\tau_I$  is the integral time constant. The function  $e(t)$  is the error signal, defined as the difference between the setpoint and the actual value of the quantity that is controlled.

When expressed in the Laplace domain the system described in Eq. 2.5 can be written as:

$$G(s) = \frac{K_c (1 + s\tau_I)}{\tau_I s} \quad (2.6)$$

where  $s$  is the complex frequency.

Eq. 2.5 and Eq. 2.6 are a crude approximation of the behavior of a real PI controller because they assume that the proportional term operates up to infinite frequencies; a more accurate model of the controller would include additional poles at high frequencies to account for the unavoidable frequency gain roll-off. Those high frequency features are usually pushed by design well past the desired control bandwidth.

To assess the stability of the control system, and to find the optimal tuning parameters,  $\tau_I$  and  $K_C$ , we measure the open loop transfer function using a Bode-100 [78] network analyzer. Figure 2.14 shows how the PI controller with transfer function  $G(s)$  is wired to the MOSFET bank and the Danisense current sensor to control the current in the coils. The dynamic system resulting from the interaction of the coils, current sensor, IGBT, and

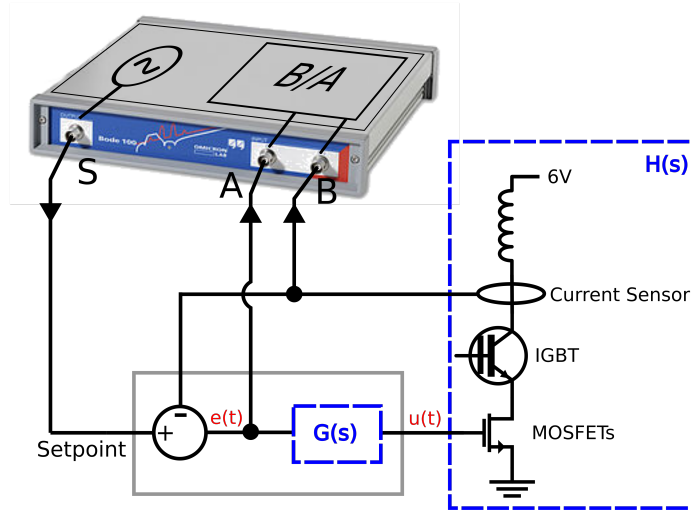


Figure 2.14: Block diagram the of system for the measurement of the open loop transfer function. The gray box represents the PI controller with transfer function  $G(s)$  while the controlled system  $H(s)$  is enclosed in the blue dashed box.

MOSFETs is represented by the transfer function  $H(s)$ . The negative feedback topology in Figure 2.14 produces the following transfer function,  $Y(s)$ , between the setpoint input to the current readout:

$$Y(s) = \frac{G(s)H(s)}{1 + G(s)H(s)} \quad (2.7)$$

The product  $G(s)H(s)$  is called the open loop transfer function, and by measuring it we can tune the parameters  $\tau_I$  and  $K_C$  to ensure asymptotic stability and optimal frequency response of the closed loop transfer function  $Y(s)$ . To assess the stability of our system, we use the Bode stability criterion. To use the criterion, we first make a Bode plot<sup>1</sup> of the amplitude and phase of the open loop transfer function and identify the gain and phase margins of the system. To obtain the Bode plot for the open loop transfer function, as shown in Fig. 2.14, we connect the signal source S of the network analyzer to the setpoint

<sup>1</sup>A Bode Plot is a bilogarithmic plot of the module of the transfer function and a plot of the phase with a logarithmic frequency axis

and we acquire the the error signal  $e(t)$  and the current sensor's output with channels A and B, respectively. Signals A and B correspond to the input and output of the block with transfer function  $G(s)H(s)$ . Therefore, the Bode plot of the open loop transfer function can be obtained by plotting  $|B/A|$  and  $\phi(B/A)$  as a function of frequency.

Figure 2.15 shows a series of Bode plots around a current set-point of 100 A during different phases of the PI tuning process. The Bode stability criterion can only be applied if the following two requirements are met: the open loop transfer function does not have any poles with a positive real part, and the gain crosses the 0 dB axis only once. The frequency at which the gain crosses the 0 dB axis corresponds to the control bandwidth of the closed loop system. Our system fulfills the two conditions. Next, we calculate the

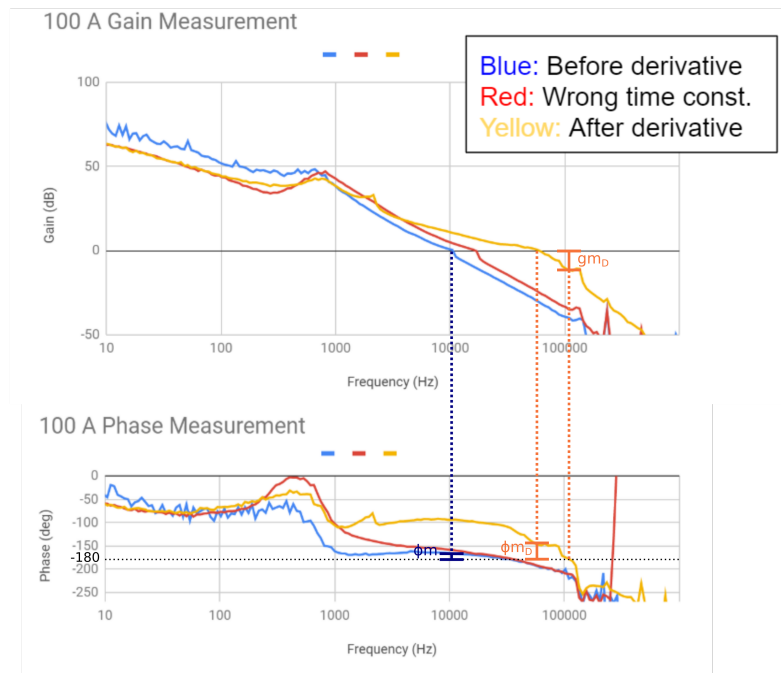


Figure 2.15: Bode Plots of the open loop transfer function  $G(s)H(s)$  at various points during tuning process. The phase margin for the blue and yellow traces is indicated as  $\phi_m$  and  $\phi_{m_D}$ , respectively, and the gain margin for yellow traces is indicated by  $gm_D$ .

phase margin and gain margin and verify that their values are within reasonable ranges.

The phase margin is calculated by determining the phase at the frequency at which the gain crosses 0 dB, and then adding 180 degrees to this number. Similarly, the gain margin is calculated by determining the gain at the frequency at which the phase reaches a 180 degree shift, and then subtracting that number from zero.

By looking at the open loop transfer function of the system after optimizing  $K_c$  and  $\tau_I$ , shown as a blue trace in Fig. 2.15, we can see that the bandwidth is around 10 kHz, as this is where the gain in dB drops below 0. The phase at the frequency at which the gain drops below 0 dB is almost -180 degrees, which means there is a phase margin of almost 0. This is not favorable according to the stability criteria and prevents us from improving the control bandwidth.

### 2.9.7 Derivative Action

To improve the stability of the system and increase the bandwidth, we notice that the open loop transfer function has a resonance peak close to 1 kHz on the gain plot. This resonance causes a phase flip of nearly 180 degrees, affecting the phase margin budget and limiting the maximum obtainable control bandwidth that can be obtained with just an integral and proportional term in  $G(s)$ . To try to fix this issue, we added a derivative component to the control circuit.

The derivative component adds a zero into the transfer function to introduce a 90 degree phase advance. The addition of the derivative action to the proportional part of the circuit is shown in Fig. 2.16. We chose values for the resistor (RG) and capacitor (CD)



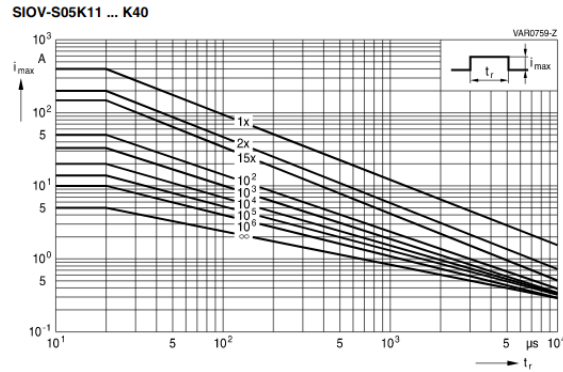


Figure 2.17: Varistor derating curve from EPCOS datasheet, page 28. The label on each curve represents the number of times the device can intervene clamping a voltage spike before being permanently damaged

created a stable closed loop system.

## 2.9.8 Voltage Limiter and Superdiode

The varistors shown in Fig. 2.11 have the essential role of protecting the MOSFET bank from overvoltage, and they were used in our lab’s previous current control system [52]. One of the issues we experienced with this solution is that the varistors tend to fail catastrophically after a certain number of interventions. A derating curve, such as the one in Fig. 2.17 is provided by the varistor manufacturers [79] to estimate the number of high current pulses that a varistor can endure before permanent damage. The number is a function of peak current and duration of the surge pulse and can vary from one to infinity. Varistors are mainly intended as a fault protection device that intervenes when an anomalous condition such as a power surge or static discharge happens on an electrical line, but in the circuit in Fig. 2.11, they would be constantly intervening to clamp the voltage across the MOSFETs. Therefore, a number of varistors (typically 8) are connected in parallel to share the current and guarantee protection for over 10,000 cycles.

Unfortunately, this approach is not foolproof and slight manufacturing differences between varistors can cause an uneven current distribution across them, causing premature failure of one device in the bank. Our lab and others following this approach typically have a failure of one varistor bank every 12-24 months and this is usually considered acceptable because the solution is simple and varistors are inexpensive.

A more robust solution would involve using the varistors as a backup, but actively controlling the MOSFET bank in a way that the voltage between the drain and source never exceeds a fixed maximum value, while the current is still independently regulated. This idea is best exemplified by a benchtop power supply. A benchtop power supply has current-limiting and voltage-limiting modes operating concurrently. If a load draws more current than the current limit you have set on the power supply, the supply will lower the voltage until the system draws the appropriate current. Similarly, the current is actively regulated to prevent the voltage from exceeding the voltage limit.

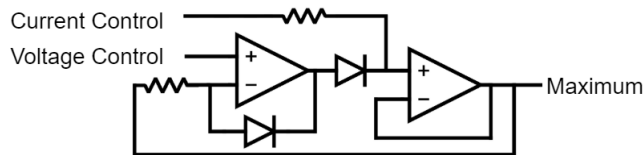


Figure 2.18: Superdiode circuit.

We took the same approach with the current control for our system: we added in a voltage control element and the capability to automatically switch between voltage and current control. To do this, we added two main components to the system: a voltage limiter circuit and a circuit called a “superdiode”. The voltage limiter detects the voltage at the node just before the MOSFETs and compares it to a setpoint voltage, producing

a voltage control signal. The superdiode is derived from a precision rectifier circuit and essentially chooses the maximum between two input signals. In this case, the two inputs to the superdiode are the current control and voltage control signals, as shown in Fig. 2.18.

Figure 2.19 shows the entire system with the double control. As an example, let us take the voltage setpoint of the voltage control as 50 V. The voltage control will take over if the voltage at the node across the MOSFETs rises above 50 V. This only happens when there is a high rate of change in the current flowing through the circuit, such as the circuit being shut off quickly when the IGBT is opened and the current setpoint is abruptly lowered; thus, the current control is dominant for most of the time.

During normal mode operation, the voltage,  $V_{bank}$ , across the MOSFET bank is low, and the voltage PID is unsuccessfully trying to regulate  $V_{bank}$  to the target voltage of 50 V by lowering the gate control voltage until it rails down to -15 V. Since this value is low, the superdiode will always choose the current control, since it looks for the maximum signal. When the voltage across the MOSFETs spikes, the PID now holds the voltage to the setpoint value and the superdiode will allow the voltage control to take over. In addition, we still have the varistors mentioned in Sections 2.9.2 and 2.9.3. The turn-on voltage of the varistors is higher than the setpoint of the active limiter so the MOSFETs

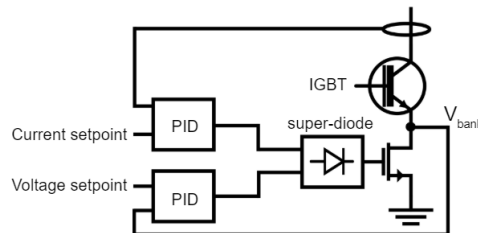


Figure 2.19: Combined current and voltage control. The wire extending upwards above the IGBT and current sensor would connect to the coils.

are doubly protected, and the varistors are used just as a backup fault protection.

### 2.9.9 Characterization of Magnetic Field

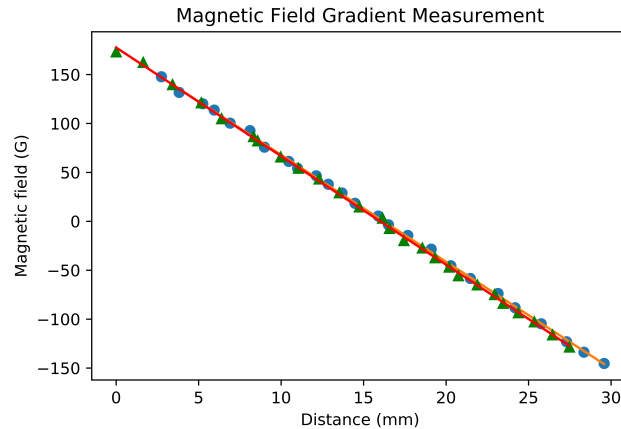


Figure 2.20: Measurement of the magnetic field gradient using the coils in a test setup with a current of 100 A. Two data sets are shown above, one in blue dots and one in green triangles. The fit line for the blue dots is shown in orange and the fit line for the green triangles is shown in red. The average gradient from these two data sets is 110.09 G/cm.

Once the current control was finalized, it was necessary to verify that the coils were producing the expected magnetic field and that the magnetic field gradient would be suitable to trap atoms. The coils were put into a test setup to mimic the approximate separation of the coils when placed on the vacuum chamber and therefore create approximately the same magnetic field the atoms would experience in the experiment. The water cooling of the coils was also tested in this configuration to be sure the coils would not leak before installing them on the vacuum chamber.

The coils were placed approximately 46 mm apart. The magnetic field in the z direction was measured using a gaussmeter. The probe was incrementally moved down the z-axis of the setup, 1-2 mm at a time and the magnetic field was measured at each of these positions. Measurements were taken with 100 A flowing through the coils. The

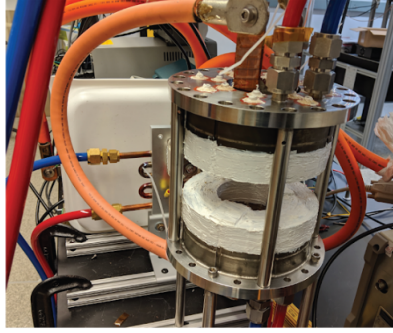


Figure 2.21: Test setup for the Bitter coils. The white coating on the coils is a potting resin to ensure that the coils would not leak.

magnetic field at the center of the quadrupole trap was verified to be 0 G. The data from two data sets were both fitted to a linear fit to determine the magnetic field gradient,  $\frac{dB}{dz}$ . The magnetic field gradient calculated from the two data sets were 109.2(5) and 111.0(5), giving an average value of 110.1(5) G/cm.

### 2.9.10 Optoisolation of MOSFETs

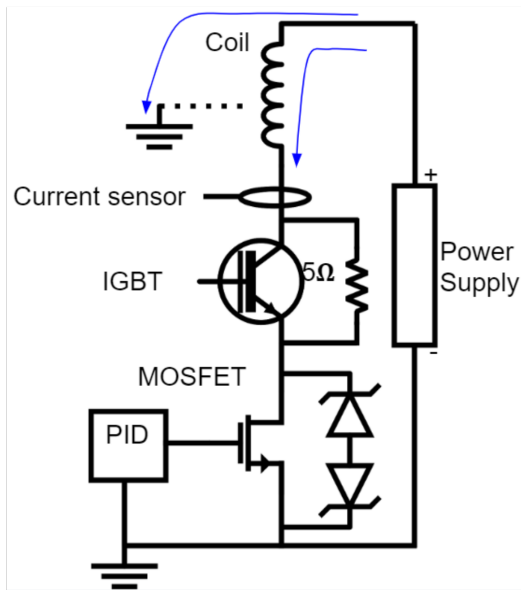
Once the Bitter coils were installed onto the vacuum chamber for the experiment and the control electronics were set up, it was time to test the entire system. One problem that we ran into immediately was that there was current running through the system (about 3 A) even when the current control was set to 0 A. After looking into this issue, we discovered that the reason extra current was flowing through the system was due to an extra connection from the Bitter coils to GND, shown in Figure 2.9.10(a) with the dotted trace.

The connection to GND from the coils occurs because the water flowing through the coils is in contact with the steel pieces that form the top and bottom of each coil, which are connected to GND. The water in the coils contains ions and also Optishield,

which was put in to prevent growth of algae in the coils and the rest of the water cooling system. The conductance from the water and Optishield combined is enough to form a significant enough GND connection in the system. To mitigate this issue, we switched to Optishield II, which is a low conductance version of the same product.

In addition to reducing the conductance of the liquid flowing through the system, we isolated the electronics that control the MOSFETs to eliminate the second route of current flow in the system. For the opto-isolation circuit, we use an optocoupler, two fast op-amps, and two buffers. To ensure linearity and flat amplitude and phase response up to 1 MHz we use an optocoupler with a matched pair of photodiodes [80], using one of them to provide feedback to the LED driving side, as shown in Ref. [81]. The op-amps (AD825ARZ) [82], denoted by IC2 and IC3 used in this circuit have a 41 Mhz and -3 dB

(a)



(b)

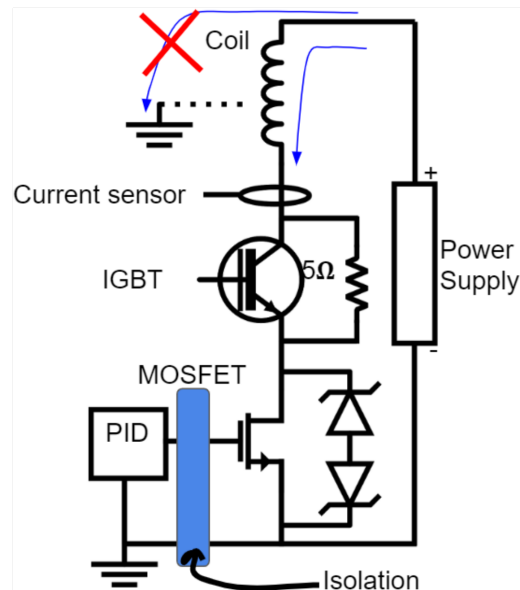


Figure 2.22: Schematic of system before and after optoisolation. (a) Circuit diagram of entire system showing two ways that current can flow. (b) Here, we see the same circuit diagram, except we have added an optoisolation circuit that isolates the electronics controlling the MOSFETs. This cuts the connection between the GND the coils are connected to and the GND that the PID circuit is connected to.



## Chapter 3: JQI Automation for Experiments (JANE)

### 3.1 Computer Control

While setting up our new experimental apparatus, we decided to move away from using LabView and SetList [85] and switch to using Labscript [84], which uses Python as a scripting language. The Labscript suite uses a hybrid text and GUI approach for experimental control. Labscript consists of three main components, shown in Fig. 3.1. First, an experiment script is written in Python. Runmanager allows you to define “global” parameters that can be applied any time they are called in the experiment script. When you

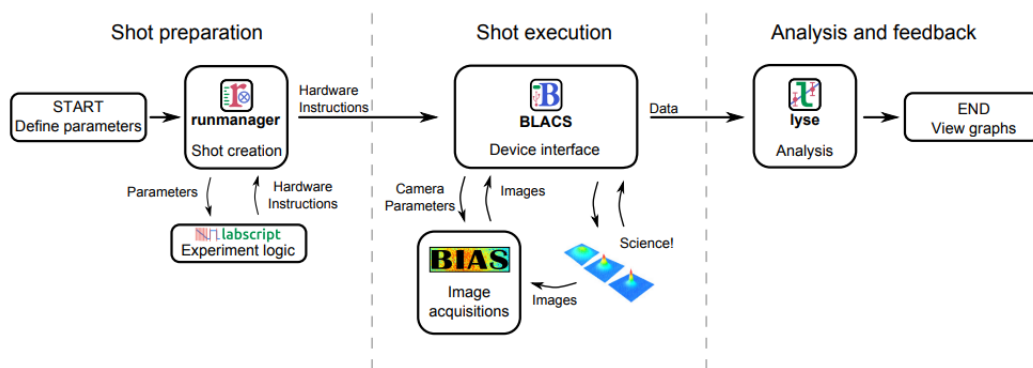


Figure 3.1: Figure taken from Ref. [84]. Schematic of all the components of the Labscript software suite. Experiment scripts are written in Python and using labscript-specific language. After global parameters have been defined, runmanager uses those parameters along with the experiment script to create the hardware instructions for the experimental shot. Blacs interfaces with hardware devices and delivers the instructions as dictated by the shot prepared by runmanager. Once the shot is over, Lyse is used for quick data analysis. Bias, the image acquisition module is no longer supported.

run an experimental shot on Runmanager, it then compiles a list of hardware instructions and timings based on the experiment logic and global parameters. These instructions are then sent to the experiment hardware via Blacs. Blacs also allows you to control hardware devices manually outside an experimental shot. Once the shot is run and the relevant data is collected, Lyse allows you to do quick, on the fly data analysis to extract key quantities, such as the atom number and optical depth.

Labscript is designed to be used in conjunction with a “pseudoclock” device, which is a variable frequency clocking device that only steps through instructions when a clocked device needs to update an output, rather than at a constant rate, eliminating unnecessary repetitive instructions [84]. In the rest of this chapter, I have included a publication that appears in Review of Scientific Instruments **92**, 055107 (2021) [86] that details the design of JQI AutomatioN for Experiments (JANE): a programmable system on chip (PSoC)-based pseudoclock device. This design was created in close collaboration with Alessandro Restelli. Alessandro taught me everything I know about electronics, and with his help, I wrote the code for the programmable logic of the PSoC, designed the carrier board and breakout boards for the digital inputs and outputs, and integrated it with Labscript. I wrote the manuscript, and all authors edited the manuscript.

## 3.2 Publication: Programmable System on Chip for controlling an atomic physics experiment

### 3.2.1 Abstract

Most atomic physics experiments are controlled by a digital pattern generator used to synchronize all equipment by providing triggers and clocks. Recently, the availability of well-documented open-source development tools has lifted the barriers to using programmable systems on chip (PSoC), making them a convenient and versatile tool for synthesizing digital patterns. Here, we take advantage of these advancements in the design of a versatile clock and pattern generator using a PSoC. We present our design with the intent of highlighting the new possibilities that PSoCs have to offer in terms of flexibility. We provide a robust hardware carrier and basic firmware implementation that can be expanded and modified for other uses.

### 3.2.2 Introduction

Laser-cooled atoms, ions, and molecules are interesting and dynamic systems to study, and are being used to develop many quantum technologies. These technologies include precise atomic clocks [12, 60], quantum computers and simulators [87, 88], and quantum sensors [89, 90]. Experiments in atomic, molecular, and optical (AMO) physics are often a combination of a large number of commercial or custom-made instruments from different sources and manufacturers that need to operate synchronously and in a repeatable fashion. Synchronization is achieved by using a specialized software suite to

control a primary digital pattern generator or clock device with deterministic timing that sends trigger signals to the other hardware devices. The PulseBlaster by SpinCore [91], a commercial device based on a field programmable gate array (FPGA), is commonly used as a primary clock in many AMO experiments [84] and is compatible with many different software suites. Many university groups have also designed custom-made devices based around a microcontroller or an FPGA as their primary clock. Microcontrollers combine processing power with many peripherals for interfacing directly with hardware, and have found use in a wide variety of physics experiments [92–95]. On the other hand, FPGAs provide versatility in modifying the overall system architecture to accommodate changes in functionality, although they require more expertise for development. Despite the steeper learning curve, FPGAs have become a common choice as a control device in many physics experiments and work extremely well to accommodate more complex architectures, as well as modular ones [96–100].

Another approach for controlling experiments is to create a complete infrastructure of software and modular hardware that is designed with built-in timing synchronization. Two commercial examples of this approach are LabView, a systems engineering software that is compatible with National Instruments hardware, and ARTIQ by M-labs [101], which is also a complete infrastructure of software and hardware. Some university research groups have also created complete architectures, basing their hardware designs off of FPGAs and designing custom control software [97, 99].

While FPGAs can work well as a primary control device for an experiment, microcontrollers offer a simpler solution for handling complex communications protocols such as USB (Universal Serial Bus) or Ethernet. Often, a microcontroller is used in conjunction with

an FPGA, either externally [84] or instantiated within the FPGA [101]. An alternative approach is to use a programmable system on chip (PSoC), which combines an FPGA and a high performance microprocessor on a single chip. This allows implementation of operating systems, advanced communication protocols, and high level language interpreters in the microprocessor, leveraging the FPGA when hardware acceleration or control of dedicated peripherals is needed. Previously, development using PSoCs has been less accessible due to the baseline level of expertise required, but recently, thanks to the diffusion and level of maturity of tools such as PetaLinux [102] or Yocto Project [103] for the generation of GNU/Linux images, PSoCs have become more widely adopted [104, 105].

We chose a PSoC architecture to design our 64-channel pattern generator and primary clock with the goal of expanding the capabilities of our ultracold strontium experiment. Our requirement, to have a large number of channels operating in parallel with fast (100 ns resolution) and deterministic timing, points towards an FPGA as the platform of choice; however, we also had the goal of handling most of the data communication protocols using high level abstraction languages, such as Python, to facilitate testing and future rapid development. To achieve these goals, we take advantage of the PYNQ (Python Productivity for Zynq) infrastructure [106], a platform for the development of applications with the Xilinx Zynq series of programmable systems on chip based on GNU/Linux and Python. Our lab uses the Labscript Suite of software [84] to control our experiment, which uses a text and GUI approach to provide efficient experimental control for atomic physics experiments and is based on the Python programming language. We designed a hardware platform around a Microzed Zynq-7020 module [107] (produced by Avnet) mounted on a

custom carrier board with four low-jitter input trigger lines and eight breakout boards with eight channels each to route the 64 output lines. The FPGA gateway is written in Verilog and System Verilog, and we used Xilinx native development tools in order to make use of the many verification features, such as complex testbenches for behavioral simulation. In the next sections, we will describe the system architecture as a whole, as well as describe the hardware and firmware in detail.

### 3.2.3 System Overview

Fig. 3.2 illustrates the overall architecture of our design, which can be broken down into three blocks: our host PC (or lab control computer), the Microzed-7020 module, and the carrier and breakout boards. The Microzed module contains the Xilinx PSoC and a series of additional peripherals, of which we show only the most relevant to our project: the I/O connectors to interface with the carrier board, 1 GB of synchronous dynamic random access memory (SDRAM), and an Ethernet physical layer chip (PHY) used for communication with the host PC. The PSoC (Xilinx XC7Z020-1CLG400C [108]) is composed of the processing system (PS) and the programmable logic (PL). The PS is a dual core ARM Cortex-A9, while the PL is an Artix-7 FPGA fabric with approximately 85000 logic cells.

The PYNQ ecosystem allows us to run Linux Ubuntu on the PS and is equipped with a Jupyter notebook server accessible from a remote machine browser as a means to interact with the PL using a Python application programming interface (API). Through the API, the PL can be accessed using extended multiplexed input/output lines (EMIO) or an

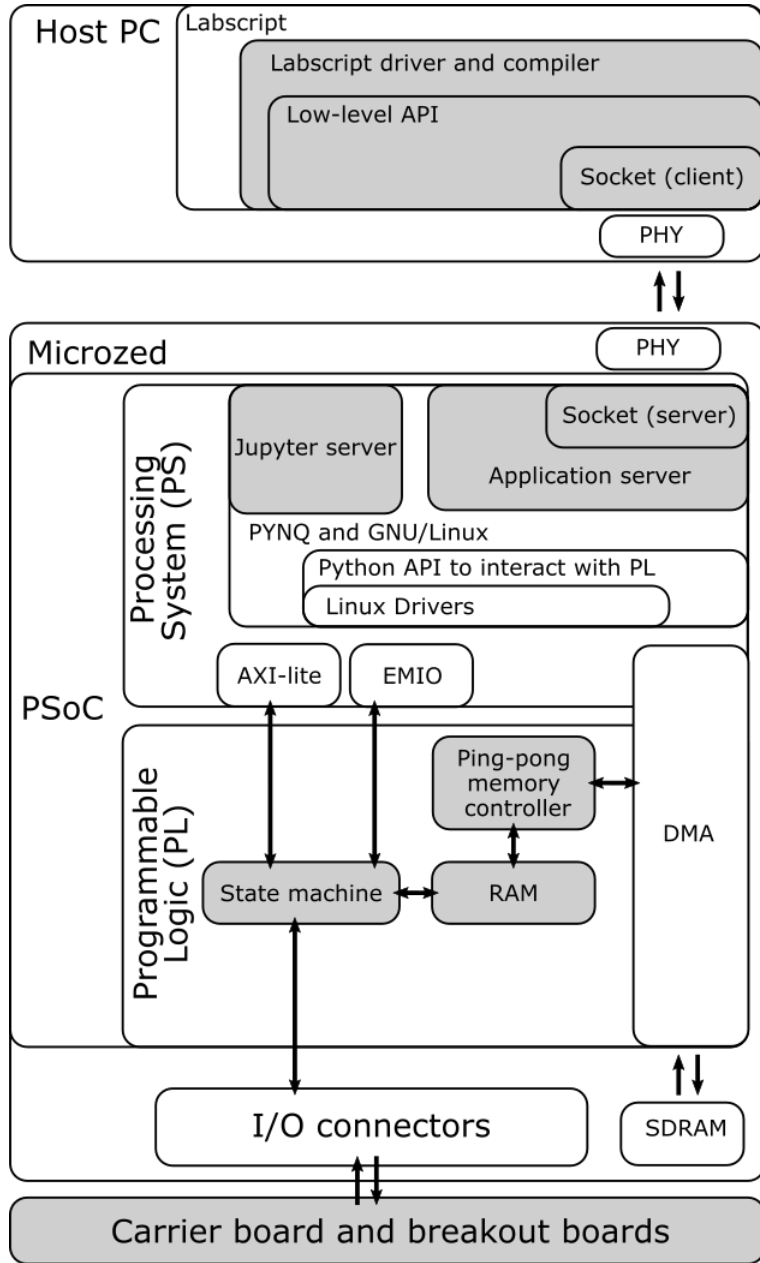


Figure 3.2: Overall schematic of the pattern generator. For convenience, we summarize acronyms used in the figure: PC (Personal Computer), API (Application Programming Interface), PHY (PhYsical interface), PSoC (Programmable System on Chip), PS (Processing System), PL (Programmable Logic), AXI (Advanced eXtensible Interface), EMIO (Extended Multiplexed Input/Output), DMA (Direct Memory Access), RAM (Random Access Memory), I/O (Input/Output), SDRAM (Synchronous Dynamic RAM). Elements of the system we designed in detail are shown in gray, while the white blocks are the components and software that are available as commercial modules, open-source libraries, or automatic software generation tools.

AXI-lite (Advanced eXtensible Interface) channel that can be used to map configuration registers in the PL to the operating system's RAM. Additionally, the SDRAM external memory used by the operating system can be accessed using a direct memory access (DMA) controller.

The heart of our design is in the PL, where we implemented a state machine written in System Verilog which reads instructions from RAM instantiated in the FPGA fabric. The RAM is limited to  $2^{15} = 32768$  instructions. To allow for a longer list of instructions, we have implemented a ping-pong memory controller that moves data from the external SDRAM to the PL RAM through the DMA channel. The state machine and ping-pong memory controller will be discussed in further detail in Sections [3.2.5.2](#) and [3.2.5.3](#), respectively.

In the PS, we wrote an application server in Python to receive instructions from the host PC through a socket connection, transferring them to the shared SDRAM and initiating DMA transfers. The application server is paired with a socket client running on the host PC, also written in Python, which acts as a low-level API to interface the Labscript instrument driver with the Microzed module.

The Microzed board plugs into a custom-designed carrier board using MicroHeader connectors. The output signals are then routed through eight breakout boards and are accessible via BNC (Bayonet Neill–Concelman) connectors. The carrier board and breakout board designs are described in Sec. [3.2.4](#).

## 3.2.4 Hardware Features

### 3.2.4.1 Carrier Board

The carrier PCB (Printed Circuit Board) routes the 64 digital output lines from the expansion connectors of the Microzed module (Amphenol ICC 61083-101400LF) to eight 20-pin rectangular connectors, which are used to distribute the signals to the breakout boards using ribbon cables. Placement of the 20-pin rectangular connectors was determined to keep the difference in length between all traces below 12 mm. The resulting maximum difference in propagation time between channels is estimated to be only  $\approx 64$  ps, which is well within the goals of our design. The carrier board also has four BNC connectors for introducing input clock or trigger signals to the Microzed. In order to adapt arbitrary trigger and clock standards to the FPGA input standards, each BNC input is connected to the analog front end circuit shown in Fig. 3.3(a). Input signals are sent through a high speed comparator chip (ADCMP552BRQZ [109]) with PECL (Positive Emitter-Coupled Logic) outputs. We set a 1 V threshold on the inverting input of the comparator using a voltage divider filtered with a  $0.1 \mu\text{F}$  capacitor, and we connect the coaxial input to a network of components (R1, R2, R3, C1, C2) that can be used to adapt a variety of AC (Alternating Current) or DC (Direct Current) input waveforms. R1 is used as jumper to select between DC and AC inputs. In the default DC-coupled configuration,  $R1 = 0 \Omega$  and  $R3 = 50 \Omega$ , making the input compatible with 3.3 V and 5 V TTL (Transistor Transistor Logic) standards. For an AC-coupled configuration, R1 is not placed,  $C1 = 0.1 \mu\text{F}$  to block DC signals, and the values,  $R2 = 294 \Omega$  and  $R3 = 60.4 \Omega$ ,

set the input impedance to  $50\ \Omega$ , maintaining an average voltage of  $0.85\ \text{V}$  at the input of the comparator. The carrier board also provides a  $3.3\ \text{V}$  supply for the I/O banks of the PSoC with two high-efficiency micro DC-DC converters (XCL214 [110]), and a supervisor chip (STM6779LWB6F [111]) ensures that the required power sequencing for the PSoC is respected [112].

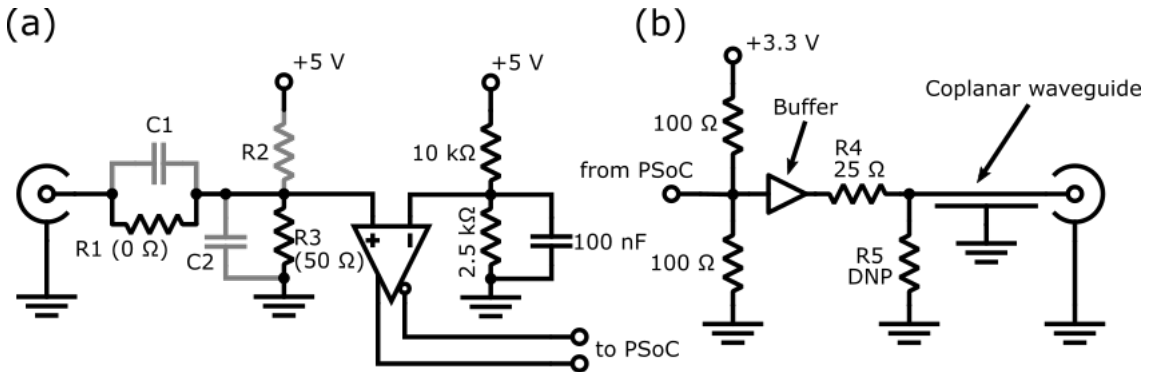


Figure 3.3: Termination networks used to interface the FPGA logics with external signals. (a) shows the circuit used for the four digital inputs on the carrier board while (b) shows the circuit used for the 64 digital outputs.

### 3.2.4.2 Breakout Boards

The eight breakout boards use a Texas Instruments octal buffer (SN74S244DWG4 [113]) to drive  $5\ \text{V}$  TTL signals through  $50\ \Omega$  coaxial cables. The electrical schematic for a single channel is shown in Fig. 3.3(b). The ribbon cable connecting the carrier board with the breakout board has an alternating pattern of GND lines and digital signal lines, which prevents crosstalk and sets a characteristic impedance of  $50\ \Omega$ . The ribbon cable also carries a  $3.3\ \text{V}$  supply used for termination and a  $5\ \text{V}$  supply used to power the octal buffer. The two  $100\ \Omega$  resistors in Fig. 3.3(b) terminate the single-ended line from the PSoC to a Thevenin equivalent of  $50\ \Omega$  at half the logic supply. This type of termination is

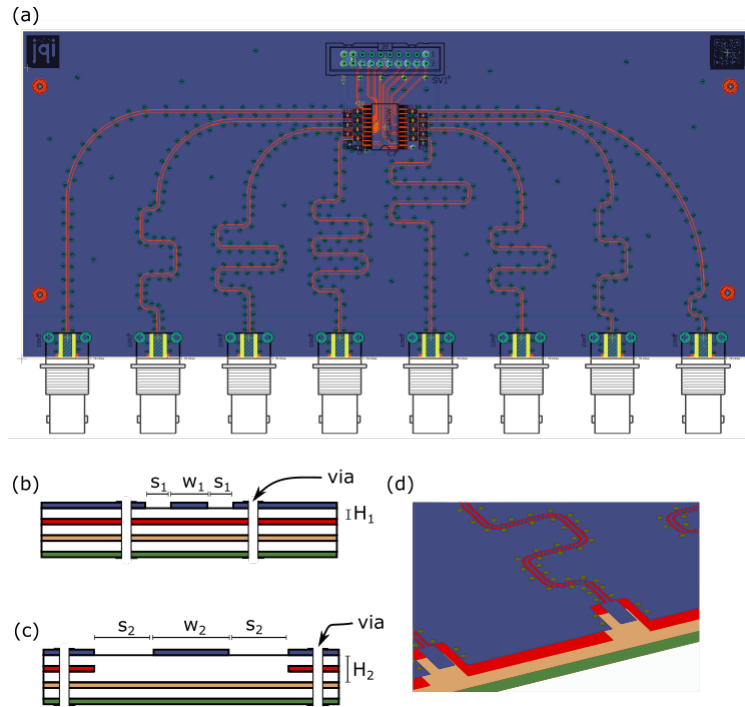


Figure 3.4: (a) Breakout board layout. Signals enter the board through the 20-pin connector at the top. Meanders help equalize electrical delays of all traces. (b) Stack-up of the PCB for the coplanar waveguide (c) Stack-up of the PCB for the microstrip below the BNC connector. (d) Close-up perspective view of the circuit board layout. Figure is not to scale.

called split termination and is described on page 26 of the Xilinx UG471 user guide [114].

Each output of the octal buffer has an internal impedance of  $25\ \Omega$ , and therefore a series resistance of  $25\ \Omega$  (R4) is added in order to bring the output impedance to a standard value of  $50\ \Omega$ . The additional DNP (do not place) resistor (R5) can be used in conjunction with a different value for R4 to produce an arbitrary Thevenin equivalent output that maintains a  $50\ \Omega$  impedance, allowing the user to configure the outputs to different logic standards. For example, the values  $R4 = 75\ \Omega$  and  $R5 = 100\ \Omega$  would reduce the output voltage by a factor of 2. The coplanar waveguide in Fig. 3.3(b) is designed with a target impedance of  $50\ \Omega$  using the Kicad PCB calculator [115] software.

Fig. 3.4(a) shows how the eight coplanar waveguides are arranged on the breakout

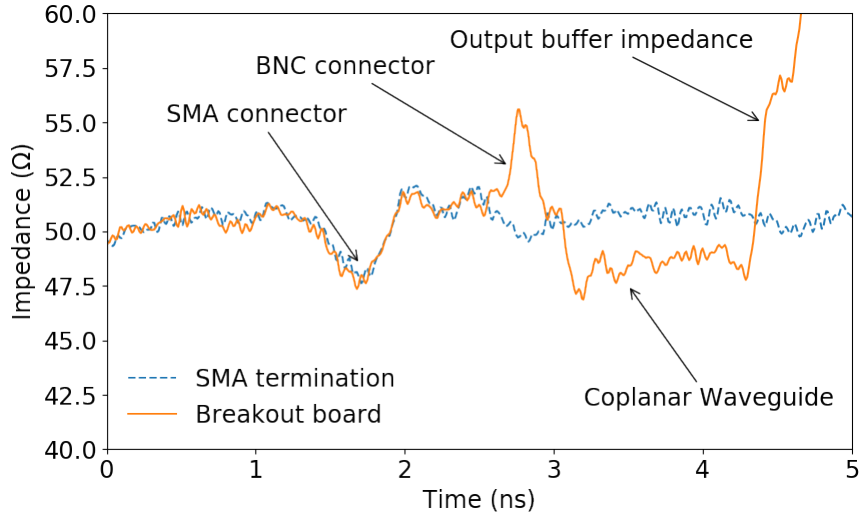


Figure 3.5: Time Domain Reflectometry measurement of the breakout board. The characteristic impedance of the BNC connector and coplanar waveguide remain within 10% of the  $50\ \Omega$  target value.

board. To prevent variations in the timing delay across different output channels, we have matched the length of all 8 traces using meanders. Based on the information provided by the PCB manufacturer (nominal relative dielectric constant  $\epsilon_r = 4.3$ ), we designed the coplanar waveguide, as illustrated in Fig. 3.4(b), with a width  $W_1 = 0.46\ \text{mm}$ , spacing between traces and top-layer ground plane  $S_1 = 0.3\ \text{mm}$ , and separation from top-inner-layer ground plane  $H_1 = 0.24\ \text{mm}$ . We chose edge-mount BNC connectors rated up to 4 GHz to minimize the characteristic impedance discontinuity from the PCB to the coaxial cables. For impedance matching, the connectors need to be soldered to a microstrip that ends at the edge of the PCB. However, to ensure an adequate mechanical strength for the connector’s central pin soldering joint, the width of the microstrip must be much larger than the width  $W_1 = 0.46\ \text{mm}$  of the coplanar waveguide in Fig. 3.4(b). To allow for a wider section of the transmission line, we therefore remove the inner-top ground layer from under the central pin’s soldering pad, as shown in Fig. 3.4(c). Using the inner-

bottom layer as the new ground plane, the distance from the transmission line is increased to  $H_2 = 1.26$  mm. A nominal  $50\ \Omega$  impedance is now obtained with  $W_2 = 2.29$  mm and  $S_2 = 1.27$  mm. A perspective view of the PCB layers is shown in Fig. 3.4(d).

We verified the performance of the transmission lines and BNC launch by performing a time domain reflectometry (TDR [116]) measurement on the PCB. The result of the measurement is shown in Fig. 3.5, where we use the technique described in Ref. [116] to measure the amplitude of a reflected step signal to calculate the characteristic impedance along a transmission line as a function of electrical delay. We first measure the response of a coaxial cable with an SMA (SubMiniature version A) connector attached to a SMA  $50\ \Omega$  termination. We then connect the coaxial cable to our PCB board, while not powered, using a SMA to BNC adapter and compare the two TDR responses. Four different sections can be distinguished in the traces in Fig. 3.5: the SMA connector, the BNC adapter, the coplanar waveguide on the PCB, and the output buffer passive impedance. Apart from the output buffer, which shows a change of impedance compatible with a capacitive load, the maximum impedance variation for the BNC connector and coplanar waveguide design is below  $\approx 10\%$ , limiting reflections below  $\approx 5\%$ .

## 3.2.5 Firmware Development

### 3.2.5.1 Communication

To communicate instructions to the PSoC, we open a socket server on the PS. We then wait for the TCP/IP client on the lab computer to connect. Once the connection is established, data is sent through the socket stored in a numpy array [117], which

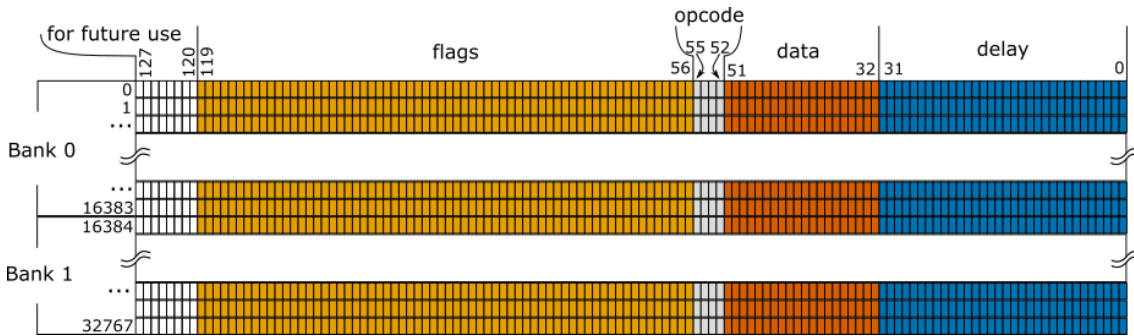


Figure 3.6: Illustration of the memory in the FPGA. The memory is split into Bank 0 and Bank 1, each with 16834 instructions. The memory has a width of 128 bits. Each instruction contains 64 bits for the state of each of the flags, 4 bits for the opcode, 20 bits for the data argument, and 32 bits for the time delay argument. The last 8 bits are left unused, but can be allocated in the future.

is mapped on a contiguous section of SDRAM shared with the PL through a DMA controller. The data is then accessed by the PL and processed by the state machine as instructions in a 128 bit format extension of the 80 bit long instruction format used in the PulseBlaster [118]. In case the connection is unexpectedly broken, we have implemented an algorithm for the server to automatically refresh the same socket connection, instead of creating a new one. This makes the system robust against the interruption of the connection without having to manually reset it.

### 3.2.5.2 State Machine

To control the 64 TTL output channels, we have written a Mealy [119] state machine in the programmable logic of the FPGA. In contrast with Moore [120] state machines, Mealy state machines' inputs directly affect the outputs, allowing for a lower-latency design. We wrote our state machine in System Verilog to take advantage of specialized features of the language, such as enumeration logic and the passing of structured data through design modules. The state machine first fetches 128 bit instructions from a

State	Instruction	Data	Function
0	CONTINUE	None	Continues to next instruction
1	STOP	None	Stops execution of program
2	LOOP	Number of desired loops, great than or equal to 1	Specifies beginning of loop
3	END LOOP	Address of beginning of loop	Specifies end of loop
4	JSR	Address of first subroutine instruction	Jumps to a subroutine
5	RTS	None	Program execution returns to instruction after JSR was called at the end of subroutine
6	BRANCH	Address in memory to branch to	Program execution branches to an address specified by data
7	LONG DELAY	Delay multiplier	Executes the length of instruction given in the time field multiplied by delay multiplier
8	WAIT	None	Waits for a hardware trigger to continue program execution

Table 3.1: List of states that was programmed in the state machine with associated data field and description of the function performed. The state numbering corresponds to the associated opcode.

128x32768 RAM, mapped as shown in Fig. 3.6. There are five fields that make up the 128 bit instruction to the state machine: time delay (32 bits), data (20 bits) opcode (4 bits), flags (64 bits) and finally the remaining 8 bits are reserved for future use. The state machine reads the memory bank row by row. The opcode tells the state machine which state to enter next, and the flags field designates which output channels will be changed or affected with each instruction. The data contains any special information specific to the current opcode. For example, if the state machine is being instructed to enter a

loop, the data would contain the number of loop iterations. Finally, the ‘delay’ argument indicates how long the state machine should wait before loading the next instruction. The states that we have programmed in our state machine are shown in Table 3.1, along with the accompanying ‘data’ field. To facilitate integration with Labscript, we choose an instruction set that is mostly compatible with the one of the Pulseblaster, which is extensively used within the Labscript codebase (we did not implement nested loops, as they are not used in Labscript).

### 3.2.5.3 Ping-Pong Memory

The state machine described in the previous section is designed to read instructions from a 32768-instruction static memory. To increase the available memory, we use the 32768-instruction space as a cache memory and divide it into two banks with  $2^{14} = 16384$  instructions each: Bank 0 and Bank 1, as shown in Fig. 3.6. We then implement a ping-pong memory controller to automatically update the content of the memory by requesting direct memory access (DMA) to a large shared contiguous portion of the SDRAM, which has space for up to 8192000 instructions. The algorithm for the ping-pong memory controller is shown in Fig. 3.7(a). The controller begins by transferring 16384 instructions from SDRAM into Bank 0 of the PL RAM and setting a register called “last\_bank” equal to 1. The main state machine then begins executing instructions from RAM, starting from Bank 0, while the ping-pong memory controller constantly monitors the memory address. Each time the memory address is not in the bank identified by the register “last\_bank”, the previously accessed bank is refreshed with new data from the SDRAM

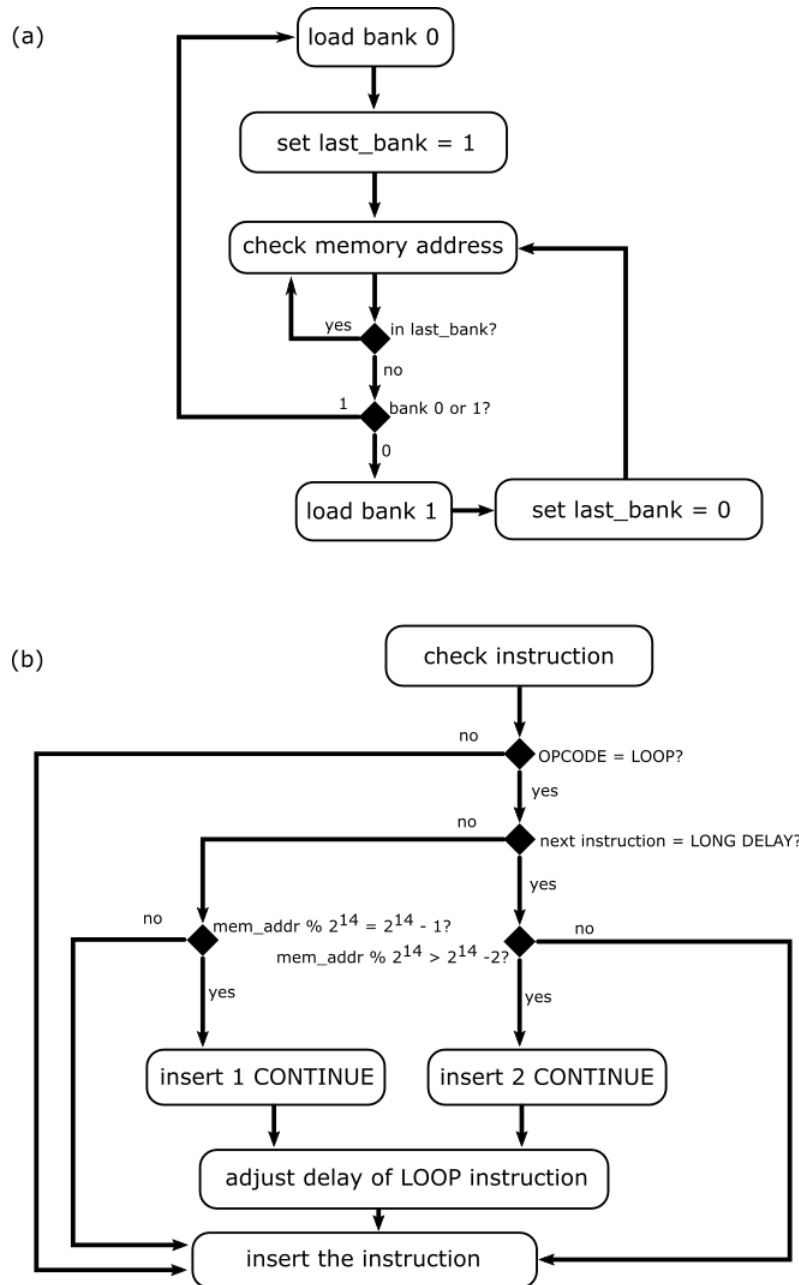


Figure 3.7: Bank switching and compiler check algorithms for the ping-pong memory controller. (a) The system begins by loading bank zero and setting the “last\_bank” to Bank 1. From there, the system consistently checks the memory address of the state machine to determine whether it has switched banks in the memory. If it has switched banks, it changes “last\_bank” and loads the other bank of memory with new instructions. (b) Checks performed during compilation to avoid memory underflow. The logic expressions  $\text{mem\_addr} \% 2^{14} > 2^{14} - 2$  and  $\text{mem\_addr} \% 2^{14} = 2^{14} - 1$  check, respectively, if  $\text{mem\_addr}$  is mapped to the last two slots or the last slot in the memory bank ( $\%$  is the MOD operator).

and the value of “last\_bank” is updated with the identifier of the currently accessed bank. Setting “last\_bank” equal to 1 when the state machine starts causes Bank 1 to be updated immediately after Bank 0 as soon as the state machine accesses the memory. The PL RAM is a dual port memory that can be independently addressed from two different clock domains. Thus, the state machine controlling the 64 TTL outputs does not need to be synchronous with the rest of the PL and with the PS. The ping-pong memory controller and DMA engine are clocked by the PS, while the state machine can be optionally clocked from one of the PLLs (Phase Locked Loop) available in the PL fabric that can be locked to an external reference connected to one of the four available BNC inputs.

The automatic RAM refresh implemented by the ping-pong memory controller can pose a problem if certain instructions span over two banks, such as LOOP/END LOOP, BRANCH, JSR/RTS. For example, if a loop is started in the first bank, but ends in the second bank, since the first bank is updated with new instructions while the second bank is running, the system will no longer have the initial loop instruction to refer back to. The compiler must be aware of this type of memory bank underflow or overflow and be able to resolve them by altering the order and number of instructions, without changing the final behavior at run time. In the current Labscript driver, there is only one instance where underflow can happen: when the complex instruction called “reps” is translated into either a LOOP immediately followed by an END LOOP instruction or a series of LOOP, LONG DELAY, END LOOP. To prevent memory underflow, we have implemented checks in the code while the program is compiling. The algorithm is illustrated in Fig. 3.7(b). When a LOOP opcode is found, the system checks if either the instruction is mapped on the last instruction of a bank or if it is mapped on the second to last and is immediately

followed by a LONG DELAY instruction. In these cases, it inserts additional CONTINUE instructions to ensure that the LOOP instruction is moved to the beginning of the next bank. To ensure that the insertion does not modify the original timing, the field ‘delay’ in the LOOP instruction is reduced by the duration of the inserted CONTINUE instructions.

### 3.2.6 Discussion

The PSoC-based primary clock device, that we have created for controlling AMO physics experiments, is easily integrated with the Labscript Suite. The hardware provides 64 buffered digital outputs for controlling other hardware devices and also 4 input trigger channels. The printed circuit board design ensures signal integrity and minimal crosstalk between channels. Our firmware design implements a state machine written in System Verilog and a ping-pong memory controller that allows the execution of a large number of instructions (exceeding 8192000). The system is currently being used to run the entire experiment in our lab, providing triggers for digital to analog converters (DAC), digital direct synthesizers (DDS), mechanical shutters, and many other instruments.

According to the Synthesis tools timing reports the maximum frequency the state machine can operate at is 104 MHz, and it is currently clocked at 100 MHz. Therefore, the current timing resolution is 10 ns, although using serializers in the PL fabric would allow timing resolutions down to 1 ns. The versatility of the platform also allows for other modifications, such as the possibility to add additional instructions to the state machine. For example, an additional instruction could initiate a train of a specific number of pulses with an adjustable duty cycle and period using a single instruction, rather than using

loops. Other extensions of the instruction set could allow for conditional branching, which has already been shown to be useful in ion trapping experiments [121]. Further modifications to the design might include network security protocols and encryption for data transmission, which we have not included since our setup is running on an isolated network. A possible use of the system we have considered, and have extensively taken advantage of during testing, is its capability to run scripts directly from the local Jupyter notebook server. With the Jupyter web interface, a remote computer is not necessary for the generation of patterns, and the device can be used as a stand-alone testbench digital pattern generator.

Our PSoC-based primary clock device has the capability to be integrated with many experimental setups with minimal modification, and the whole design is available online [122].

## Chapter 4: Experimental Procedure

### 4.1 Blue MOT

#### 4.1.1 Experimental Sequence

In this chapter, we will discuss the experimental sequence and the procedure for getting each stage of the experiment to work. We start the blue MOT stage with the magnetic field gradient at around 55 G/cm and the blue MOT beams at their maximum power of around 9 mW per beam. After letting the MOT load for a little over 3 s, we employ a “Doppler cooling” phase in which we ramp the field gradient up to around 58 G/cm and the power in the MOT beams down to 0 mW over a span of approximately 0.2 s. This has the effect of further confining the atoms in the blue MOT and cooling them down as much as possible before transfer to the red MOT. With this experimental sequence, we achieve temperatures in the  $\sim$  mK range. The repump lasers remain on for this entire period of time. The normalized power in the blue MOT beams and the magnetic field gradient during the blue MOT stage are shown as a function of time in Fig. 4.1. We trap around  $1 \times 10^8$  atoms in the blue MOT using this experimental sequence.

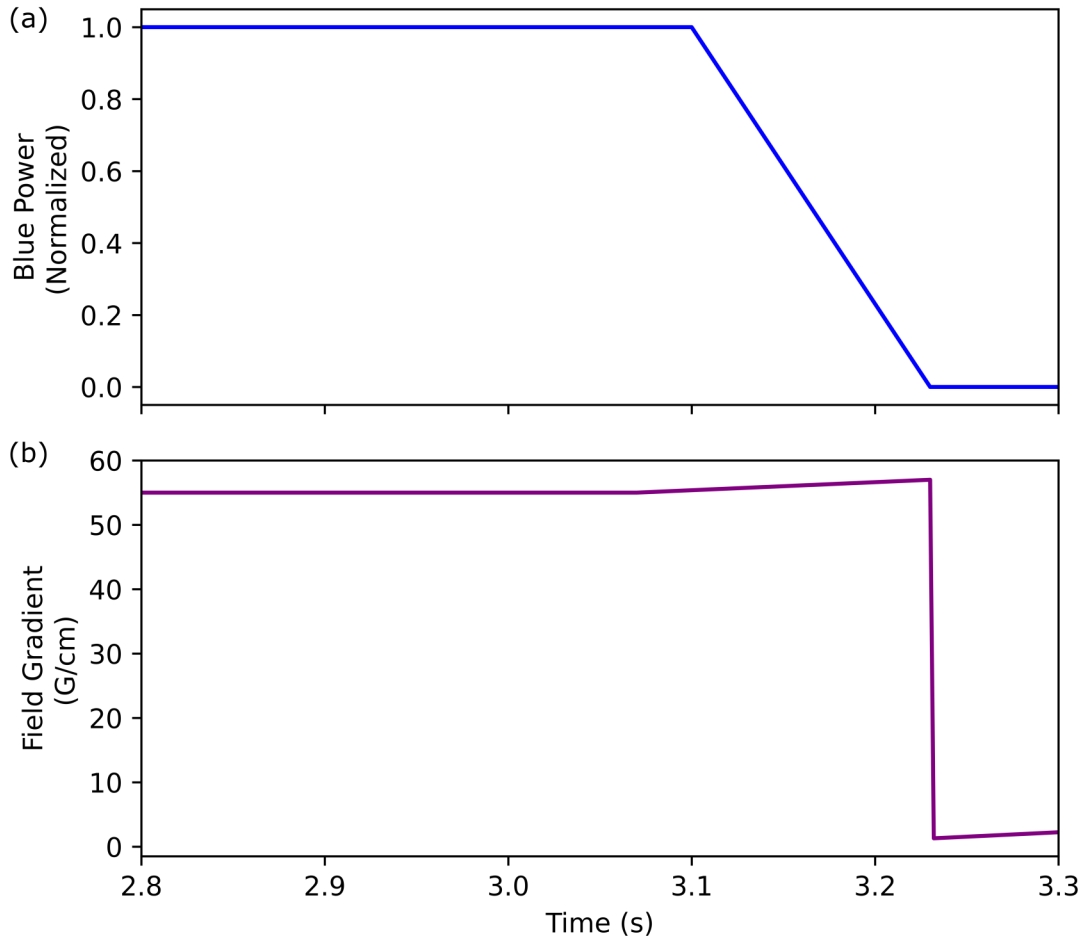


Figure 4.1: Normalized power in the blue MOT beams and the magnetic field gradient during the blue MOT stage of the experimental sequence as a function of time. (a) Power in the blue MOT beams starts at its maximum value of  $\sim 9$  mW per beam. At around 3.1 s into the experimental shot, we ramp the power down to 0 mW as part of the “Doppler cooling” stage. (b) The magnetic field gradient starts at 55 G/cm and at 3.1 s is ramped to approximately 58 G/cm. The field is then rapidly lowered to approximately 1.3 G/cm.

#### 4.1.2 Absorption Imaging

To image our atoms, we use absorption imaging. Absorption imaging involves interrogating an atomic cloud with probe light resonant with an atomic transition and taking an image of the shadow cast by the atoms with a CCD camera. In our experiment we take three images as part of the experimental sequence: an image of the probe light

with no atoms, an image of the shadow caused by the atoms absorbing probe light, and an image of the background when no probe light or atoms are present. With these three images, we are able to extract the optical depth (OD) of the atomic cloud. We perform near-resonant absorption imaging on the strong  $^1S_0 \rightarrow ^1P_1$  transition. The decrease in intensity of the light transmitted through the atomic cloud is given by the Beer-Lambert Law for a two-level system [123, 124]:

$$\frac{dI(x, y, z)}{dy} = -n(x, y, z)\sigma_0 \frac{I(x, y, z)}{1 + (I(x, y, z)/I_{sat}) + (2\delta/\Gamma)^2} \quad (4.1)$$

In Equation 4.1,  $I_{sat} = 3\lambda^2/2\pi$  is the saturation intensity of the transition,  $\delta$  is the detuning of the probe beam,  $\Gamma$  is the natural linewidth of the transition,  $\sigma_0 = \pi hc\Gamma/3\lambda^3$  is the absorption cross-section,  $n$  is the atomic cloud density, and  $\hat{y}$  is the axis along which the probe light propagates. In the case of a low-intensity, resonant probe,  $I \ll I_{sat}$  and  $\delta = 0$ , and the Beer-Lambert law simplifies to:

$$\frac{dI(x, y, z)}{dy} = -n(x, y, z)\sigma_0 I(x, y, z) \quad (4.2)$$

Taking the integral of both sides of Eq. 4.2, we get:

$$n_{2D}(x, z)\sigma_0 = -\ln\left(\frac{I_f(x, z)}{I_0(x, z)}\right) \quad (4.3)$$

Here,  $n_{2D}(x, z) = \int n(x, y, z)dy$  is the column density,  $I_0$  is the intensity of the probe light before the atomic cloud, and  $I_f$  is the intensity after the atomic cloud. Using our three images taken during the experimental sequence of the atoms ( $I_a$ ), probe ( $I_p$ ), and

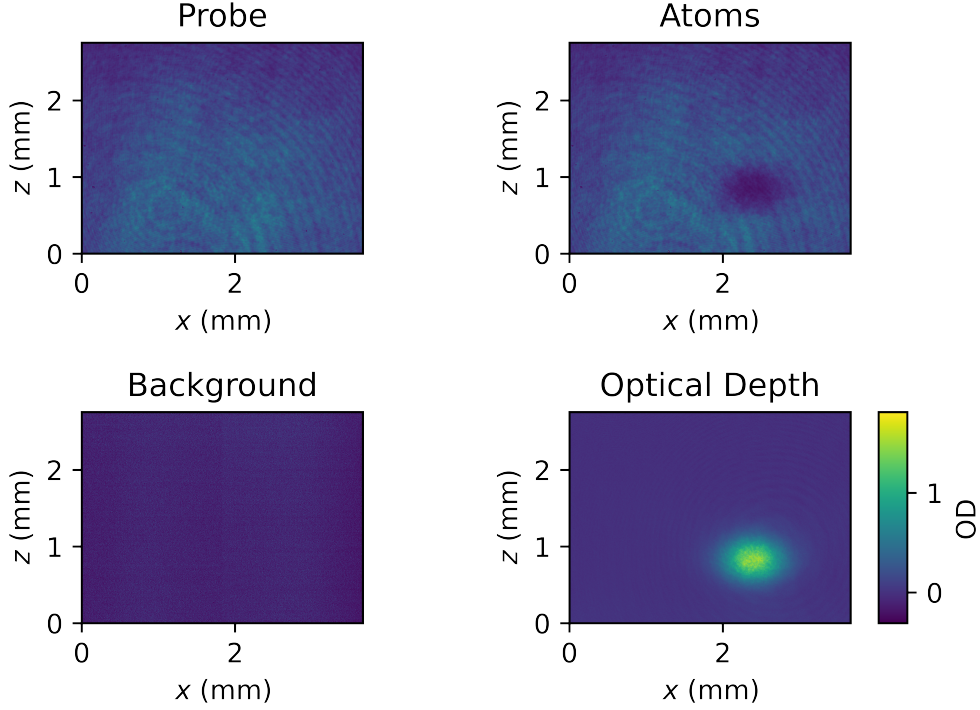


Figure 4.2: Example of absorption imaging with 20 ms time of flight. The probe, atoms, and background images are all taken with a CCD camera during the experimental shot. The shadow created by the atoms absorbing the probe light can be seen in the top right “Atoms” image. The optical depth is calculated according to Eq. 4.4 to generate the bottom right image. This imaging system is in the  $\hat{x} - \hat{z}$  plane.

background ( $I_b$ ), we get  $I_f(x, z) = I_a(x, z) - I_b(x, z)$  and  $I_0(x, z) = I_p(x, z) - I_b(x, z)$ .

With the optical depth defined as  $OD = n_{2D}(x, z)\sigma_0$ , we can write Eq. 4.3 as

$$OD = -\ln \left( \frac{I_a(x, z) - I_b(x, z)}{I_p(x, z) - I_b(x, z)} \right) \quad (4.4)$$

Typically, we allow the atomic cloud to expand in time of flight until the shape of the cloud resembles a Gaussian profile ( $\sim 1$  ms for the blue MOT). Using the optical depth, we can calculate the number of atoms by using an iterative process of taking slices of the OD image until the center of the atomic cloud is found and then taking a Gaussian fit  $f(x) = ae^{-(x-c)^2/2w^2}$  along the  $\hat{x}$  and  $\hat{z}$  directions, shown in Fig. 4.3. The number

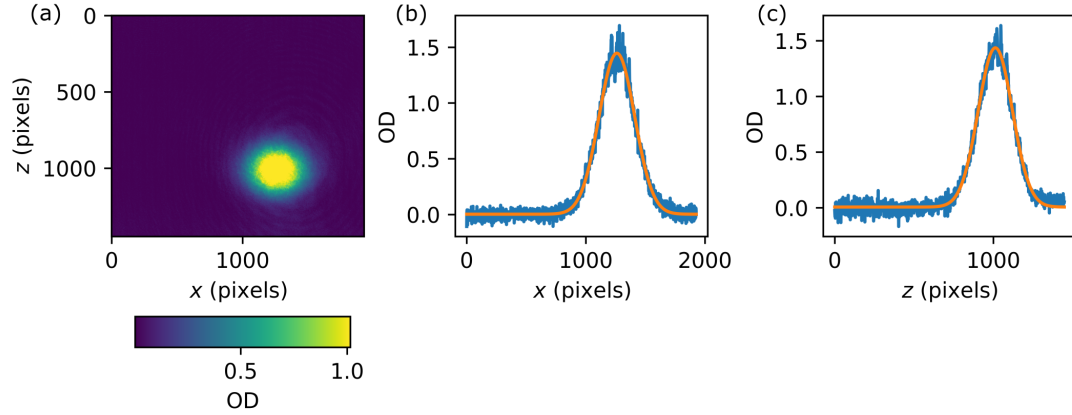


Figure 4.3: Example of Gaussian fitting of the atomic cloud in the  $\hat{x}$  and  $\hat{z}$  directions to extract parameters such as the center position of the cloud, the width of the cloud along both axes, and the number of atoms in the sample. (a) Image of optical depth of the atomic cloud with 20 ms time of flight. (b) Gaussian fit of the OD along the  $\hat{x}$  axis. (c) Gaussian fit of the OD along the  $\hat{z}$  axis.

of atoms in the atomic cloud can then be calculated as  $N = \pi w_x w_z (a_x + a_z) / \sigma_0$  [125], where  $w_x, a_x$  and  $w_z, a_z$  are the width and amplitude parameters from the Gaussian fits in the  $\hat{x}$  and  $\hat{z}$  directions, respectively, and the pixel size/magnification of the imaging system has been taken into account when calculating the widths.

## 4.2 Red MOT

### 4.2.1 Experimental Sequence

To transfer atoms from the blue MOT to the red MOT, we must lower the magnetic field gradient from 58 G/cm to around 1 G/cm very quickly (i.e. in under 1 ms). Our PI controller for the current flowing through the magnetic field coils is able to command the current down to 1.3 G/cm in around 200  $\mu$ s. When operating the experiment using the IGBT, we open the IGBT while sending an exponential decay that matches the natural

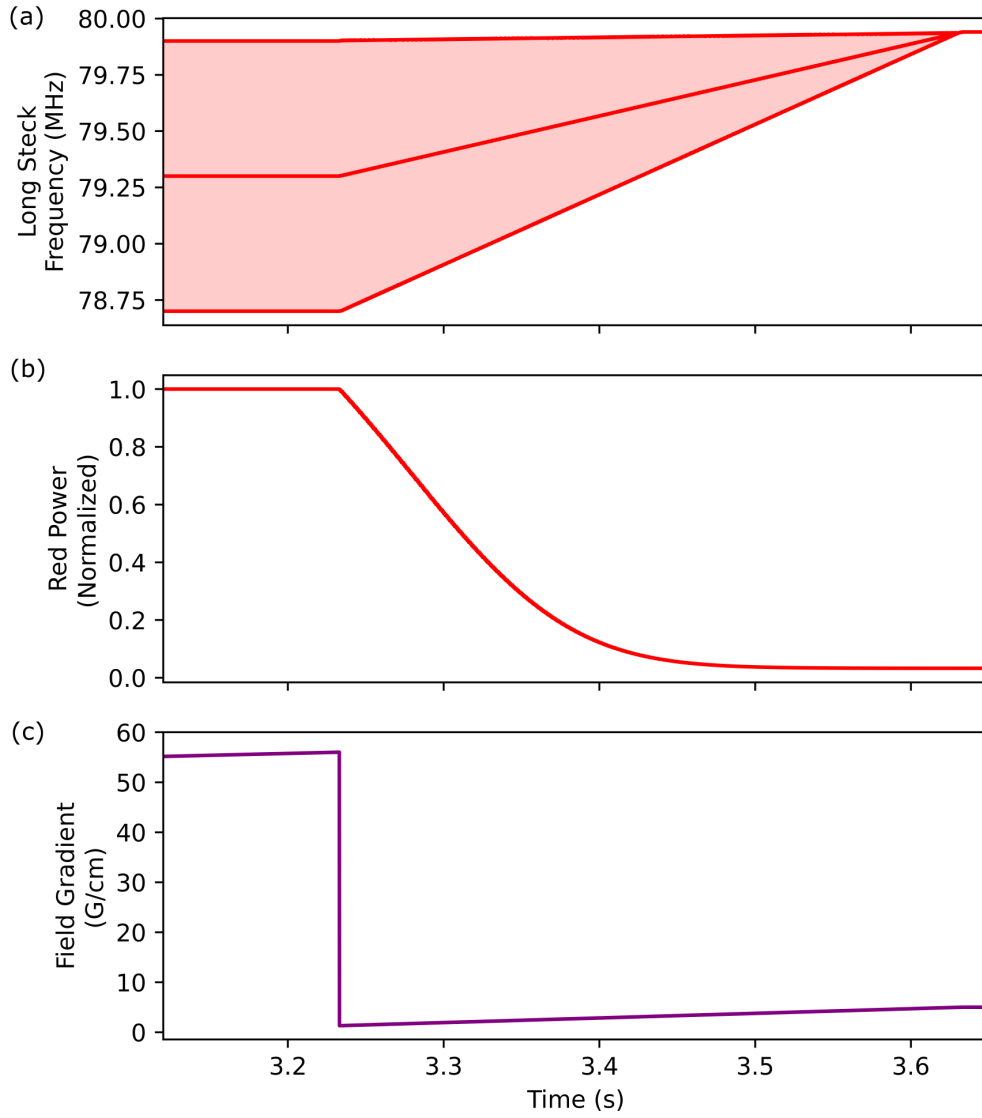


Figure 4.4: Red cooling (stirring) laser frequency and power for  $^{88}\text{Sr}$  ( $^{87}\text{Sr}$ ) and magnetic field gradient over time during the red MOT stage. (a) Long Stack laser frequency in MHz during the red MOT stage. This laser acts as the cooling laser for the bosonic isotopes and the stirring laser for the fermionic isotopes. The frequency is modulated over a width of approximately 1.2 MHz initially during the red MOT loading. The modulation amplitude is ramped down to 0 MHz over approximately 0.4 s for red MOT compression. (b) Long Stack laser power during the red MOT stage. The power starts at its maximum value of approximately  $900 \mu\text{W}$  per beam and is ramped down to  $0 \mu\text{W}$  at the end of the red MOT stage. (c) Magnetic field gradient during the red MOT stage. During the Doppler cooling stage, the field gradient is ramped up to 58 G/cm. To transfer atoms to the red MOT, the field gradient is rapidly dropped to around 1.3 G/cm in around  $200 \mu\text{s}$  and then ramped up to 5 G/cm for compression of the red MOT.

decay of the current as the PI control signal, as described in Ch. 2. We begin the red MOT loading phase with the frequency of the red cooling laser modulated over a span of approximately 1.2 MHz. Once the magnetic field gradient is dropped to 1.3 G/cm, we start to ramp the modulation amplitude of the red laser frequency down and the power in the red MOT beams down (from an initial 900  $\mu\text{W}$  per beam) over around 0.4 s, shown in Fig. 4.4. During this time, after hitting the low value of 1.3 G/cm, the field gradient is ramped back up to around 5 G/cm. This process of narrowing the frequency, lowering the power, and slightly increasing the field gradient allows us to initially capture atoms from as many velocity classes as possible, but then compress and cool them down to  $\sim \mu\text{K}$  temperatures.

#### 4.2.2 Electron Shelving Spectroscopy

Because the red MOT magnetic field gradient is so small, it is very important to cancel out any stray magnetic fields that are present in the lab, as they are no longer negligible. To cancel out stray fields, we use shim coils in a Helmholtz configuration along the  $\hat{x}$ ,  $\hat{y}$ , and  $\hat{z}$  directions. We used electron shelving spectroscopy as a diagnostic to determine the necessary magnetic fields that the shim coils must provide to cancel out stray fields. We follow the procedure presented in Ref. [126]. Atoms are loaded into the blue MOT and then transferred to the red MOT. Once a red MOT is formed, the atoms are released (the magnetic field and laser light are turned off) and then the atoms are supplied with a short pulse from the red MOT beams (around 20  $\mu\text{s}$ ), optically pumping them from the  $^1\text{S}_0$  to the  $^3\text{P}_1$  state, before imaging the atoms. We scan the frequency of the red MOT

laser over a range of around 50 MHz during the short pulse over several experimental shots and record the number of atoms in each shot. If there is a stray magnetic field present at the center of the trap, the Zeeman sublevels of the excited state will not be degenerate, and we will see resolved dips in the atom number for each  $m_J$  sublevel. After adjusting the shim fields and when the stray magnetic fields are cancelled, only a single dip feature will be present in the spectroscopy scan.

### 4.2.3 Red MOT Search

Another diagnostic that we used when attempting to transfer atoms from the blue MOT to the red MOT was qualitatively looking at the absorption images of residual blue MOT atoms around 5 ms after release and with the single-frequency red MOT light pulsed on. Because of the narrow linewidth of the  $^1S_0 \rightarrow ^1P_1$  transition, when the frequency of the red MOT laser is not modulated, the light is only resonant with a narrow velocity class

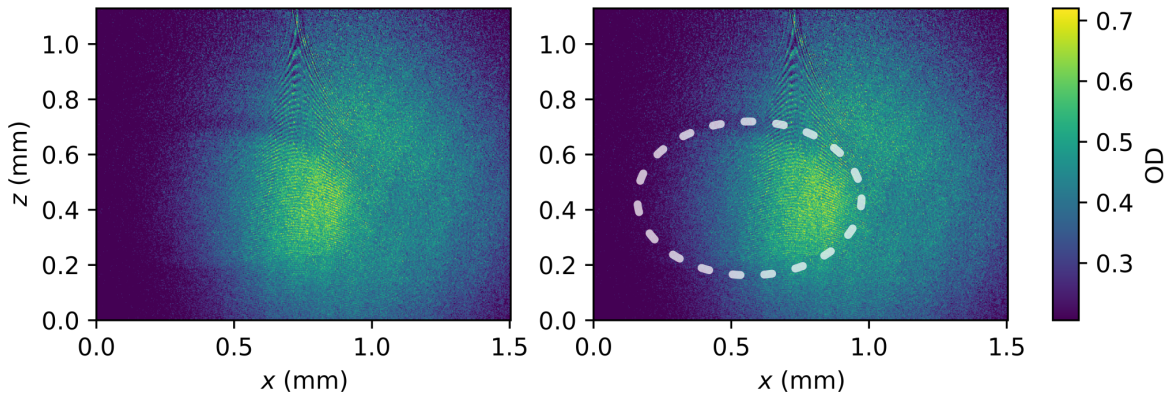


Figure 4.5: Rings of resonance from single-frequency red MOT light on the residual blue MOT atoms with dashed ring outlining the ring for clarity (right image). After turning off the blue MOT light and lowering the magnetic field gradient to the red MOT field gradient, some atoms are still present. The red MOT light is pulsed in single-frequency mode and causes a dark ring of absorption corresponding with the atoms in the resonant velocity class.

of atoms. These atoms will absorb the pulsed red light and show up as a dark ring in the optical depth image. Ideally, this ring's center will be located at the magnetic field zero, or the center of the trap. In Fig. 4.5, we see an example of when there were stray fields that had not been cancelled by the shim coils present, causing the ring's center to be displaced from the center of the trap. To determine optimal parameters for the red MOT, we scanned the frequency of the red MOT laser until we saw a ring. Then, if the ring was relatively large, this meant that the laser frequency was detuned from resonance. If the laser was red-detuned, as we move the frequency closer to resonance, the ring gets smaller, and on the other side of the resonance, the ring expands again. We gradually walked the detuning closer to resonance, while adjusting the shim fields to keep the center of the ring as close to the center of the trap as possible. The images in Fig. 4.5 are from just before we achieved the red MOT for the first time, and a diffuse cluster of atoms can be seen close to the right side of the ring.

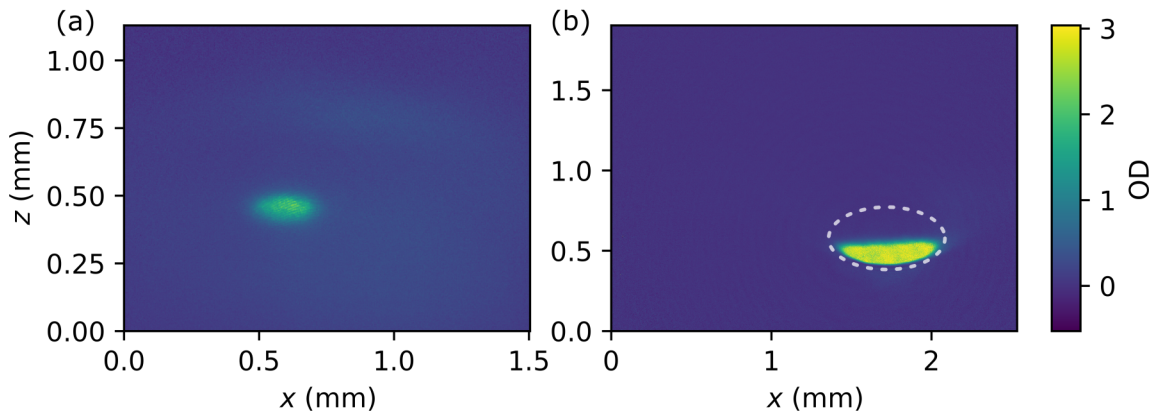


Figure 4.6: Red MOT absorption images *in situ*. (a) The first red MOT we achieved on this apparatus. (b) The red MOT at a later date, with the center frequency of the modulation of the red laser detuned from resonance by around 3 MHz. Here, we have an approximate OD of 3, and we trap around  $2 \times 10^7$  atoms. The atoms sag to the bottom of the resonant ring (dashed ellipse) because of the force of gravity.

We achieve the red MOT by following the experimental sequence described earlier in this section. Figure 4.6 shows the first red MOT produced on this apparatus and another later image of the red MOT after optimization, but detuned from resonance by about 3 MHz. The atoms in the red MOT sag in the center of the atomic cloud because the force due to gravity is no longer negligible compared to the MOT force, as described in Ch. 1. The currents in the shim coils to produce optimal shim fields vary sometimes, but tend to stay in the range of 0 - 0.5 A. In the red MOT we typically trap around  $3 \times 10^7$  atoms and achieve temperatures around  $5 \mu\text{K}$ .

## 4.3 Dipole Trap

### 4.3.1 Alignment

After trapping atoms in the red MOT, we transfer them to an optical dipole trap at 1064 nm. As described in Ch. 2, we chose lenses for the optical setup so that the beam waist at the center of the vacuum chamber would be approximately  $30 \mu\text{m}$ . To align the dipole trap, we first took an image of the red MOT to determine the position of the atoms in the camera's field of view in pixels. We then aligned the dipole trap beam at low power onto the camera at the same pixel position using steering mirrors. The lens just before the chamber was placed on a translation stage so that the position of the focus of the dipole trap beam could be finely adjusted. We took several experimental shots while varying the shim field values after the red MOT stage until we see something like what is shown in Fig. 4.7(a).

Here, we can see that the dipole trap is catching some atoms, but the position of the

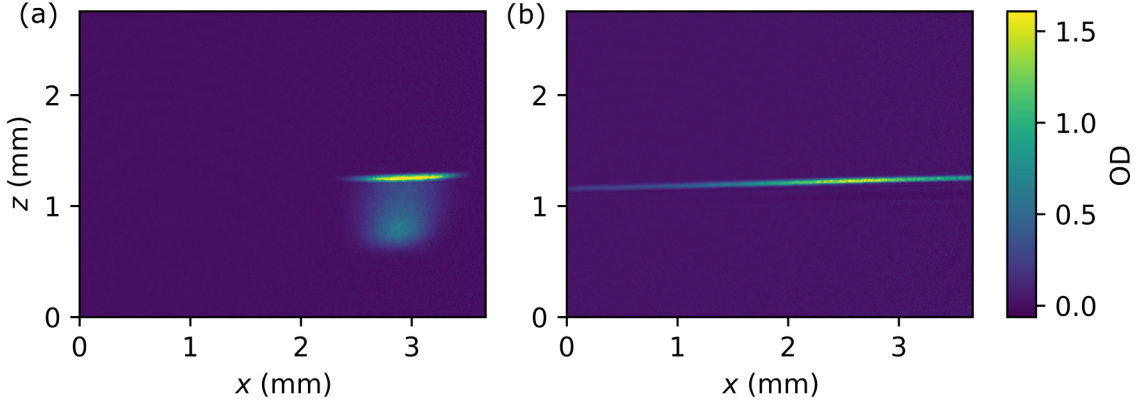


Figure 4.7: Absorption images of the dipole trap of  $^{88}\text{Sr}$  *in situ*. (a) First sign of a dipole trap. Some atoms are caught by the trap, but the position of the focus of the trap is displaced from the position of the red MOT, so atoms fall out of the bottom of the trap. (b) Properly aligned dipole trap. Atoms are attracted to the points in the trap with highest intensity of 1064 nm light, so the position of the atoms coincides with the propagation of the dipole trap beam.

focus of the trap is not aligned with where the red MOT forms, so some atoms are falling out of the trap. After adjusting the focus of the beam using the translation stage, we realized a proper dipole trap, shown in Fig. 4.7(b). The atoms are attracted to the positions with highest light intensity, so they collect in the center of the dipole trap beam [48].

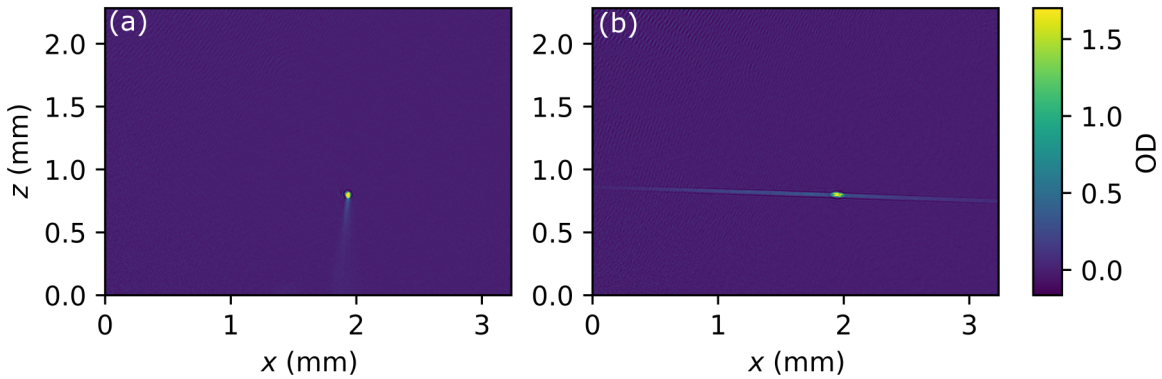


Figure 4.8: Absorption images of the dipole trap in the  $\hat{y}$  direction and the cross dipole trap. (a) Image of the  $\hat{y}$  dipole trap *in situ*. The atoms appear as a dot because the dipole trap beam propagates into the plane of the page. (b) Image of the cross dipole trap *in situ*. Atomic sample is localized at the intersection of the two 1D dipole traps.

### 4.3.2 Cross Dipole Trap

To align the dipole trap along the  $\hat{y}$  axis, we followed the same procedure to that of the first dipole trap. Figure 4.8 shows absorption images of the atoms *in situ* with just the  $\hat{y}$  axis dipole trap turned on (a) and the cross dipole trap (both  $\hat{x}$  and  $\hat{y}$ ) on. Once the second dipole trap was aligned, we iteratively walked its position and optimal shim field values to match those of the first dipole trap. In the cross dipole trap, we see confinement of the atoms in the position where the two dipole traps intersect.

In the future, measurements of the temperature of the atomic sample and the trap depth can be done, as well as evaporative cooling to a degenerate gas using this setup. Now that we have acquired the new M2 laser that will produce the magic wavelength 813 nm light for the clock transition of strontium, this dipole trap setup can also be switched to that wavelength with some minor realignment. The progress on this main apparatus positions future students to be able to complete the box trap experiments [27,28] mentioned in Chapter 1, once the repulsive blue detuned dipole trap has also been set up. In the following chapters, we will switch gears and discuss the much more compact grating magneto-optical trap apparatus.

## Chapter 5: Strontium Grating Magneto-Optical Trap

As presented in Chapter 1, there has been increased interest in designing compact cold atom systems with the hopes of creating portable and field-deployable quantum devices. At the National Institute of Standards and Technology, NIST, the Portable Cold Atom Vacuum Standard (pCAVS) group has already made progress in compact systems with alkali atoms [58, 127–130]. In this chapter, I am including our realization of the first grating magneto-optical trap of an alkaline-earth element, originally published in *Review of Scientific Instruments* **91**, 103202 (2020) [131]. This work was a collaboration between me, Peter Elgee, and Gretchen Campbell, along with Daniel Barker, Stephen Eckel, and Nikolai Klimov in the Sensor Science Division at NIST. Peter and I contributed equally to the experimental setup, taking and analyzing the data, and writing the original manuscript, with guidance from Dan, Gretchen, and Steve. Nikolai designed the nanofabricated diffraction grating used in the experiment. All authors contributed to editing the manuscript and provided insight throughout the process. In the last section of this chapter, I will report on work done since this publication on trapping the fermionic isotope of strontium in the broad line grating MOT.

## 5.1 Publication: Confinement of an alkaline-earth element in a grating magneto optical trap

### 5.1.1 Abstract

We demonstrate a compact magneto-optical trap (MOT) of alkaline-earth atoms using a nanofabricated diffraction grating chip. A single input laser beam, resonant with the broad  $^1S_0 \rightarrow ^1P_1$  transition of strontium, forms the MOT in combination with three diffracted beams from the grating chip and a magnetic field produced by permanent magnets. A differential pumping tube limits the effect of the heated, effusive source on the background pressure in the trapping region. The system has a total volume of around 2.4 L. With our setup, we have trapped up to  $5 \times 10^6$   $^{88}\text{Sr}$  atoms, at a temperature of approximately 6 mK, and with a trap lifetime of approximately 1 s. Our results will aid the effort to miniaturize quantum technologies based on alkaline-earth atoms.

### 5.1.2 Introduction

Laser-cooled alkaline-earth atoms have applications in a wide range of quantum devices, including atomic clocks [12,60,61], gravimeters [132], and spaceborne gravitational wave detectors [62, 63]. The transition from a laboratory to field-based applications will require a drastic reduction in the size and complexity of laser-cooling systems. For example, proposals to detect gravitational waves using alkaline-earth atoms require atom interferometers capable of being installed in satellites [62]. Compact versions of these laser-cooled systems are also necessary in order make the unprecedented accuracy of

alkaline-earth atomic clocks widely accessible [133].

Laser-cooling experiments typically use a magneto-optical trap (MOT) to capture, cool, and confine the atoms. Conventional MOTs use three orthogonal pairs of well-balanced, counterpropagating laser beams to confine atoms at the center of a quadrupole magnetic field. As such, MOTs require large vacuum chambers with optical access along all axes, and have many degrees of freedom in alignment and polarization. Compound optics can generate all necessary beams from a single input beam, reducing the complexity of the optical setup. For example, pyramidal retro-reflectors maintain the beam geometry of conventional MOTs [134]. However, the MOT forms inside the retro-reflecting optic, limiting optical access [135, 136]. Tetrahedral reflectors form the MOT above the optic, maintaining optical access but breaking the geometry of a conventional trap by using only four beams [137]. Tetrahedral MOTs can also be planarized by using diffraction gratings [138–140]. Thus far, only experiments with alkali atoms have been successfully miniaturized using such grating MOTs [58, 139, 140]. Here, we demonstrate a compact, grating MOT system for alkaline-earth atoms.

Alkaline-earth atoms pose unique challenges to miniaturization. First, sources for alkaline-earth atoms must be heated to high temperatures (over 350 °C) to create sufficient flux of atoms to load a MOT. Outgassing from the hot source can increase the background pressure, decreasing the trap lifetime, and equilibrium atom number. Second, alkaline-earth atoms require large magnetic field gradients (on the order of 5 mT/cm), often created with large water cooled coils [141]. Third, with the high Doppler temperature of the broad  $^1S_0 \rightarrow ^1P_1$  transition, and lack of sub-Doppler cooling, strontium and other alkaline-earth systems usually operate a second, subsequent MOT on the narrow

$^1S_0 \rightarrow ^3P_1$  transition to achieve lower temperatures. The ideal compact system must have the capability to operate at the two different cooling wavelengths.

Our system, designed around a diffraction grating chip, mitigates the above issues associated with miniaturizing a MOT for alkaline-earth atoms (see Fig. 5.1). First, a 3 cm long differential pumping tube separates the vacuum chamber into two regions: the source chamber and the science chamber. The source chamber contains a vacuum pump and a low-outgassing dispenser [128] that vaporizes strontium atoms. The atoms then travel through the differential pumping tube before entering the science chamber. Second, we create the magnetic field gradient for the MOT using permanent magnets, which are less complex than typical, water-cooled coils. The magnetic field gradient extends into the differential pumping tube, forming an effective Zeeman slower when combined with the input laser beam. Lastly, the first order diffraction efficiency of the grating we use is optimal at a wavelength of 600 nm, a middle ground between the two laser-cooling wavelengths (461 nm and 689 nm) for strontium. Our compact alkaline-earth grating MOT system also maintains the optical access and achieves the atom number necessary for future quantum devices.

### 5.1.3 Apparatus

Our apparatus is shown in Fig. 5.1. The vacuum system is comprised of two chambers, separated by a 3 cm long, 3 mm diameter differential pumping tube with an  $N_2$  conductance of 0.11 L/s. The MOT is located in a science chamber with four CF275 [142] viewports, and pumped with a 75 L/s ion pump (not shown). The source

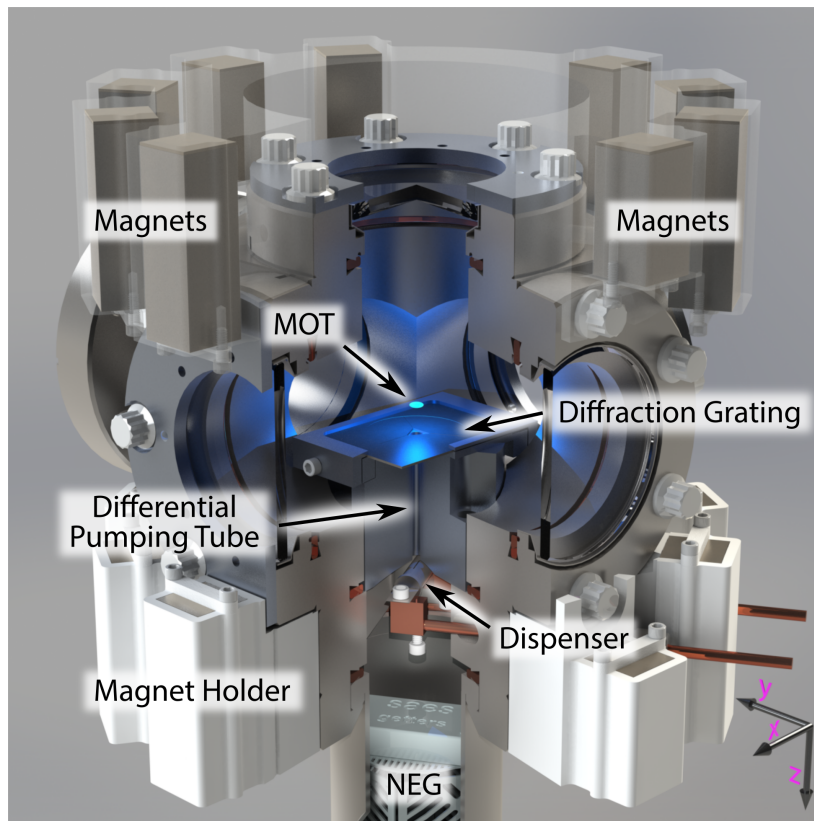


Figure 5.1: A cut-away model of the grating MOT system, with coordinates specified in the bottom right. The diffraction grating in the middle of the science chamber diffracts light to form the MOT beams. The input laser beam (not shown) propagates along the  $+\hat{z}$  direction. 3D-printed magnet holders position permanent magnets around the top and bottom of the chamber. The top magnet holder is translucent to show the configuration of the magnets in the holders. The polarity of the magnets is shown with red and blue coloring. The dispenser source sits below the differential pumping tube and is pumped by a non-evaporable getter (NEG) pump.

chamber is located below the differential pumping tube and is pumped with a 40 L/s non-evaporable getter (NEG) pump. Our source of Sr atoms is a 3D-printed titanium dispenser, described in Ref. [128]. We run a current between 12 A and 14 A through the dispenser, effusing strontium towards the differential pumping tube. Together, the source

and science chambers are approximately 2.4 L in volume, although this estimate does not include the ion pump or the magnet holders. In typical strontium experiments, the sources alone are often at least 2 L in volume. The base vacuum pressure of  $2 \times 10^{-7}$  Pa in the science chamber could be improved by replacing the large ion pump with a small hybrid NEG/ion pump, which would also reduce the size of the apparatus.

The grating chip is located above the differential pumping tube, and has a triangular hole through its center, allowing atoms to enter the science chamber. The grating chip was fabricated at the National Institute of Standards and Technology, and consists of three linear gratings arranged in a triangle. The parameters of the chip are the same as those in Ref. [58], except with a trench depth of 150(2) nm. This trench depth minimizes the 0<sup>th</sup> order diffraction at 600 nm, which is between the 461 nm and 689 nm cooling transition wavelengths for strontium. Each linear grating diffracts 32(1) % of the normally-incident 461 nm light into each of the  $\pm 1$  diffraction orders with an angle of 27.0(5)°. 4 % of the light is diffracted into each of the  $\pm 2$  orders, and 11 % is diffracted into the 0 order, with the remainder lost due to the aluminum coating [143]. The 0 order light does not disrupt the MOT because of the hole in the grating directly beneath it. The diffraction angle is a trade-off between confinement of the 461 nm MOT and overlap with the second stage 689 nm MOT beams. For normally incident, circularly polarized light, the stokes parameters of the grating chip at 461 nm are  $Q = -0.23(1)$ ,  $U = -0.13(1)$ ,  $V = 0.96(1)$ , where  $Q = 1$  ( $Q = -1$ ) corresponds to  $s$  ( $p$ ) polarization defined relative to the plane of reflection for each linear grating.

Two sets of grade N52 NdFeB magnets, arranged roughly in a dodecagon, create the magnetic field for the MOT. Within each set, the poles of the magnets are aligned.

The magnets are housed in 3D-printed magnet holders made of polylactic acid (PLA) that are designed to produce a compact setup with high magnetic field gradients, as shown in Fig 5.1. Due to the geometric constraints of the vacuum chamber, the configuration of magnets is asymmetric, and the principal axes are rotated from those Fig 5.1. We achieve maximum gradients of  $\{3.5 \text{ mT/cm}, 2.7 \text{ mT/cm}, 6.2 \text{ mT/cm}\}$  along the  $\{\hat{x}', \hat{y}', \hat{z}\}$  axes, respectively, where  $\hat{x}'$  and  $\hat{y}'$  are rotated by  $-\pi/6$  from  $\hat{x}$  and  $\hat{y}$ . By removing magnets from the holders, we can lower the gradient to  $\{1.9 \text{ mT/cm}, 1.9 \text{ mT/cm}, 3.8 \text{ mT/cm}\}$  along the  $\{\hat{x}', \hat{y}', \hat{z}\}$  axes, respectively. The field gradient extends to  $z \approx 50 \text{ mm}$ , where  $z = 0$  corresponds to the  $\mathbf{B} = 0$  and  $z \approx 40 \text{ mm}$  corresponds to the position of the source.

A single laser beam, red-detuned from the  $^1S_0 \rightarrow ^1P_1$  transition at 461 nm, enters through the top viewport along the  $+\hat{z}$  axis and is normally incident upon the diffraction grating chip. The input MOT beam has a  $1/e^2$  radius of 12 mm and a maximum power of 92 mW. For the  $^1S_0 \rightarrow ^1P_1$  transition with natural linewidth  $\Gamma/2\pi = 30.5 \text{ MHz}$ ,  $I_{\text{sat}} = 40.3 \text{ mW/cm}^2$ , giving a maximum peak  $I/I_{\text{sat}} \approx 1$ . Intensities  $I/I_{\text{sat}}$  reported herein always refer to the peak intensity of the input beam. The central portion of the beam continues through the hole in the diffraction grating and through the differential pumping tube. This beam, combined with the magnetic field gradient, allows for a small amount of initial slowing of the atoms, similar to a Zeeman slower. Atoms can be lost from the MOT because the excited  $^1P_1$  state decays at a rate of  $610 \text{ s}^{-1}$  to the  $^1D_2$  state, which in turn decays to the  $^3P$  manifold. To mitigate the atom loss, two repump lasers, with wavelengths 679 nm and 707 nm, address the  $^3P_0 \rightarrow ^3S_1$  and  $^3P_2 \rightarrow ^3S_1$  transitions, respectively. More information on the repump scheme can be found in Ref. [144]. The repump beams are combined together on a 50/50 beam splitter, and then combined with

the input MOT beam using a polarizing beam splitter.

We use absorption and fluorescence imaging along  $\hat{x}$  to characterize the MOT. Absorption images are taken after the MOT atom number equilibrates using a probe beam resonant with the  $^1S_0 \rightarrow ^1P_1$  transition with  $I/I_{\text{sat}} \approx 0.01$ . We use the atom number from the absorption images to calibrate the atom number extracted from fluorescence images taken during loading. The Labscript suite software [84] controls the experiment and data collection. More detailed information on the laser systems can be found in Ref. [46].

#### 5.1.4 Results

We measure atom number, loading rate, lifetime, and temperature to characterize the MOT. During each experimental shot we take a sequence of fluorescence images while the MOT loads and construct a loading curve. Fig. 5.2 shows typical loading curves at an axial magnetic field gradient of 6.2 mT/cm. For a MOT with no light assisted collisions, the loading rate  $R$ , MOT lifetime  $\tau$ , and equilibrium atom number  $N_0 = R\tau$ , are extracted by fitting each loading curve to the single exponential

$$N(t) = R\tau(1 - e^{-t/\tau}). \quad (5.1)$$

An example fit is shown with a solid black curve in Fig. 5.2. The quality of the fit to Eq. (5.1) indicates light assisted collisions and secondary scattering are negligible. At the higher gradient of 6.2 mT/cm, we observe typical loading rates of  $4 \times 10^6 \text{ s}^{-1}$  and a vacuum-limited lifetime of 1 s. We observe a similar loading curve at the lower gradient of 3.8 mT/cm.

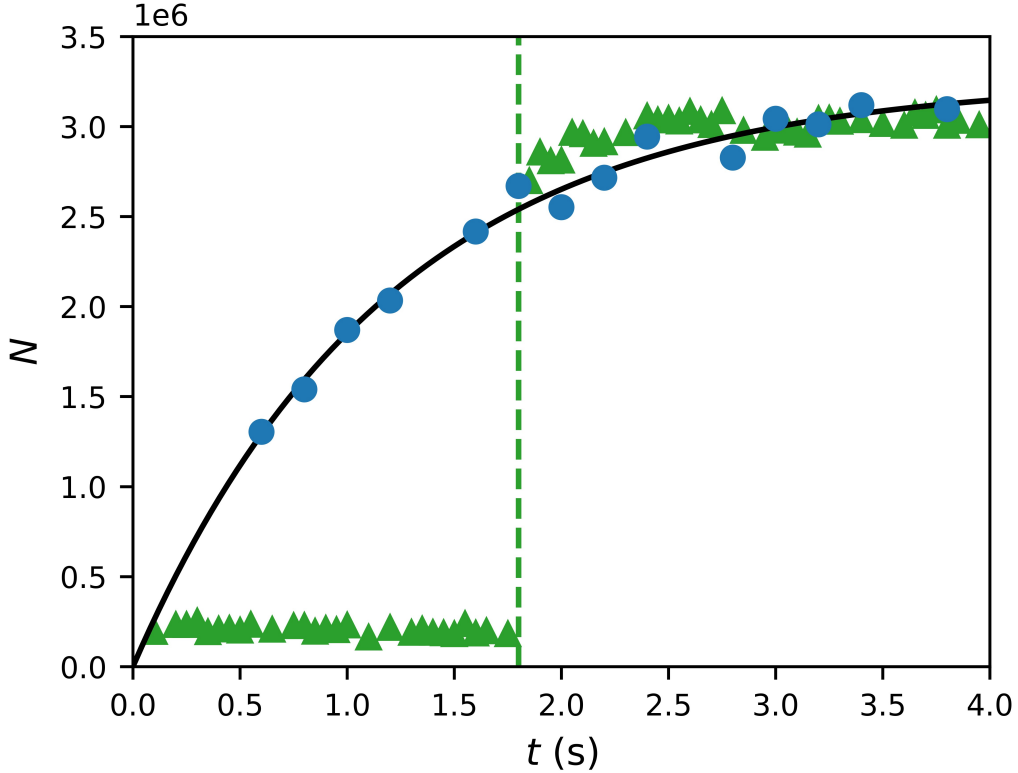


Figure 5.2: MOT loading curves with a source current of 13 A,  $I/I_{\text{sat}} = 1$ , axial magnetic field gradient of 6.2 mT/cm, and detuning  $\Delta/\Gamma = -1$ . The blue dots show the MOT atom number  $N$  as a function of time  $t$ . The black curve is a fit to Eq. 5.1. The green triangles show the MOT loading without repump lasers, and subsequent recapture from the metastable reservoir. The dashed line indicates when the repump lasers were turned on.

Fig. 5.3 and Fig. 5.4 show the MOT parameters as a function of detuning from resonance and intensity, respectively. We find the maximum atom number of approximately  $4 \times 10^6$  at a source current of 13 A and  $\Delta/\Gamma \approx -1$ , a typical detuning for a conventional 6-beam Sr MOT [16, 145, 146]. As shown in Fig. 5.4(a), the atom number continues to increase with  $I/I_{\text{sat}}$ , even at our maximum intensity, indicating that more laser power would be beneficial. The increase in  $N_0 = R\tau$  is only partially due to the increase in the loading rate  $R$ , shown in Fig. 5.4(b). Part of the atom number increase is due to an increase in the lifetime with intensity, shown in Fig. 5.4(c). The lifetime increase suggests

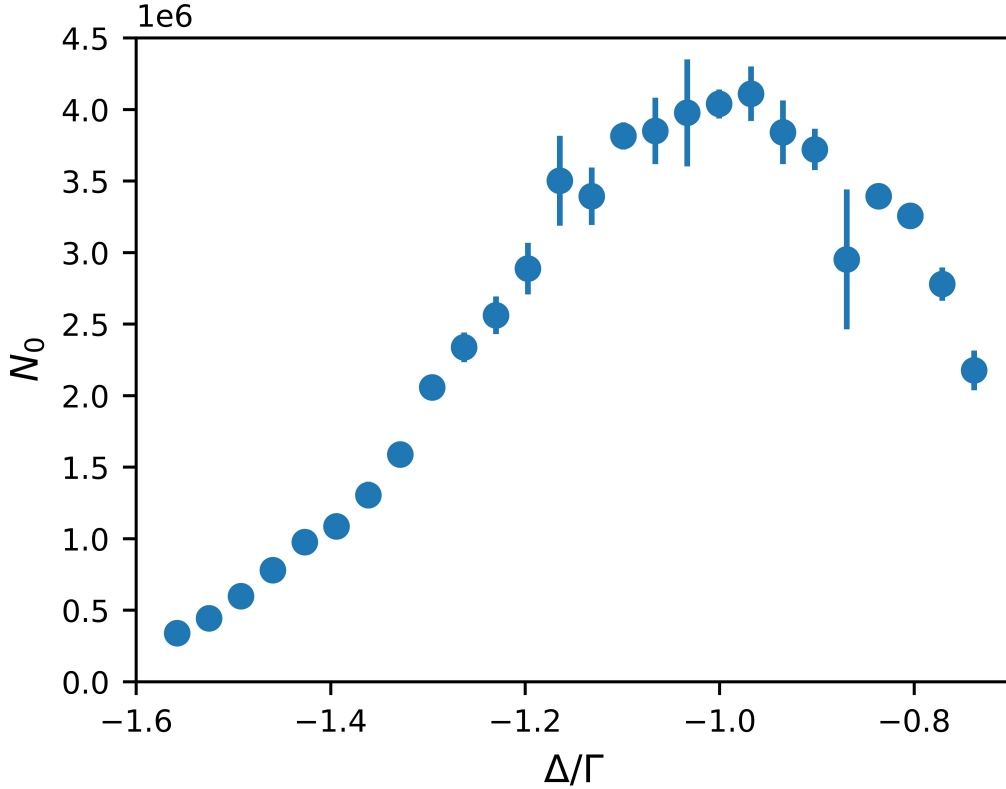


Figure 5.3: The equilibrium atom number  $N_0$  as a function of MOT beam detuning  $\Delta/\Gamma$ , with a source current of 13 A, axial magnetic field gradient of 6.2 mT/cm, and  $I/I_{\text{sat}} = 1$ . The optimal detuning is  $\Delta/\Gamma = -1$ . Most of the error bars are smaller than the data points, and represent the standard error about the mean.

that the trap depth is increasing with laser power, which in turn increases the escape velocity for a Sr atom that undergoes a background gas collision [147, 148]. However, the interplay between MOT temperature and tighter radial confinement with increasing intensity may also play a role.

We can also use the MOT to continuously load a magnetic trap, which consists of atoms that are trapped in the metastable  $^3P_2$  state. With strontium, the metastable magnetic trap is often used to increase the capture of rare isotopes and was key to the realization of quantum degeneracy [146, 149]. By operating the MOT without repump light, atoms are shelved in the  $^3P_2$  state where they are trapped by the MOT magnetic

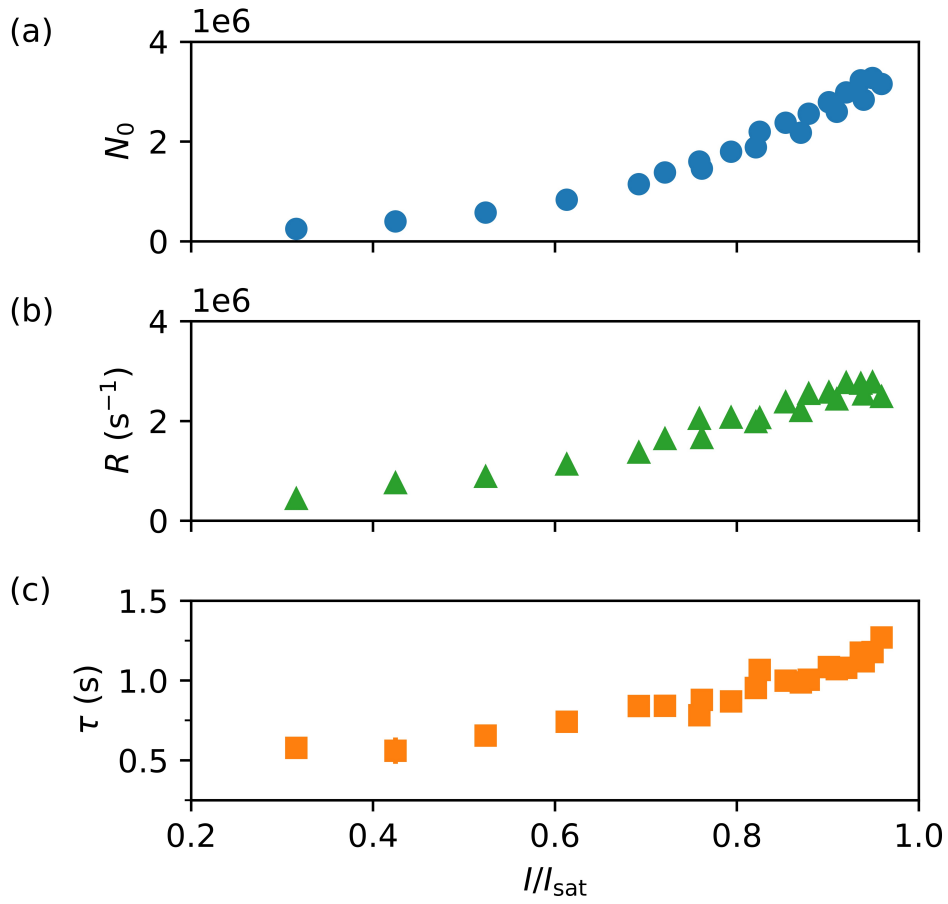


Figure 5.4: MOT loading parameters as a function of  $I/I_{\text{sat}}$ : (a) equilibrium atom number  $N_0$ , (b) loading rate  $R$ , and (c) lifetime ( $\tau$ ). Here, the source current is 13 A, the detuning  $\Delta/\Gamma = -1$ , and axial field gradient is 6.2 mT/cm. The error bars on the points are comparable to the marker size, and represent the standard error about the mean.

field. When the repump light is turned on after atoms have accumulated in the magnetic trap, we see a sharp increase in the MOT atom number as shown in Fig. 5.2. The recovery confirms that atoms are being caught and held in the magnetic trap, however we do not see a transient enhancement above the equilibrium atom number as demonstrated elsewhere [37]. Given our densities, and vacuum-limited atom number, we would not expect enhancement from magnetic trap loading. Adding a depumping laser could enhance the loading rate of the magnetic trap and increase the atom number [35].

We investigate the effect of the source current on the atom number, loading rate, and lifetime, shown in Fig. 5.5. The source current sets the temperature of the source, which in turn determines both the vapor pressure and the average velocity of atoms leaving the source. At our highest achievable source current of 14 A, limited by the ampacity of our electrical feedthroughs, we trap  $5 \times 10^6$  atoms, but have still not saturated the atom number. Based on the fit presented in Ref. [128], we estimate the source temperature at 13 A to be over 600 °C. When the source current is increased from 0 A to 13 A, the vacuum pressure in the science chamber increases by  $3 \times 10^{-8}$  Pa, suggesting that the differential pumping is sufficient. The increase in pressure is consistent with the small lifetime decrease shown in Fig. 5.5(c).

To determine the temperature of the MOT, we measure the width of the atomic cloud as it expands in time of flight, shown in Fig. 5.6. A Gaussian fit extracts the root-mean-square (rms) width,  $w$ , of the cloud in both the  $\hat{y}$  and  $\hat{z}$  directions. The extracted widths are binned by time of flight, and the error bars are calculated from the standard error about the mean. We fit the data to  $w(t)^2 = w_0(t)^2 + v_{rms}^2 t^2$ , where  $w_0$  is the initial rms width of the cloud,  $v_{rms} = \sqrt{k_B T / m}$  is the rms velocity,  $k_B$  is Boltzmann's constant,  $m$  is the

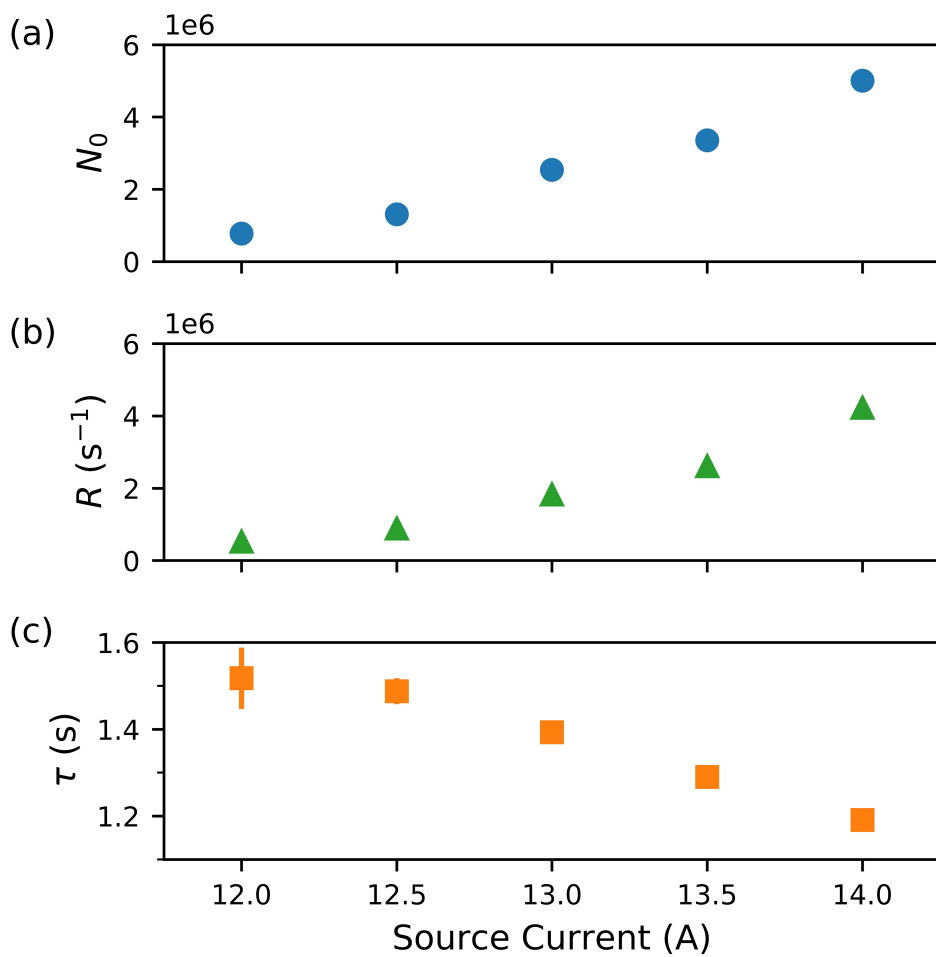


Figure 5.5: MOT loading parameters as a function of source current: (a) equilibrium atom number  $N_0$ , (b) loading rate  $R$ , and (c) lifetime ( $\tau$ ). Here,  $I/I_{\text{sat}} \approx 1$ ,  $\Delta/\Gamma = -1$ , and axial field gradient is 6.2 mT/cm. The error bars on most of the points are comparable to the marker size, and represent the standard error about the mean.

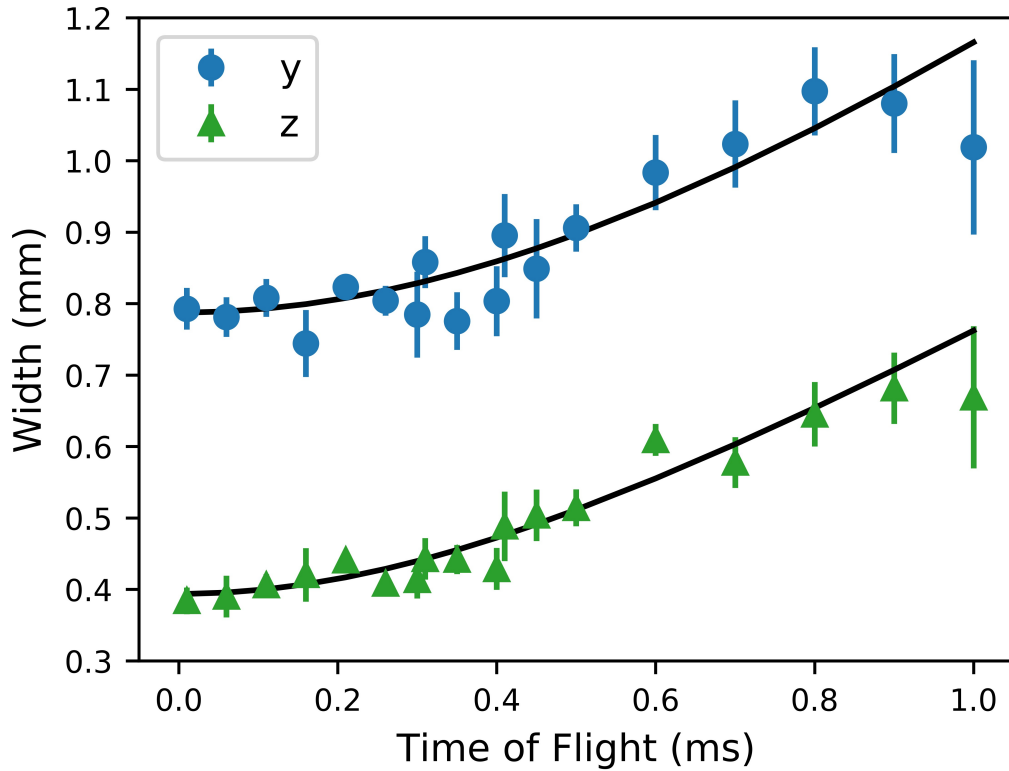


Figure 5.6: Temperature measurement of the atomic cloud. The rms width of the atomic cloud in the  $\hat{y}$  direction (blue circles) and in the  $\hat{z}$  direction (green triangles) are plotted against time of flight and fitted to the expansion function discussed in the text (black curves). The calculated temperatures based on the fits are 7.8(9) mK and 4.6(4) mK for  $\hat{y}$  and  $\hat{z}$ , respectively, where the errors in parentheses are one standard deviation. This data was taken with a source current of 13 A,  $I/I_{\text{sat}} = 1$ , axial magnetic field gradient of 6.2 mT/cm, and detuning  $\Delta/\Gamma = -1$ . The error bars represent the standard error about the mean.

atomic mass, and  $T$  is the temperature of the atomic cloud. The temperature is 7.8(9) mK and 4.6(4) mK for  $\hat{y}$  and  $\hat{z}$ , respectively, where the errors in parentheses are one standard deviation, which is consistent with a conventional six-beam MOT [145]. The temperature is not equal in the two dimensions because the diffusion coefficient and velocity damping constant are different in the axial and radial directions in a grating MOT. For our MOT, the ratio of the temperatures along  $\hat{y}$  and  $\hat{z}$  is 1.7(2), consistent with the ratio of 1.9 from the theory in Ref. [150].

While the discussion has focused on trapping  $^{88}\text{Sr}$ , strontium has a number of stable isotopes. The isotope abundances for strontium are 82.58 %, 7.00 %, 9.86 %, and 0.56 % for  $^{88}\text{Sr}$ ,  $^{87}\text{Sr}$ ,  $^{86}\text{Sr}$ , and  $^{84}\text{Sr}$ , respectively. Our setup can also trap around  $7 \times 10^5$  atoms of  $^{86}\text{Sr}$  at a source current of 13 A, consistent with the abundances above. Likewise, we would also expect to trap around  $5 \times 10^5$  atoms of  $^{87}\text{Sr}$ , but were unable to realize a MOT of  $^{87}\text{Sr}$ . The hyperfine structure of  $^{87}\text{Sr}$  poses at least two complications. First, we might not have sufficient repump power to adequately address all necessary hyperfine transitions [24]. Second, the hyperfine structure combined with the non-trivial geometry and polarizations of the grating MOT may significantly weaken the already limited transverse confining forces [47, 139]. The theoretical details of the latter are beyond the scope of this work and will be presented in a future publication.

### 5.1.5 Discussion

We have realized a grating MOT of alkaline-earth atoms in a compact 2.4 L apparatus. Our permanent magnet design supplies the necessary field gradients for the MOT and allows for a degree of tunability, while the differential pumping tube limits outgassing from the hot source. The MOT traps up to  $5 \times 10^6$  atoms of  $^{88}\text{Sr}$  at a loading rate of  $4 \times 10^6 \text{ s}^{-1}$ , with a lifetime of approximately 1 s. This performance is comparable to vapor loaded, six-beam strontium MOTs [145, 151]. We also observe MOTs of  $^{86}\text{Sr}$  with  $7 \times 10^5$  atoms, consistent with the relative isotopic abundance.

In the future, upgrades to our apparatus could be made to improve the performance of the MOT and decrease the size of the system. We could improve the quality of the

vacuum and reduce the size of the apparatus by replacing the ion pump with a hybrid NEG/ion pump. Improving the quality of the vacuum would increase atom number and lifetime, potentially allowing us to observe a MOT of  $^{84}\text{Sr}$ . The system could be further miniaturized by using a fiber-coupled and photonically integrated chip to expand the MOT beam to the appropriate size without additional optics [152, 153].

With additional upgrades to our apparatus, we would be able to transfer atoms to a second stage MOT operating on the narrow  $^1\text{S}_0 \rightarrow ^3\text{P}_1$  transition at 689 nm. The grating has good diffraction efficiency at both the 461 nm and 689 nm cooling wavelengths. In addition, 43% of the capture volume created by the 689 nm diffracted beams overlaps with the 461 nm capture volume, facilitating transfer between the MOTs. As discussed in Ref. [139] and Ref. [154], the diffracted beams of a grating MOT have a complicated polarization projection onto the  $\hat{z}$  axis. The mixed polarization projection of the diffracted beams reduces the confining force, which might limit the second stage MOT because the force due to gravity is no longer negligible. The second stage MOT also requires a low magnetic field gradient to operate, which we could achieve by incorporating electromagnets with our permanent magnet assembly. Due to its low field gradient, the second stage MOT is highly sensitive to stray magnetic fields, thus we would also need to incorporate shim coils to ensure proper positioning. The electromagnets and shim coils would also allow us to null the magnetic field to allow operation of optical clocks. We plan to make these upgrades to the apparatus and attempt second stage cooling in future experiments.

The implementation of field-deployable quantum devices relies on compact systems. Alkaline-earth-based quantum sensors have been proposed as platforms for atom interferometers and atomic clocks. Compact interferometers could be used for inertial navigation [155],

and gravitational wave detection in space [62]. Deployable networks of optical clocks will be important for improved time and frequency metrology [133], and tests of fundamental physics [156]. Our results show that alkaline-earth grating MOTs are a promising step towards the development of compact optical clocks and other quantum devices.

## 5.2 Broad Line Grating MOT in $^{87}\text{Sr}$

As stated in the previous section, the possibility of trapping  $^{87}\text{Sr}$  was somewhat doubtful because of its hyperfine structure. We did not initially observe a  $^{87}\text{Sr}$  broad line MOT, even though we did observe a MOT of  $^{86}\text{Sr}$ , which has a similar isotopic abundance. For the fermionic isotope, we have nuclear spin  $I = 9/2$ , and so the excited state of the  $^1\text{S}_0 \rightarrow ^1\text{P}_1$  transition has  $m_F = -1, 0, 1$  hyperfine splittings. For an  $F \rightarrow F' = F + 1$  transition, the condition for stable trapping in a MOT is [47]:

$$\frac{F}{F+1} < \frac{\mu_{F'}}{\mu_F} < \frac{F}{F-1} \quad (5.2)$$

Thus, if the magnetic moments of the ground and excited state are highly mismatched, there should not be stable MOT operation. Condition 5.2 is violated for both the broad line  $^1\text{S}_0 \rightarrow ^1\text{P}_1$  and the intercombination line  $^1\text{S}_0 \rightarrow ^3\text{P}_1$  in strontium, but this issue has been mitigated for intercombination line six-beam strontium MOTs using sawtooth wave adiabatic passage [157, 158] or an additional stirring laser [21, 24, 47] to randomize the ground state  $m_F$  levels, as mentioned in Ch. 1. Because the natural linewidth of the broad blue MOT transition is so large (30.2 MHz), off-resonant excitations of the  $F \rightarrow F' = F$  and  $F \rightarrow F' = F - 1$  transitions are sufficient to stabilize the broad line  $^{87}\text{Sr}$  six-beam

MOT. In a grating MOT, the axial spin polarization due to the tetrahedral geometry has the potential to cause issues for trapping of fermionic alkaline-earth atoms.

After performing simulations of the axial force profiles in a  $^{87}\text{Sr}$  blue grating MOT using PyLCP [64], we determined that the center position of the fermionic grating MOT would be slightly closer (on the order of a couple mm) to the magnetic field zero as compared to that of the  $^{88}\text{Sr}$  grating MOT. In Fig. 5.7, we show experimental confirmation of the simulation results. We took repeated fluorescence images of both the  $^{88}\text{Sr}$  and  $^{87}\text{Sr}$  MOTs and averaged the images to find the approximate center. The MOT center and point of zero force for the boson (fermion), are indicated by the dashed (dotted) lines in Fig. 5.7(a), (b), and (c).

We find optimal fluorescence counts at a beatnote frequency that is around 9 MHz detuned from where we find our optimal  $^{88}\text{Sr}$  grating MOT, which is consistent with typical isotope shift values [16, 52]. As is the case with our six-beam fermionic blue MOT setup, we must modulate the frequency of the repump laser at 707 nm to address as many hyperfine transitions as possible. For the grating MOT, we find optimal repump

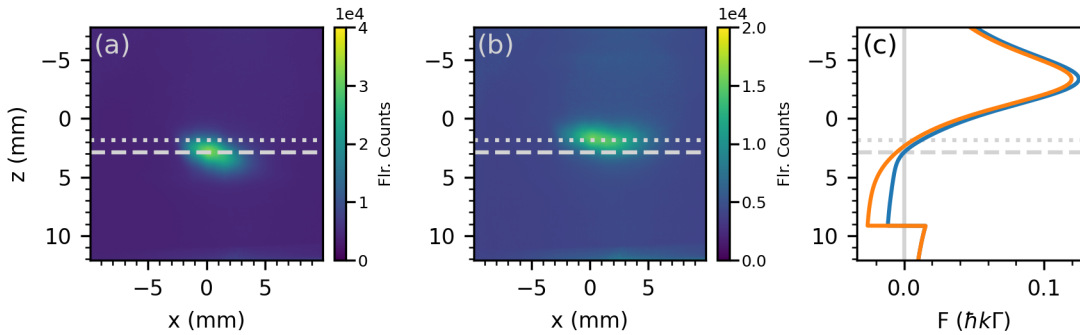


Figure 5.7: Comparison of the measured and calculated center shift of the  $^{88}\text{Sr}$  and  $^{87}\text{Sr}$  blue grating MOTs. (a) and (b) show average fluorescence images for  $^{88}\text{Sr}$  and  $^{87}\text{Sr}$ , respectively. (c) shows the axial force profile for  $^{88}\text{Sr}$  (blue) and  $^{87}\text{Sr}$  (orange). Dashed (dotted) lines show the point of zero force in each force profile for  $^{88}\text{Sr}$  ( $^{87}\text{Sr}$ ).

modulation frequencies at 658 MHz, 1209 MHz, 1502 MHz with respect to the main frequency at 423.91300 THz, and we operate the 679 nm repump laser at a frequency of 441.33250 THz. With these parameters, we achieve around 10,000 peak fluorescence counts in the  $^{87}\text{Sr}$  MOT. According to the natural abundance ratios listed in Chapter 1, this is still a factor of 2 less counts than we would expect given the number of fluorescence counts we get for our  $^{88}\text{Sr}$  blue grating MOT.

In the following chapter, we will discuss the intricacies of the narrow-line MOT in a tetrahedral trap geometry. We report the realization of a narrow-line grating MOT of  $^{88}\text{Sr}$  using sawtooth wave adiabatic passage, and discuss the possibility of also trapping  $^{87}\text{Sr}$  in a narrow-line grating MOT.

## Chapter 6: Narrow Line Sr Grating MOT

### 6.1 Sawtooth Wave Adiabatic Passage (SWAP) Cooling

As described in Chapter 1, the earliest mechanism of laser cooling, Doppler cooling, relies on the preferential absorption of counter-propagating laser beams, followed by spontaneous emission. Doppler cooling is limited by the recoil temperature  $T_R = \hbar^2 k^2 / mk_B$ , derived from the energy from emitting one photon, with  $\omega_R < \Gamma$ , where  $\omega_R$  is the recoil frequency and  $\Gamma$  is the natural linewidth of the atomic transition. For narrow linewidth transitions, the cooling timescale is long, as it scales inversely with  $\Gamma$ , and the scattering process is not as efficient. As such, many methods of laser cooling have been explored which try to reduce the reliance on spontaneous emission, such as Sisyphus cooling, Raman sideband cooling, cavity cooling techniques, and cooling using the bichromatic force [159–163]. With sawtooth wave adiabatic passage, or SWAP cooling, particles are coherently driven between the ground and excited states of a narrow-linewidth optical transition by counter-propagating frequency-swept laser beams, allowing stimulated forces to enhance laser cooling. By coherently driving the transition many times, large amounts of energy can be removed from the system with each spontaneous emission, and significant forces can be generated to achieve sufficiently low temperatures while maintaining a higher capture velocity [164, 165].

To illustrate the general concept of SWAP, we consider two counter-propagating linearly polarized laser beams with frequency  $\omega_L(t)$  hitting an atom, shown in Fig. 6.1(a). If the frequencies of both laser beams are swept in a sawtooth wave pattern (Fig 6.1(b)), due to the Doppler shift from the atom's motion, the counter-propagating laser beam will become resonant with the atom first and adiabatically transfer the atom from the ground state  $|g\rangle$  to the excited state  $|e\rangle$ . The atom will then absorb a photon and receive a momentum kick of  $-\hbar k$ . As the frequency sweep continues, the co-propagating beam later becomes resonant with the atom and stimulates emission back to the ground state, and the atom receives another momentum kick in the same direction of  $-\hbar k$ . The result of this mechanism is that the atom has now received two photon kicks via stimulated absorption followed by stimulated emission and has also returned back to its initial state.

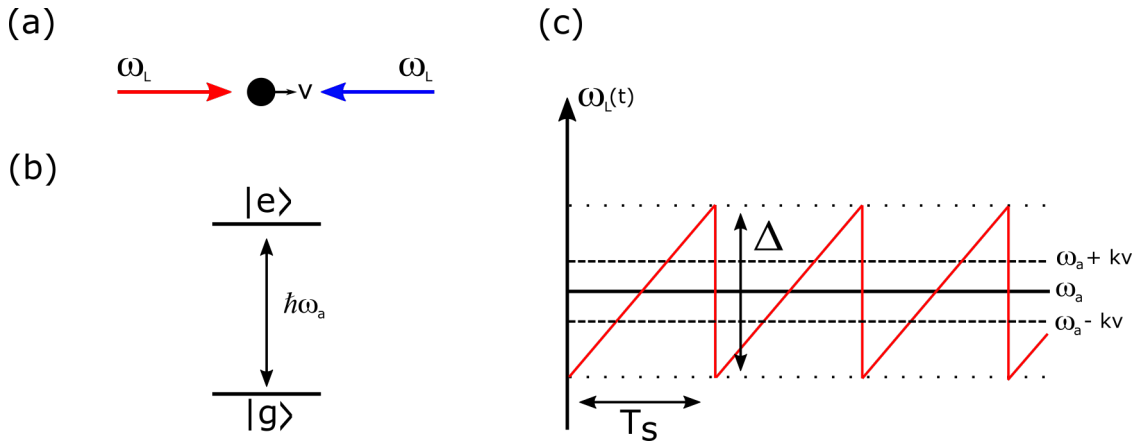


Figure 6.1: Visualization of the SWAP cooling mechanism. (a) Two counter-propagating linearly polarized laser beams, both with frequency  $\omega_L(t)$ , interact with an atom with velocity  $v$ . (b) Level diagram showing ground and excited state of the two-level system, with transition frequency  $\omega_a$ . (c) Sawtooth waveform indicating the frequency  $\omega_L$  over time, with sweep time  $T_s$  and sweep range  $\Delta$  (bounded by dotted lines). Dashed lines indicate frequencies  $\omega_a + kv$  and  $\omega_a - kv$ , the resonant frequencies of the co-propagating and counter-propagating laser beams, respectively. Because of the Doppler shift, the counter-propagating beam becomes resonant with the atom first, exciting the atom from  $|g\rangle$  to  $|e\rangle$ . As the laser frequency sweeps, the co-propagating beam later becomes resonant, stimulating emission from  $|e\rangle$  to  $|g\rangle$ .

To achieve SWAP cooling, the sweep range  $\Delta$ , must be large enough for both beams to become resonant, or [165]:

$$\Delta > 4|kv|. \quad (6.1)$$

This ensures that the atom is in the ground state at the beginning of each sweep of the laser frequency. In addition, to minimize the probability of spontaneous emission while the atom is in the excited state, we also require that the time spent in the excited state  $\tau_e \ll 1/\Gamma$ . Finally, to ensure a great enough probability of an adiabatic transition at each resonance, we must have the following condition on the Rabi frequency  $\Omega$  and the sweep rate  $\alpha$  [165]:

$$\frac{\Omega^2}{\alpha} \geq 1. \quad (6.2)$$

## 6.2 SWAP in a MOT

As reported in the previous chapter, we have realized a broad-line grating MOT of both  $^{88}\text{Sr}$  and  $^{87}\text{Sr}$ . We achieve temperatures around 6 mK in the  $^{88}\text{Sr}$  blue grating MOT, and as with a conventional six-beam MOT, we must transfer the atoms to the narrow-line red MOT on the  $^1\text{S}_0 \rightarrow ^3\text{P}_1$  transition to achieve  $\mu\text{K}$  temperatures. Transfer to the narrow-line MOT in a grating configuration has recently been demonstrated in  $^{88}\text{Sr}$  [166]. In this chapter, we investigate SWAP as it can apply to a narrow-line grating MOT of strontium atoms. In conventional strontium setups, SWAP has been shown to increase the capture fraction and produce fast and efficient loading into the narrow-line

MOT for  $^{88}\text{Sr}$  and  $^{87}\text{Sr}$  [157, 158].

To consider SWAP in a conventional six-beam MOT, we take the 1D case: two counter-propagating and oppositely circularly polarized beams interacting with an atom moving with velocity  $\vec{v}$ , shown in Fig. 6.2. Again, the atom has a transition from  $|g\rangle$  to  $|e\rangle$  with resonant frequency  $\omega_a$ . With a uniform magnetic field with magnitude  $B$ , the excited state  $|e\rangle$  splits into three excited states,  $|-\rangle$ ,  $|e_0\rangle$ , and  $|+\rangle$ , with a Zeeman shift  $\delta \propto m_J B$  between  $|e_0\rangle$  and  $|-\rangle$  and  $|e_0\rangle$  and  $|+\rangle$ . In a normal experimental scheme for a strontium red MOT, we usually use a triangle wave to modulate the frequency of the 689 nm laser. With SWAP, both the  $\sigma^+$  and  $\sigma^-$  polarized beams have frequency  $\omega_L(t)$ , sweep time  $T_s$ , and sweep range  $\Delta$ . As the laser sweeps across frequencies, the  $\sigma^-$  polarized beam will become resonant with the atoms first, and this will excite some population,  $P_-$  of the

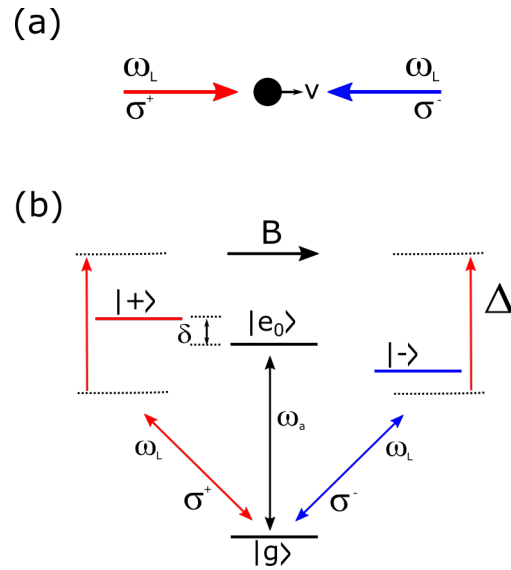


Figure 6.2: Visualization of the SWAP in a magneto-optical trap. (a) Two counter-propagating oppositely circularly polarized laser beams, both with frequency  $\omega_L(t)$ , interact with an atom with velocity  $v$ . (b) Level diagram showing ground and excited state of the two-level system, with transition frequency  $\omega_a$ . A uniform magnetic field causes Zeeman splitting  $\delta \propto m_J B$  of the excited state into  $|+\rangle$ ,  $|e_0\rangle$ , and  $|-\rangle$ . Sweep range  $\Delta$  is indicated by the dotted lines and red vertical arrows.

atoms to the  $|-\rangle$  state. If the sweep time  $T_s$  is small compared to the  $20 \mu\text{s}$  lifetime of the excited state  $^3\text{P}_1$ , then these atoms will still remain in the  $|-\rangle$  state when the laser sweeps over the resonant frequency of  $|+\rangle$ . This causes the population,  $P_+$ , of atoms excited to  $|+\rangle$  to be a bit smaller than  $P_-$ , and this gives an imbalance in the momentum exchanged between the atoms and the  $\sigma^-$  and  $\sigma^+$  laser beams. When the Zeeman shift  $\delta$  is 0 (close to the magnetic field zero of the quadrupole field), the atom is equally likely to interact with either laser beam. In this case,  $\delta$  is much smaller than the Doppler shift  $kv$ , and this is what provides the time-ordered absorption of the “correct” beam to receive a momentum kick even closer to the center of the trap, as is the case in SWAP cooling. If a downward sawtooth wave sweep is used (referred to as anti-SWAP later), the atom absorbs from the two laser beams in the wrong order, and we do not get a trap with confinement and cooling. The SWAP MOT mechanism is different from SWAP cooling in that it still relies heavily on spontaneous emission to reset the atom back to the ground state since the counter-propagating beams no longer address the same transition, whereas SWAP cooling relies on spontaneous emission only occasionally [157]. There has been a theoretical proposal to realize true SWAP cooling in a MOT involving two stimulated momentum kicks, but this involves rapidly switching the magnetic field direction and the polarizations of both beams in the middle of the sawtooth sweep [167].

### 6.3 Simulations of SWAP in a Grating MOT

Although SWAP has been shown to increase capture fraction in  $^{88}\text{Sr}$  and  $^{87}\text{Sr}$  in conventional MOT setups, there was uncertainty as to whether it would work with a

grating MOT, especially for  $^{87}\text{Sr}$ , due to the added complications with scrambled polarization in a grating setup and hyperfine structure with the fermionic isotope. As mentioned in Chapter 1, the diffracted beams in a grating MOT have  $\sigma^+$ ,  $\pi$ , and  $\sigma^-$  polarization components, and the “correct” circular polarization has the least intensity out of the three. Thus, with SWAP, it is possible that you would get the wrong time-ordered absorption since the probability of interacting with the laser beam that would give the atom a momentum kick away from the center of the trap is higher. This is not as much of an issue with triangle wave modulation because the wave is symmetric and the atoms receive both directions of frequency sweep.

Using the Python package PyLCP [64], we were able to simulate the performance of the red MOT in a grating apparatus using both triangle and sawtooth wave modulation. PyLCP calculates the force profile by solving the optical Bloch equations after defining the Hamiltonian for the system. The simulations in Fig. 6.3(a) and (b) were done using masked Gaussian laser beams and a standard quadrupole field. To average over the polarization lattice formed by the laser beams, we took 100 random phase samples of the laser beams. The force profiles were calculated assuming a sweep range  $\Delta$  of  $200\Gamma$ , where  $\Gamma$  is the natural linewidth of the intercombination line transition. We use an initial sweep detuning of  $-100\Gamma$  and a final sweep detuning of  $100\Gamma$ . We also did a simulation of the force in the  $\hat{z}$  direction with respect to a constant magnetic field in the  $\hat{z}$  direction. For this, we set the initial position and velocity vectors of the atoms as  $x_i = (0,0,0)$  and  $v_i = (0,0,0)$ . Then, we set a constant magnetic field  $B_z$  and take 200 samples over a range of  $-400$  to  $400 \mu_B B_z / \hbar \Gamma$ . In both simulations, we ensure that the sweep rate for the triangle wave and sawtooth wave are the same.

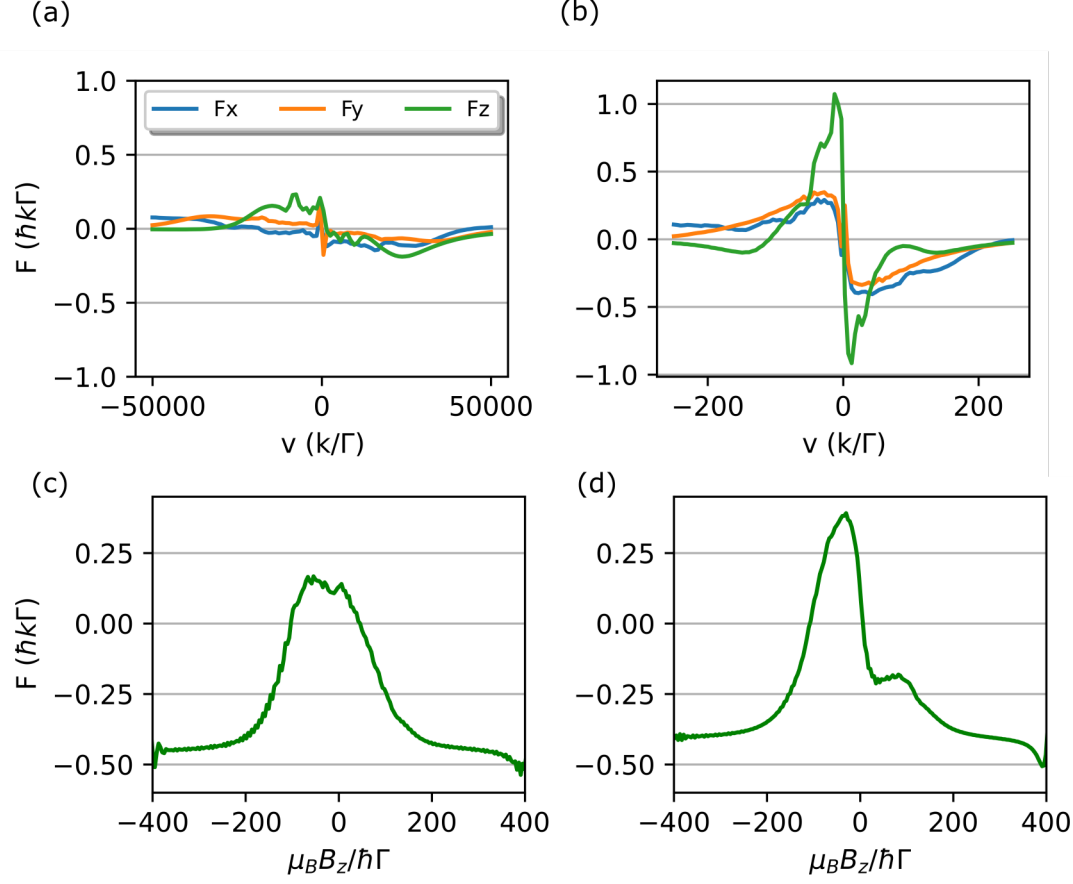


Figure 6.3: Simulations of force profiles vs. velocity and magnetic field for  $^{88}\text{Sr}$ . (a) Force vs. velocity with triangle wave modulation of the red MOT beam. (b) Force vs. velocity with sawtooth wave modulation of the red MOT beam. (c) Axial force vs. axial magnetic field with triangle wave modulation. (d) Axial force vs. axial magnetic field with sawtooth wave modulation. All the force profiles were calculated with the following parameters: sweep range  $\Delta = 200\Gamma$ , where  $\Gamma$  is the natural linewidth of the transition and the sweep is centered on resonance, saturation intensity  $s = 6030I_{sat}$ . The triangle wave simulation used a sweep period  $T_s = 5\tau$ , while the sawtooth wave simulation used  $T_s = 2.5\tau$ , where  $\tau$  is the lifetime of the excited state, to keep the sweep rate the same.

From these simulations, we can see that with the sawtooth wave, we achieve stimulated forces in the axial direction, as the peak force for  $F_z$  exceeds  $1/2 \hbar k \Gamma$ , and importantly, we see proper MOT confining forces along all three axes. Even with respect to the magnetic field, the peak force generated by sawtooth wave modulation is higher than that generated by triangle wave modulation at magnetic fields close to zero, which is consistent with

the idea that SWAP cooling plays a part close to the magnetic field zero. Both of these simulations indicate that SWAP can not only work in our grating MOT system, but might be advantageous over triangle wave modulation.

## 6.4 Changes to the Apparatus

The vacuum chamber remains roughly the same as was described in Ref. [131]. One issue we encountered with this apparatus, was the buildup of strontium on the top viewport. To fix this issue, we replaced this viewport with a heated viewport from Thermionics Northwest Inc. (Part No. VHW-150-G), shown in Fig. 6.5. This viewport supports temperatures up to 550 °C and is rated for ultra-high vacuum applications. We operate the viewport at around 300 °C. The viewing area has a 2.38 inch diameter and the window is mounted on a 4.5 inch outer diameter flange. We use a long nipple to attach the heated viewport to the vacuum chamber to allow space for the fan that accompanies the heated viewport and the magnetic field coils. Since Ref. [131], we fixed a minor vacuum leak in our apparatus, giving us a slight improvement in vacuum pressure and atom number in our blue MOT. We now achieve a base vacuum pressure of approximately  $1 \times 10^{-7}$  Pa and around  $4 \times 10^7$  atoms in the blue MOT of  $^{88}\text{Sr}$ .

The setup of the 679 nm and 707 nm repump beams is the same as that of the previous apparatus, described in Ch. 5; we combine both repump beams on a PBS and send them into the chamber via the side viewport, shown in Fig. 6.4 and Fig. 6.5. To incorporate the red laser beams needed to create the red MOT, we use the laser system described in Chapter 2. As shown in Fig. 6.4, we combine the red and blue beams using

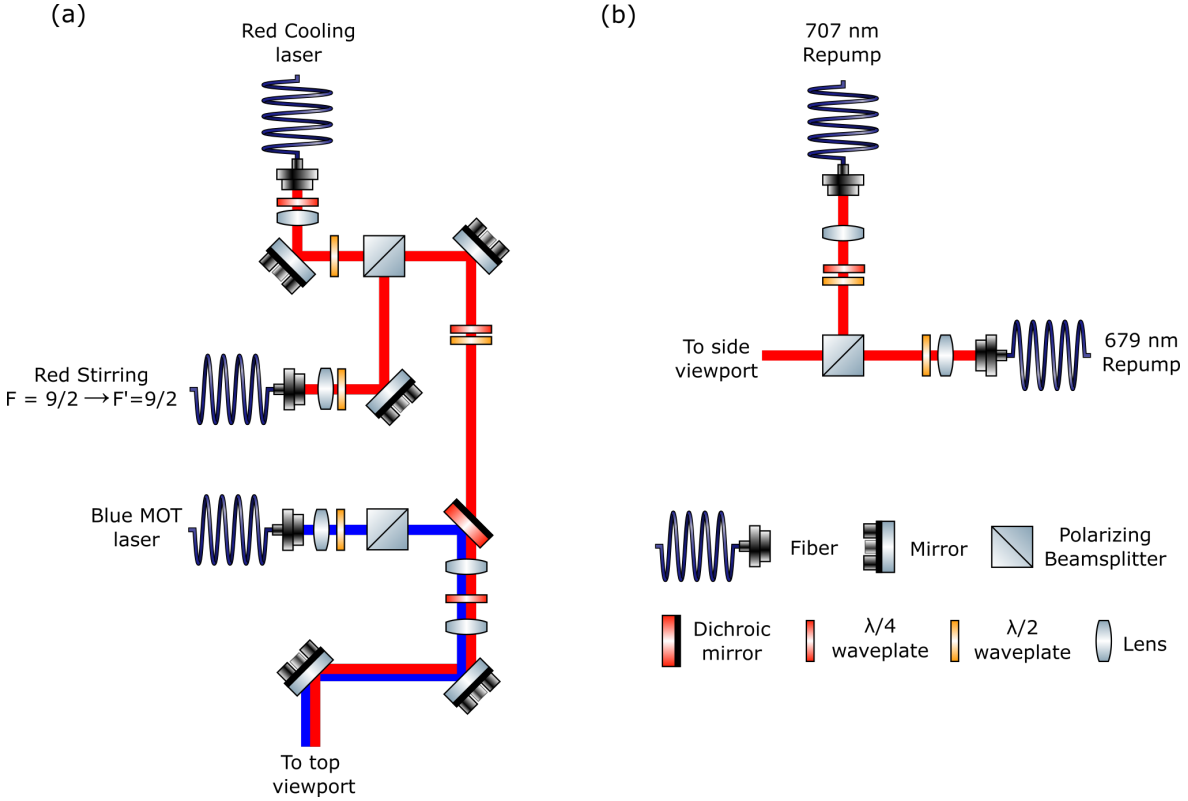


Figure 6.4: Beam launch optics for the grating MOT apparatus. (a) Optics for blue MOT laser and red MOT cooling and stirring lasers. Blue and red lasers are combined using a dichroic mirror that reflects blue and transmits red. After the dichroic mirror, we use a dual wavelength  $\lambda/4$  waveplate to ensure the same circular polarization for all beams. (b) Optics for 679 nm and 707 nm repump lasers. Both repumps are combined using a PBS and enter the chamber via the side viewport.

a dichroic mirror that transmits the red light and reflects the blue light. We use a  $\lambda/2$  waveplate and  $\lambda/4$  waveplate on the red cooling beam before the blue and red beams are combined, in addition to a  $\lambda/4$  dual wavelength waveplate after the dichroic mirror to ensure adequate control over the polarization purity of both beams. The grating in our apparatus has a measured diffraction efficiency of 37% at 689 nm. As discussed in Ch. 1, the  $^{87}\text{Sr}$  red MOT benefits from a “stirring” laser on the  $F = 9/2 \rightarrow F' = 9/2$  transition, and this is combined with the cooling laser, addressing the  $F = 9/2 \rightarrow F' = 11/2$  transition, on a PBS. We use the “Long Steck” laser as the cooling laser for

the  $^{88}\text{Sr}$  red MOT, but as the stirring laser for the  $^{87}\text{Sr}$  red MOT, while we use the injection laser as the cooling laser for  $^{87}\text{Sr}$ , as with the apparatus described in Ch. 2. The entirety of the beam launch optics is mounted to the chamber using cage mount pieces. We operate the  $^{88}\text{Sr}$  red MOT using  $1/e^2$  beam radius of 1.8 cm and a peak laser intensity of around  $18 \text{ mW/cm}^2$ , where  $I_{sat}$  for the  $^1\text{S}_0 \rightarrow ^3\text{P}_1$  transition is  $3 \mu\text{W/cm}^2$ . To achieve this peak intensity, we seed a Toptica TA-Pro tapered amplifier with the output of red cooling laser.

Because the red MOT and blue MOT operate at very different magnetic field gradients, we needed to come up with a different solution for the magnetic field than the permanent magnet configuration described in Ch. 5. We first attempted to use a combination of permanent magnets and coils. We cut the number of magnets in each magnet stack by half, giving us half of the magnetic field gradient necessary for the blue MOT from the permanent magnets. We then wound coils and controlled them using a +/- 20 A bipolar current controller [168]. This configuration did not end up working, as we were not able to switch the magnetic field gradient fast enough; the fastest switching speed the bipolar current controller could achieve was around 3 ms, since it was originally designed for shim coils. To attempt to reduce the switching time of the current control circuit, we initially designed a fast-switching circuit based on a similar concept to the one described in Section 2.9. In this circuit, instead of an IGBT, we used two power MOSFETs in series to open the circuit while switching the current. This successfully allowed us to switch the current in around 1 ms, but the added resistance from the fast-switching circuit did not allow us to get the field gradient quite low enough to achieve a red MOT and at this point, we also realized that an eddy current was being caused by the aluminum chip holder and differential pumping tube block in the chamber. To reduce the effects of

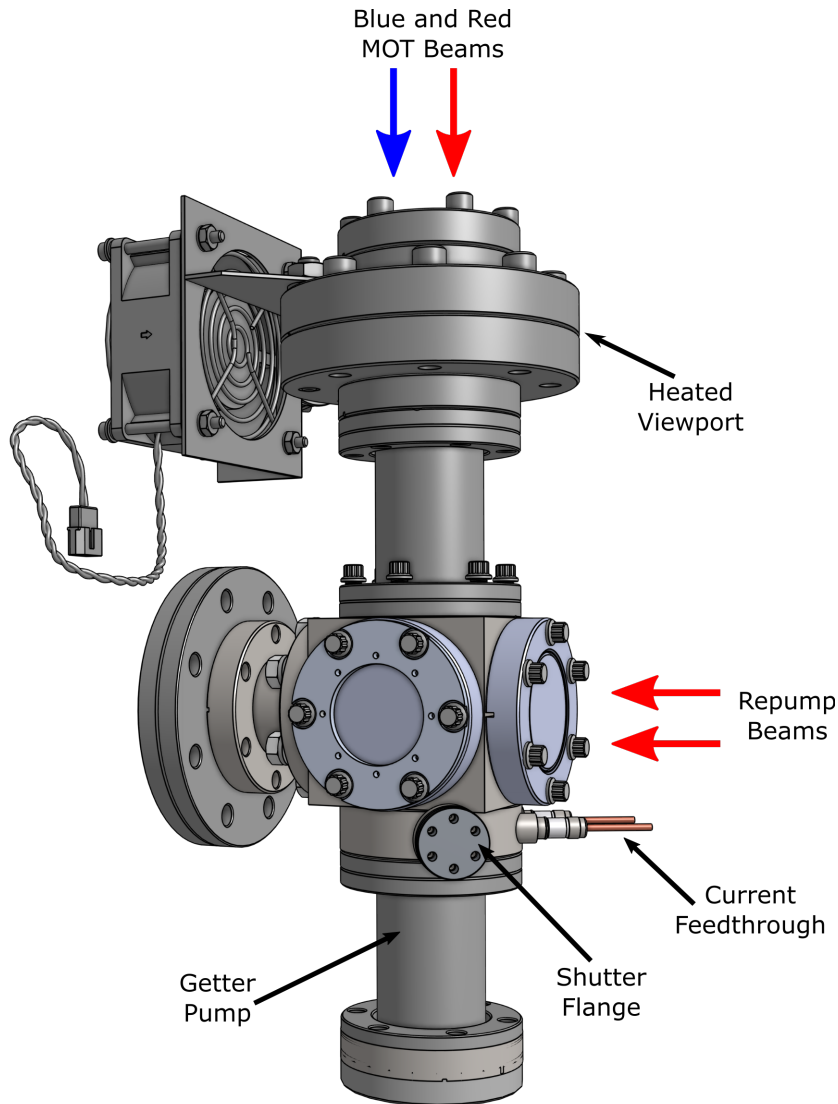


Figure 6.5: Updated vacuum apparatus for the grating MOT setup. The heated viewport sits on top of a nipple to provide separation from the main chamber and has an accompanying fan to prevent overheating. Thicker, colored arrows indicate through which viewports the blue and red MOT beams and the repump beams enter the chamber. The flange where a pneumatic atomic shutter can be incorporated is shown, just under the front viewport. Magnetic field coils are not pictured for clarity.

the eddy current, we replaced both aluminum components with identical versions made of titanium. For the coils and current control, we switched to using two sets of coils: one for the blue MOT gradient and one for the red MOT gradient. The blue MOT coils are water cooled and consist of 48 turns of 0.427 cm wide square tubing with Kapton

coating, following the design in Ref. [52]. For the red MOT coils we used flat ribbon wire that is lined with Kapton tape, and each coil has 20 turns. Using the Radia package in Mathematica to simulate both sets of coils, we calculate that the blue MOT coils produce around 0.55 G/cm/A, and the red MOT coils produce approximately 0.2 G/cm/A. We also added shim coils on the transverse axes of the apparatus, using the same copper wire as the red MOT coils and with each coil having 30 turns. For both the red MOT coils and the shim coils, we use the bipolar current controller mentioned above [168]. To shut off the current in the blue MOT coils quickly (under 1 ms), we use an IGBT in series with the coils and a similar shutoff scheme as the one described in Section 2.9.

## 6.5 Results

We have realized a  $^{88}\text{Sr}$  grating MOT on the narrow  $^1\text{S}_0 \rightarrow ^3\text{P}_1$  transition. We achieve approximately  $3 \times 10^6$  atoms in the red MOT and an average temperature of around  $3.7 \mu\text{K}$ . The MOT lifetime is approximately 0.8 s, comparable to that of the blue grating MOT. Absorption images of the blue MOT and red MOT with an approximate outline of the capture region formed by the red MOT beams can be seen in Fig. 6.6. The blue MOT forms close to the top of the red capture region, and as shown in Fig. 6.6(b), the atoms fall to a position much closer to the bottom of the red capture region in the red MOT. In this section, we will discuss the details of the experimental procedure and characterization of the MOT.

### 6.5.1 Experimental Procedure

Because our blue MOT was quite hot (several mK), we employ a “Doppler cooling” stage, similar to the one described in Chapter 4. The main difference is that we only ramp the blue MOT power down, but keep the magnetic field gradient the same, as we do not have the range to increase the magnetic field past approximately 50 G/cm on this setup. When employing a Doppler cooling stage, we have seen some improvement of the measured temperature of the blue MOT on the order of a couple mK. Though this improvement was not always consistent, we still used the Doppler cooling stage when searching for the red MOT.

To operate the red MOT stage, we use a similar experimental sequence to the one described in Ch. 4. After the blue MOT is loaded, we transfer the atoms to the red MOT by shutting off the blue light, turning on the red light, and rapidly switching the magnetic field gradient from around 50 G/cm to 3 G/cm. The initial power in our red MOT beam

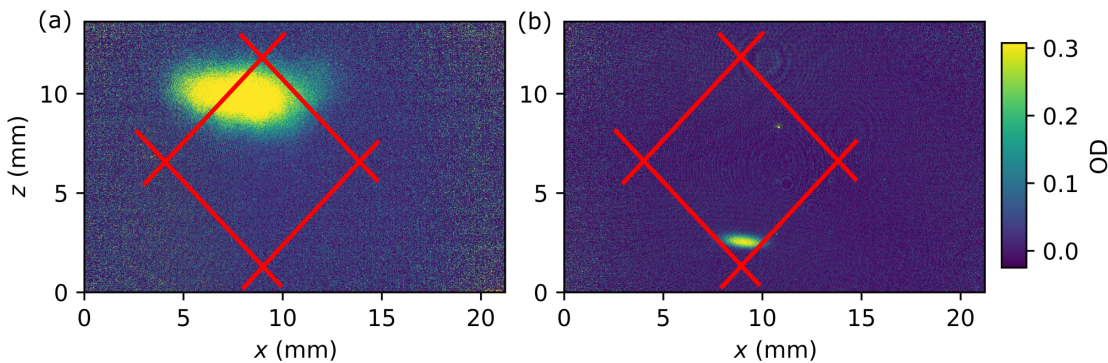


Figure 6.6: Absorption images of the blue grating MOT (a) and the red grating MOT (b) with the capture region created by the red MOT laser (red lines). The capture region is calculated for a grating chip that has four sections instead of three to aid with visualization, and is thus just an approximation. The blue MOT is shown *in situ*, whereas the red MOT is shown after 10 ms of time of flight.

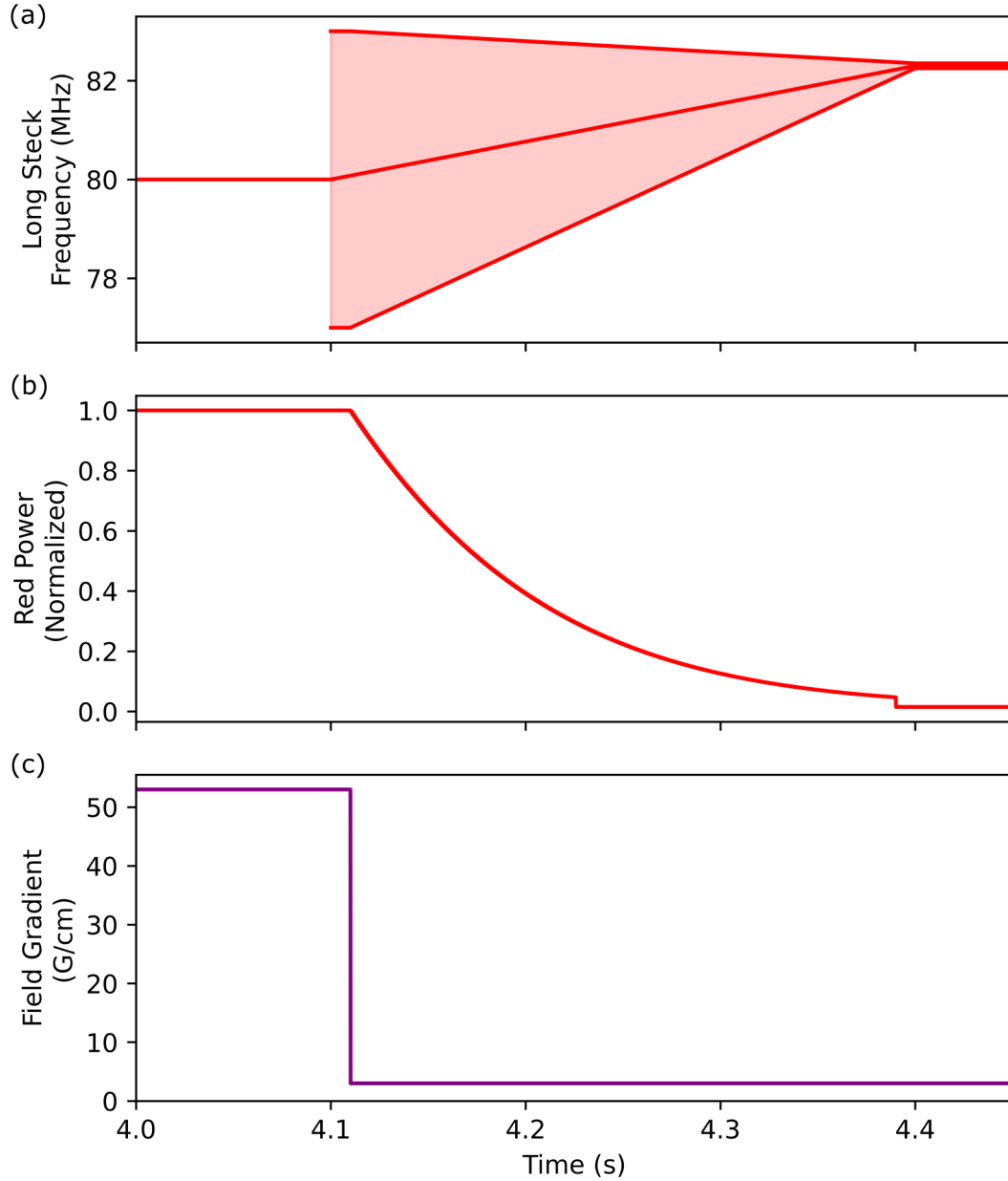


Figure 6.7: Experimental procedure for the red MOT stage. (a) Frequency of the Long Steck laser with respect to time. Broadening of 6 MHz starts at 4.1 s into the experimental shot. Upper trace indicates end frequency of sweep, and lower trace indicates start frequency of the sweep, while the center trace marks half of the sweep range ( $\Delta/2$ ) above the start frequency. (b) Normalized power in the red cooling laser (Long Steck) with respect to time. The red MOT laser power starts at its maximum value and decreases to 0 mW of power over the course of the broadening. (c) Field gradient with respect to time. The field gradient begins around 50 G/cm in the blue MOT stage and drops to the red MOT gradient of around 3 G/cm in under 1 ms.

entering the chamber is around 45 mW. To switch the magnetic field, we actually just shut off the larger blue MOT coils by opening the IGBT and leave on the smaller red MOT coils which give the appropriate red MOT gradient. At the same time that the blue MOT gradient is turned off, we begin to modulate the frequency of the red MOT laser, using the sawtooth wave described in Section 6.2. The initial modulation span of the red laser is 6 MHz, and this span is ramped down to 0.1 MHz over the course of the red MOT loading time (around 0.3 s). The center frequency of the sawtooth wave sweep begins around 2 MHz red detuned from resonance and is ramped closer to resonance. The end frequency of the sweep is slightly blue detuned of resonance at the beginning of the red MOT loading period. Similar to the red MOT in our main apparatus, we do not implement a single frequency compression stage, as it did not seem to make a difference to the MOT.

### 6.5.2 Demonstration of SWAP

Having made these changes to the apparatus, we have successfully demonstrated SWAP in a grating magneto-optical trap with  $^{88}\text{Sr}$ . Using SWAP with a sweep time  $T_s$  of  $50 \mu\text{s}$ , we measured the atom number vs. final detuning of the red laser using a sawtooth wave at 20 kHz, triangle wave at 20 kHz, opposite sawtooth wave (anti-SWAP) at 20 kHz, and triangle wave at 10 kHz, as shown in Fig. 6.8. We investigate two different sweep frequencies for the triangle wave because at 10 kHz, the sweep rate is the same as that of a sawtooth wave at 20 kHz. However, we still include the triangle wave data at 20 kHz, which is more optimal for the triangle wave MOT, to show that it is still worse than the sawtooth wave at its optimal sweep frequency. With the correct sawtooth wave, we get

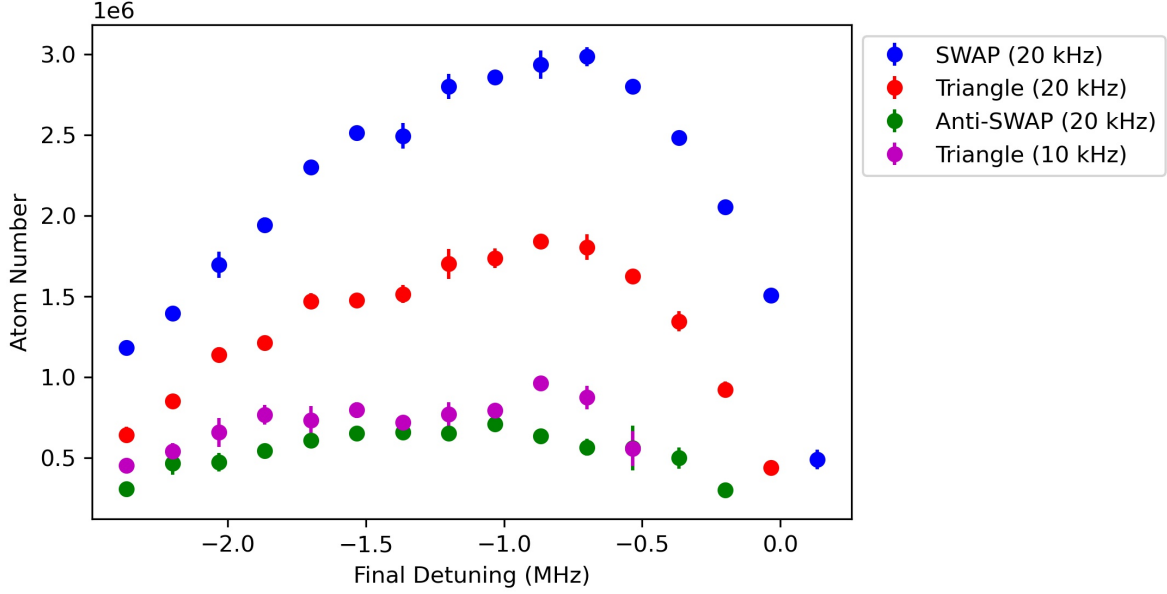


Figure 6.8: Comparison of atom number vs. final detuning of red MOT laser for SWAP (20 kHz), triangle wave (20 kHz), Anti-SWAP (20 kHz), and triangle wave (10 kHz). Frequency in parenthesis is modulation frequency, or  $1/T_s$ .

a peak atom number of around  $3 \times 10^6$  atoms, while using a triangle wave only yields approximately  $1.7 \times 10^6$  atoms, at best. We can also see that for the anti-SWAP wave, the atom number is a factor of 6 lower (green circles) than that of SWAP. We estimate the detuning at our peak atom number as around 500 kHz, where we take resonance as the frequency at which the atom number drops off using triangle wave modulation.

To measure the temperature, we calculate the root-mean-square width of the atomic cloud using a Gaussian fit, while varying the time of flight from 0 to 20 ms. As with the blue grating MOT in Ch. 4, we fit the data to  $w(t)^2 = w_0(t)^2 + v_{rms}^2 t^2$ , where  $w_0$  is the initial rms width of the cloud,  $v_{rms} = \sqrt{k_B T / m}$  is the rms velocity,  $k_B$  is Boltzmann's constant,  $m$  is the atomic mass, and  $T$  is the temperature of the atomic cloud. The calculated temperature is  $4.5(6) \mu\text{K}$  in the transverse direction,  $\hat{y}$ , and  $2.9(1) \mu\text{K}$  in the axial direction,  $\hat{z}$ . These temperatures are comparable to that of our  $^{88}\text{Sr}$  red MOT using

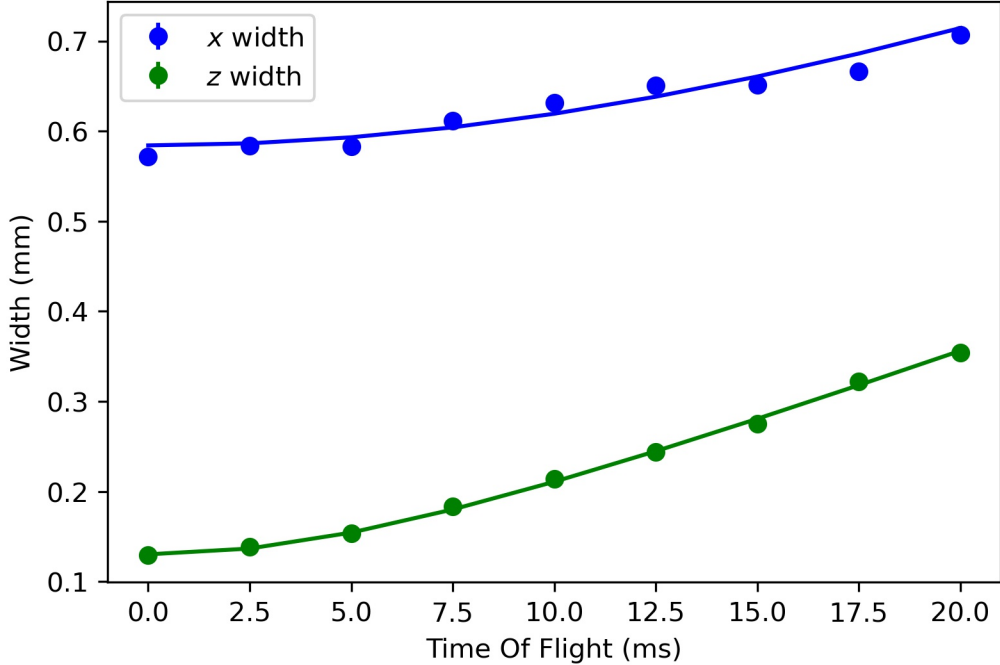


Figure 6.9: Temperature measurement of red MOT of  $^{88}\text{Sr}$ . The rms width of the atomic cloud in the  $\hat{y}$  direction (blue circles) and in the  $\hat{z}$  direction (green circles) are plotted against time of flight and fitted to the expansion function discussed in Section 5.1.4 (blue/green curves). The calculated temperatures based on the fits are  $4.5(6) \mu\text{K}$  and  $2.9(1) \mu\text{K}$  for  $\hat{y}$  and  $\hat{z}$ , respectively, and the errors in parentheses are one standard deviation. The error bars are smaller than the data points and represent the standard error about the mean.

the conventional six-beam apparatus, where we get an average temperature of  $\sim 5 \mu\text{K}$ .

We also report the lifetime of the red grating MOT of  $^{88}\text{Sr}$ . To measure the lifetime, we introduce a hold time, an interval where we hold the trapped red MOT atoms in the trap at all of the final values of the experimental parameters shown in Fig. 6.7. We then take a sequence of experimental shots, measuring the atom number in the MOT while varying the hold time from 0 to 1.5 s. We fit these data to an exponential decay curve:  $N(t) = N_0 e^{-t/\tau}$ . The data with the fitted curve is shown in Fig. 6.10. From the decay constant of the fit we calculate a lifetime of approximately 0.8 s, which is roughly similar to our blue grating MOT lifetime and is consistent with a vacuum-limited lifetime for our

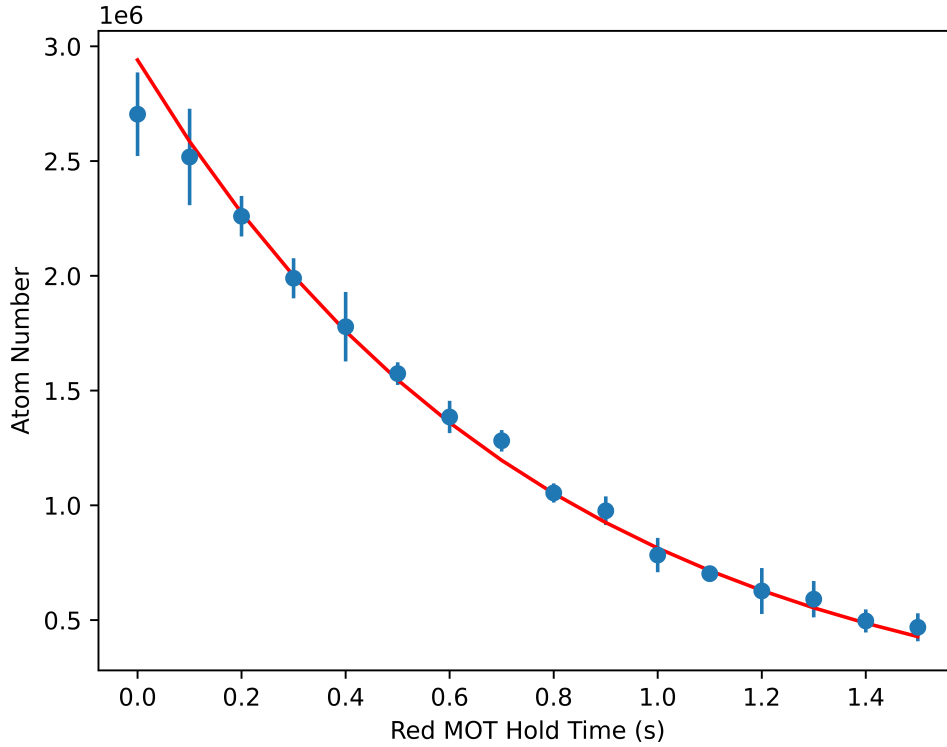


Figure 6.10: Measurement of the lifetime of the red MOT. Atom number (blue dots) is shown with respect to the red MOT hold time. Error bars are the standard error about the mean. Data points are fitted to an exponential decay curve (red curve). We calculate the lifetime as  $1/\tau = 0.8$  s, where  $\tau$  is the time constant of the fitted curve.

vacuum pressure in the low  $10^{-7}$  Pa range.

## 6.6 Future Work

Now that we have trapped  $^{88}\text{Sr}$  in the red MOT with our grating apparatus, we will attempt to try to make the red MOT work with  $^{87}\text{Sr}$  as well. Because  $^{87}\text{Sr}$  has a nuclear spin of  $9/2$ , the  $^3\text{P}_1$  state gets split into 10 hyperfine states, as described in Chapter 1. As with the conventional six-beam fermionic red MOT, we would expect to have to use a stirring laser in addition to the cooling laser. We initially tried to achieve the fermionic red MOT simply using the SWAP technique on the red cooling laser and no

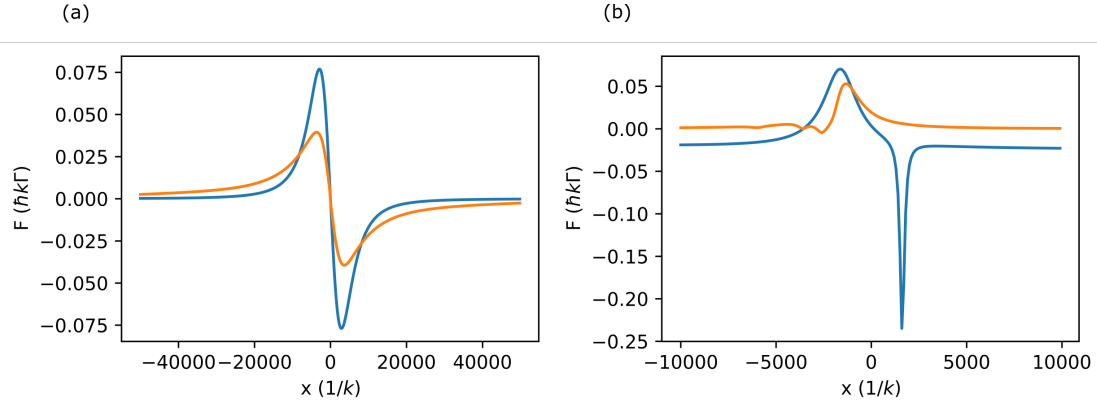


Figure 6.11: Simulations using PyLCP of the axial force profiles for both  $^{88}\text{Sr}$  (blue curve) and  $^{87}\text{Sr}$  (orange curve) without the stirring laser. (a)  $^{88}\text{Sr}$  and  $^{87}\text{Sr}$  force vs. position in a conventional six-beam MOT. (b)  $^{88}\text{Sr}$  and  $^{87}\text{Sr}$  force vs. position in a grating MOT configuration.

stirring, but were not successful. Upon further investigation into simulations of the  $^{87}\text{Sr}$  red MOT in a grating configuration, it seems that the trap will not be possible without a stirring laser. This stands in contrast to the fermionic red MOT using the conventional six-beam configuration. In Fig. 6.11, we can see that while for a conventional MOT, we still get the appropriate trapping force profile for both  $^{88}\text{Sr}$  and  $^{87}\text{Sr}$ , for  $^{87}\text{Sr}$  in the grating configuration, we no longer get a trapping force without the stirring laser.

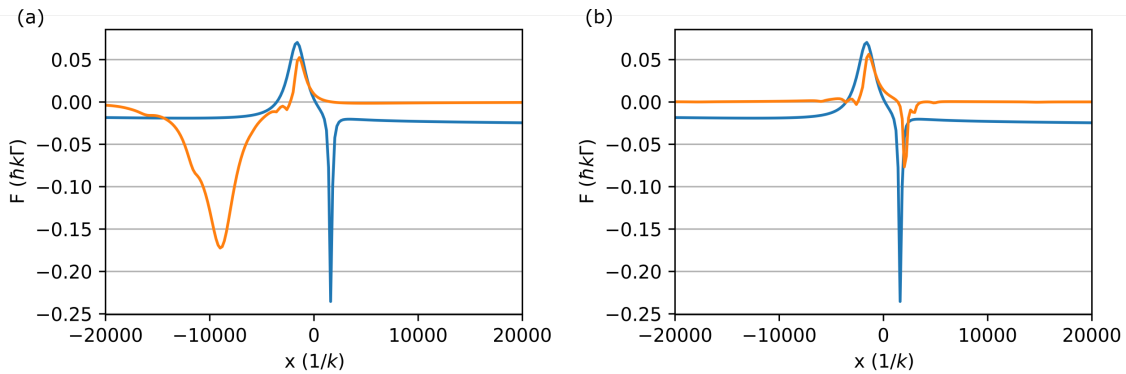


Figure 6.12: Simulations using PyLCP of the axial force profiles for both  $^{88}\text{Sr}$  (blue curve) and  $^{87}\text{Sr}$  (orange curve) with stirring on the  $F = 9/2 \rightarrow F' = 9/2$  transition (a) and the  $F = 9/2 \rightarrow F' = 7/2$  transition (b).

Simulations with PyLCP also show that the stirring of the MOT behaves differently in the grating MOT setup, shown in Fig. 6.12. Stirring on the usual  $F = 9/2 \rightarrow F' = 9/2$  hyperfine transition (Fig. 6.12(a)) does not produce proper confinement, and seems only to work if the stirring laser has the opposite circular polarization to the red cooling laser. Interestingly, in the grating MOT, stirring on the  $F = 9/2 \rightarrow F' = 7/2$  transition (Fig. 6.12(b)) may be possible, which is not the case for six-beam strontium MOTs. We have not implemented stirring on this transition yet, but will in the future.

## 6.7 Conclusion and Outlook

We have demonstrated sawtooth wave adiabatic passage in a narrow line MOT of  $^{88}\text{Sr}$ . We have shown that using sawtooth wave modulation on the red MOT laser instead of a triangle wave gives approximately a factor of 2 increase in the atom number in the trap, which is a more substantial increase than was reported for  $^{88}\text{Sr}$  in a conventional six-beam system [157]. We believe this is due to the SWAP mechanism described in Section 6.2, which still relies on spontaneous emission at high magnetic fields, but allows for stimulated SWAP cooling close to the magnetic field zero. It is also possible that the polarization components of diffracted beams in the tetrahedral geometry trap allow for SWAP cooling to occur at higher magnetic fields, as you can get time-ordered absorption and emission from the “incorrect” polarization beam from either side in the trap. Similarly, the  $\pi$  polarized components of the diffracted beams could cause some of the stimulated SWAP cooling mechanism to occur in the transverse direction.

With enough power in the stirring laser, it is possible that we could make the  $^{87}\text{Sr}$  red

MOT work with the grating apparatus, and this would have even more impact because of the fermion's unique characteristics and applications to atomic clocks and other quantum devices. Even with just  $^{88}\text{Sr}$ , the experiment is now at the stage that the atoms in the red MOT could possibly be loaded into a dipole trap and also opens the door to many other applications, such as clock-state interferometers [169–171]. Our experiments show that grating MOTs are a promising direction for compact quantum devices with strontium.

## Bibliography

- [1] T. H. MAIMAN. Stimulated optical radiation in ruby. *Nature*, 187(4736):493–494, August 1960.
- [2] William D. Phillips. Nobel lecture: Laser cooling and trapping of neutral atoms. *Rev. Mod. Phys.*, 70:721–741, Jul 1998.
- [3] A. Ashkin. Atomic-beam deflection by resonance-radiation pressure. *Phys. Rev. Lett.*, 25:1321–1324, Nov 1970.
- [4] A. Ashkin. Trapping of atoms by resonance radiation pressure. *Phys. Rev. Lett.*, 40:729–732, Mar 1978.
- [5] William D. Phillips, John V. Prodan, and Harold J. Metcalf. Laser cooling and electromagnetic trapping of neutral atoms. *J. Opt. Soc. Am. B*, 2(11):1751–1767, Nov 1985.
- [6] M. H. Anderson, J. R. Ensher, M. R. Matthews, C. E. Wieman, and E. A. Cornell. Observation of bose-einstein condensation in a dilute atomic vapor. *Science*, 269(5221):198–201, 1995.
- [7] K. B. Davis, M. O. Mewes, M. R. Andrews, N. J. van Druten, D. S. Durfee, D. M. Kurn, and W. Ketterle. Bose-einstein condensation in a gas of sodium atoms. *Phys. Rev. Lett.*, 75:3969–3973, Nov 1995.
- [8] B. DeMarco and D. S. Jin. Onset of fermi degeneracy in a trapped atomic gas. *Science*, 285(5434):1703–1706, 1999.
- [9] M. Saffman, T. G. Walker, and K. Mølmer. Quantum information with rydberg atoms. *Rev. Mod. Phys.*, 82:2313–2363, Aug 2010.
- [10] I. M. Georgescu, S. Ashhab, and Franco Nori. Quantum simulation. *Rev. Mod. Phys.*, 86:153–185, Mar 2014.

- [11] Travis Nicholson, S. Campbell, Ross Hutson, Edward Marti, B. Bloom, R. McNally, W. Zhang, M. Barrett, Marianna Safronova, G. Strouse, W. Tew, and Jun Ye. Systematic evaluation of an atomic clock at  $2 \times 10^{-18}$  total uncertainty. *Nature Communications*, 6:6896, 2015-04 2015.
- [12] N. Hinkley, J. A. Sherman, N. B. Phillips, M. Schioppo, N. D. Lemke, K. Beloy, M. Pizzocaro, C. W. Oates, and A. D. Ludlow. An Atomic Clock with  $10^{-18}$  Instability. *Science*, 341:1215, 2013.
- [13] Schwab D.J. Tsai J.J. Coursey, J.S. and R.A. Dragoset. Atomic weights and isotopic compositions (version 4.1), 2015.
- [14] Y. N. Martinez de Escobar, P. G. Mickelson, P. Pellegrini, S. B. Nagel, A. Traverso, M. Yan, R. Côté, and T. C. Killian. Two-photon photoassociative spectroscopy of ultracold  $^{88}\text{Sr}$ . *Phys. Rev. A*, 78:062708, Dec 2008.
- [15] Alexander Stein, Horst Knöckel, and Eberhard Tiemann. The  $1s+1s$  asymptote of  $\text{sr}^2$  studied by fourier-transform spectroscopy. *The European Physical Journal D*, 57:171–177, 2010.
- [16] Simon Stellmer, Rudolf Grimm, and Florian Schreck. Production of quantum-degenerate strontium gases. *Phys. Rev. A*, 87:013611, Jan 2013.
- [17] Charles S. Adams, Heun Jin Lee, Nir Davidson, Mark Kasevich, and Steven Chu. Evaporative cooling in a crossed dipole trap. *Phys. Rev. Lett.*, 74:3577–3580, May 1995.
- [18] Simon Stellmer, Meng Khoon Tey, Bo Huang, Rudolf Grimm, and Florian Schreck. Bose-einstein condensation of strontium. *Phys. Rev. Lett.*, 103:200401, Nov 2009.
- [19] Y. N. Martinez de Escobar, P. G. Mickelson, M. Yan, B. J. DeSalvo, S. B. Nagel, and T. C. Killian. Bose-einstein condensation of  $^{84}\text{Sr}$ . *Phys. Rev. Lett.*, 103:200402, Nov 2009.
- [20] P. G. Mickelson, Y. N. Martinez de Escobar, M. Yan, B. J. DeSalvo, and T. C. Killian. Bose-einstein condensation of  $^{88}\text{Sr}$  through sympathetic cooling with  $^{87}\text{Sr}$ . *Phys. Rev. A*, 81:051601, May 2010.
- [21] B. J. DeSalvo, M. Yan, P. G. Mickelson, Y. N. Martinez de Escobar, and T. C. Killian. Degenerate fermi gas of  $^{87}\text{Sr}$ . *Phys. Rev. Lett.*, 105:030402, Jul 2010.
- [22] Meng Khoon Tey, Simon Stellmer, Rudolf Grimm, and Florian Schreck. Double-degenerate bose-fermi mixture of strontium. *Phys. Rev. A*, 82:011608, Jul 2010.
- [23] Simon Stellmer, Meng Khoon Tey, Rudolf Grimm, and Florian Schreck. Bose-einstein condensation of  $^{86}\text{Sr}$ . *Phys. Rev. A*, 82:041602, Oct 2010.
- [24] M. M. Boyd. *High Precision Spectroscopy of Strontium in an Optical Lattice: Towards a New Standard for Frequency and Time*. PhD thesis, University of Colorado, Boulder, 2007.

- [25] A. V. Gorshkov, A. M. Rey, A. J. Daley, M. M. Boyd, J. Ye, P. Zoller, and M. D. Lukin. Alkaline-earth-metal atoms as few-qubit quantum registers. *Phys. Rev. Lett.*, 102:110503, Mar 2009.
- [26] Andrew J. Daley, Martin M. Boyd, Jun Ye, and Peter Zoller. Quantum computing with alkaline-earth-metal atoms. *Phys. Rev. Lett.*, 101:170504, Oct 2008.
- [27] Michael E. Beverland, Gorjan Alagic, Michael J. Martin, Andrew P. Koller, Ana M. Rey, and Alexey V. Gorshkov. Realizing exactly solvable  $SU(n)$  magnets with thermal atoms. *Phys. Rev. A*, 93:051601, May 2016.
- [28] Michael E. Beverland, Jeongwan Haah, Gorjan Alagic, Gretchen K. Campbell, Ana Maria Rey, and Alexey V. Gorshkov. Spectrum estimation of density operators with alkaline-earth atoms. *Phys. Rev. Lett.*, 120:025301, Jan 2018.
- [29] X. Zhang, M. Bishof, S. L. Bromley, C. V. Kraus, M. S. Safronova, P. Zoller, A. M. Rey, and J. Ye. Spectroscopic observation of  $su(n)$ -symmetric interactions in sr orbital magnetism. *Science*, 345(6203):1467–1473, 2014.
- [30] C W Bauschlicher, S R Langhoff, R L Jaffe, and H Partridge. Theoretical electric quadrupole transition probabilities for ca, sr and ba. *Journal of Physics B: Atomic and Molecular Physics*, 17(13):L427–L431, jul 1984.
- [31] L. R. Hunter, W. A. Walker, and D. S. Weiss. Observation of an atomic stark–electric-quadrupole interference. *Phys. Rev. Lett.*, 56:823–826, Feb 1986.
- [32] S. B. Nagel, P. G. Mickelson, A. D. Saenz, Y. N. Martinez, Y. C. Chen, T. C. Killian, P. Pellegrini, and R. Côté. Photoassociative spectroscopy at long range in ultracold strontium. *Phys. Rev. Lett.*, 94:083004, Mar 2005.
- [33] Masami Yasuda, Tetsuo Kishimoto, Masao Takamoto, and Hidetoshi Katori. Photoassociation spectroscopy of  $^{88}\text{Sr}$ : Reconstruction of the wave function near the last node. *Phys. Rev. A*, 73:011403, Jan 2006.
- [34] J. E. Sansonetti and G. Nave. Wavelengths, transition probabilities, and energy levels for the spectrum of neutral strontium (sri). *Journal of Physical and Chemical Reference Data*, 39(3):033103, 2010.
- [35] D. S. Barker, B. J. Reschovsky, N. C. Pimenti, and G. K. Campbell. Enhanced magnetic trap loading for atomic strontium. *Phys. Rev. A*, 92:043418, Oct 2015.
- [36] P G Mickelson, Y N Martinez de Escobar, P Anzel, B J DeSalvo, S B Nagel, A J Traverso, M Yan, and T C Killian. Repumping and spectroscopy of laser-cooled sr atoms using the  $(5s5p)^3_{sup3}/supsub2/sub-(5s4d)^3_{sup3}/supsub2/sub$  transition. *Journal of Physics B: Atomic, Molecular and Optical Physics*, 42(23):235001, nov 2009.

- [37] S. B. Nagel, C. E. Simien, S. Laha, P. Gupta, V. S. Ashoka, and T. C. Killian. Magnetic trapping of metastable  $^3P_{-2}$  atomic strontium. *Physical Review A*, 67:011401(R), 2003.
- [38] B. Reschovsky. *Studies of Ultracold Strontium Gases*. PhD thesis, University of Maryland, College Park, 2017.
- [39] B.A. Bushaw and W. Nörtershäuser. Resonance ionization spectroscopy of stable strontium isotopes and  $^{90}\text{Sr}$  via  $5s^2 1s_0 \rightarrow 5s5p 1p_1 \rightarrow 5s5d 1d_2 \rightarrow 5s11f 1f_3 \rightarrow \text{sr}^+$ . *Spectrochimica Acta Part B: Atomic Spectroscopy*, 55(11):1679–1692, 2000.
- [40] Gisbert Zu Putlitz. Bestimmung des elektrischen Kernquadrupolmomentes des ungeraden stabilen Strontium-87-Kerns. *Zeitschrift für Physik*, 175(5):543–552, October 1963.
- [41] Stephan M. Heider and Gilbert O. Brink. Hyperfine structure of  $^{87}\text{Sr}$  in the  $^3p_2$  metastable state. *Phys. Rev. A*, 16:1371–1374, Oct 1977.
- [42] I. Courtilot, A. Quessada-Vial, A. Bruschi, D. Kolker, G. D. Rovera, and P. Lemonde. Accurate spectroscopy of Sr atoms. *European Physical Journal D*, 33(2):161–171, May 2005.
- [43] M. Norcia. *New Tools for Precision Measurement and Quantum Science with Narrow Linewidth Optical Transitions*. PhD thesis, University of Colorado, Boulder, 2017.
- [44] Fachao Hu, Canzhu Tan, Yuhai Jiang, Matthias Weidemüller, and Bing Zhu. Observation of photon recoil effects in single-beam absorption spectroscopy with an ultracold strontium gas. *Chinese Physics B*, 31(1):016702, Jan 2022.
- [45] F. SORRENTINO, G. FERRARI, N. POLI, R. DRULLINGER, and G. M. TINO. Laser cooling and trapping of atomic strontium for ultracold atoms physics, high-precision spectroscopy and quantum sensors. *Modern Physics Letters B*, 20(21):1287–1320, 2006.
- [46] Neal Carden Piseni. *Isotope Shift Spectroscopy of Ultracold Strontium*. PhD thesis, University of Maryland, 2019.
- [47] Takashi Mukaiyama, Hidetoshi Katori, Tetsuya Ido, Ying Li, and Makoto Kuwata-Gonokami. Recoil-limited laser cooling of  $^{87}\text{Sr}$  atoms near the fermi temperature. *Phys. Rev. Lett.*, 90:113002, Mar 2003.
- [48] Rudolf Grimm, Matthias Weidemüller, and Yurii B. Ovchinnikov. Optical dipole traps for neutral atoms. volume 42 of *Advances In Atomic, Molecular, and Optical Physics*, pages 95–170. Academic Press, 2000.
- [49] Immanuel Bloch, Jean Dalibard, and Wilhelm Zwerger. Many-body physics with ultracold gases. *Rev. Mod. Phys.*, 80:885–964, Jul 2008.

- [50] Immanuel Bloch, Jean Dalibard, and Sylvain. Quantum simulations with ultracold quantum gases. *Nature Physics*, 8:267–276, 04 2012.
- [51] L.-M. Duan, E. Demler, and M. D. Lukin. Controlling spin exchange interactions of ultracold atoms in optical lattices. *Phys. Rev. Lett.*, 91:090402, Aug 2003.
- [52] D. S. Barker. *Degenerate Gases of Strontium for Studies of Quantum Magnetism*. PhD thesis, University of Maryland, College Park, 2016.
- [53] Norman F. Ramsey. Experiments with separated oscillatory fields and hydrogen masers (nobel lecture). *Angewandte Chemie International Edition in English*, 29(7):725–733, 1990.
- [54] M. Kafatos. *Bell’s Theorem, Quantum Theory and Conceptions of the Universe*. Fundamental Theories of Physics. Springer Netherlands, 2013.
- [55] J. J . Bollinger, Wayne M. Itano, D. J. Wineland, and D. J. Heinzen. Optimal frequency measurements with maximally correlated states. *Phys. Rev. A*, 54:R4649–R4652, Dec 1996.
- [56] F. Shimizu, K. Shimizu, and H. Takuma. Four-beam laser trap of neutral atoms. *Optics Letters*, 16(5):339, 1991.
- [57] Takayuki Kurosu and Fujio Shimizu. Laser cooling and trapping of calcium and strontium. *Japanese Journal of Applied Physics*, 29(Part 2, No. 11):L2127–L2129, nov 1990.
- [58] D. S. Barker, E. B. Norrgard, N. N. Klimov, J. A. Fedchak, J. Scherschligt, and S. Eckel. Single-Beam Zeeman Slower and Magneto-Optical Trap Using a Nanofabricated Grating. *Physical Review Applied*, 11(6):1–8, 2019.
- [59] William R McGehee, Wenqi Zhu, Daniel S Barker, Daron Westly, Alexander Yulaev, Nikolai Klimov, Amit Agrawal, Stephen Eckel, Vladimir Aksyuk, and Jabez J McClelland. Magneto-optical trapping using planar optics. *New Journal of Physics*, 23(1):013021, jan 2021.
- [60] Tobias Bothwell, Dhruv Kedar, Eric Oelker, John M Robinson, Sarah L Bromley, Weston L Tew, Jun Ye, and Colin J Kennedy. JILA SrI optical lattice clock with uncertainty of  $2.0 \times 10^{-18}$ . *Metrologia*, 56(6):065004, oct 2019.
- [61] Piotr Morzyński, Marcin Bober, Dobrosława Bartoszek-Bober, Jerzy Nawrocki, Przemysław Krehlik, Łukasz Śliwczyński, Marcin Lipiński, Piotr Masłowski, Agata Cygan, Piotr Dunst, et al. Absolute measurement of the  $^1S_0$ - $^3P_0$  clock transition in neutral  $^{88}\text{Sr}$  over the 330 km-long stabilized fibre optic link. *Scientific reports*, 5:17495, 2015.
- [62] Peter W. Graham, Jason M. Hogan, Mark A. Kasevich, and Surjeet Rajendran. New Method for Gravitational Wave Detection with Atomic Sensors. *Physical Review Letters*, 110(17):171102, apr 2013.

- [63] A. Vutha. Optical frequency standards for gravitational wave detection using satellite Doppler velocimetry. *New Journal of Physics*, 17:063030, 2015.
- [64] Stephen Eckel, Daniel S. Barker, Eric B. Norrgard, and Julia Scherschligt. Pylcp: A python package for computing laser cooling physics. *Computer Physics Communications*, 270:108166, 2022.
- [65] C P Pearman, C S Adams, S G Cox, P F Griffin, D A Smith, and I G Hughes. Polarization spectroscopy of a closed atomic transition: applications to laser frequency locking. *Journal of Physics B: Atomic, Molecular and Optical Physics*, 35(24):5141–5151, dec 2002.
- [66] R. Drever, John Hall, F. Kowalski, J. Hough, G. Ford, A. Munley, and H. Ward. Laser phase and frequency stabilization using an optical resonator. *Applied Physics B Photophysics and Laser Chemistry*, 31:97–105, Jan-06-1983 1983.
- [67] Eryn C. Cook, Paul J. Martin, Tobias L. Brown-Heft, Jeffrey C. Garman, and Daniel A. Steck. High passive-stability diode-laser design for use in atomic-physics experiments. *Review of Scientific Instruments*, 83(4):043101, 2012.
- [68] D. R. Leibbrandt and J. Heidecker. An open source digital servo for atomic, molecular, and optical physics experiments. *Review of Scientific Instruments*, 86(12):123115, 2015.
- [69] J. D. Pritchard, J. A. Isaacs, and M. Saffman. Long working distance objective lenses for single atom trapping and imaging. *Review of Scientific Instruments*, 87(7):073107, 2016.
- [70] Ren Zhang, Yanting Cheng, Hui Zhai, and Peng Zhang. Orbital feshbach resonance in alkali-earth atoms. *Phys. Rev. Lett.*, 115:135301, Sep 2015.
- [71] G. Pagano, M. Mancini, G. Cappellini, L. Livi, C. Sias, J. Catani, M. Inguscio, and L. Fallani. Strongly interacting gas of two-electron fermions at an orbital feshbach resonance. *Phys. Rev. Lett.*, 115:265301, Dec 2015.
- [72] M. Höfer, L. Riegger, F. Scazza, C. Hofrichter, D. R. Fernandes, M. M. Parish, J. Levinsen, I. Bloch, and S. Fölling. Observation of an orbital interaction-induced feshbach resonance in  $^{173}\text{Yb}$ . *Phys. Rev. Lett.*, 115:265302, Dec 2015.
- [73] Tian Luan, Tianwei Zhou, Xuzong Chen, and Zhaoyuan Ma. A modified bitter-type electromagnet and control system for cold atom experiments. *Review of Scientific Instruments*, 85(2):024701, 2014.
- [74] Dylan O. Sabulsky, Colin V. Parker, Nathan D. Gemelke, and Cheng Chin. Efficient continuous-duty bitter-type electromagnets for cold atom experiments. *Review of Scientific Instruments*, 84(10):104706, 2013.
- [75] Danisense ds200id datasheet. <https://www.danisense.com/images/pdf/0-600A/DS200ID.pdf>. Accessed: 2020-05-07.

- [76] International rectifier ir2117(s)/ir2118(s) & (pbf) datasheet. <https://www.infineon.com/dgdl/ir2117.pdf?fileId=5546d462533600a4015355c84331168d>. Accessed: 2020-05-07.
- [77] John Bechhoefer. Feedback for physicists: A tutorial essay on contro. *Reviews of Modern Physics*, 77(3):783–836, jul 2005.
- [78] Bode-100 network analyzer technical datasheet. [https://www.omicron-lab.com/fileadmin/assets/Bode\\_100/Documents/Bode\\_100\\_R2\\_Technical\\_Data\\_V1.2.pdf](https://www.omicron-lab.com/fileadmin/assets/Bode_100/Documents/Bode_100_R2_Technical_Data_V1.2.pdf). Accessed: 2020-05-08.
- [79] Epcos varistor datasheet. [https://www.tdk-electronics.tdk.com/inf/70/db/var/SIOV\\_Leaded\\_StandarD.pdf](https://www.tdk-electronics.tdk.com/inf/70/db/var/SIOV_Leaded_StandarD.pdf). Accessed: 2020-05-07.
- [80] Hcnr200 and hcnr201 datasheet. [https://www.mouser.com/datasheet/2/678/av02-0886en\\_ds\\_hcnr200\\_2014-01-07-1827983.pdf](https://www.mouser.com/datasheet/2/678/av02-0886en_ds_hcnr200_2014-01-07-1827983.pdf). Accessed:2020-05-11.
- [81] Paul Horowitz and Winfield Hill. *The art of electronics; 3rd ed.*, chapter 12.7.4 IV: Analog-oriented optocouplers, pages 847–849. Cambridge University Press, Cambridge, 2015.
- [82] Analog devices ad825 datasheet. <https://www.analog.com/media/en/technical-documentation/data-sheets/AD825.pdf>. Accessed: 2020-05-08.
- [83] Texas instruments buf634a datasheet. <https://www.ti.com/lit/ds/symlink/buf634a.pdf?&ts=1588957324474>. Accessed: 2020-05-08.
- [84] P. T. Starkey, C. J. Billington, S. P. Johnstone, M. Jasperse, K. Helmersen, L. D. Turner, and R. P. Anderson. A scripted control system for autonomous hardware-timed experiments. *Review of Scientific Instruments*, 84(8):085111, 2013.
- [85] Setlist github repository. <https://github.com/JQIamo/SetList>. Accessed: 2020-05-11.
- [86] A. Sitaram, G. K. Campbell, and A. Restelli. Programmable system on chip for controlling an atomic physics experiment. *Review of Scientific Instruments*, 92(5):055107, 2021.
- [87] J. Ignacio Cirac and Peter Zoller. Goals and opportunities in quantum simulation. *Nature Physics*, 8(4):264–266, Apr 2012.
- [88] Frank Verstraete, Michael M. Wolf, and J. Ignacio Cirac. Quantum computation and quantum-state engineering driven by dissipation. *Nature Physics*, 5(9):633–636, Sep 2009.
- [89] Jun Ye, H. J. Kimble, and Hidetoshi Katori. Quantum state engineering and precision metrology using state-insensitive light traps. *Science*, 320(5884):1734–1738, 2008.

- [90] F. Sorrentino, A. Alberti, G. Ferrari, V. V. Ivanov, N. Poli, M. Schioppo, and G. M. Tino. Quantum sensor for atom-surface interactions below  $10 \mu\text{m}$ . *Phys. Rev. A*, 79:013409, Jan 2009.
- [91] Certain commercial products or company names are identified here to describe our study adequately. Such identification is not intended to imply recommendation or endorsement by the National Institute of Standards and Technology, nor is it intended to imply that the products or names identified are necessarily the best available for the purpose.
- [92] Manish Patel, Ahmad Sakaamini, Matthew Harvey, and Andrew James Murray. An experimental control system for electron spectrometers using arduino and labview interfaces. *Review of Scientific Instruments*, 91(10):103104, 2020.
- [93] Radim Hořák and Miroslav Ježek. Arbitrary digital pulse sequence generator with delay-loop timing. *Review of Scientific Instruments*, 89(4):045103, 2018.
- [94] Peter E. Gaskell, Jeremy J. Thorn, Sequoia Alba, and Daniel A. Steck. An open-source, extensible system for laboratory timing and control. *Review of Scientific Instruments*, 80(11):115103, 2009.
- [95] Bola S. Malek, Zachary Pagel, Xuejian Wu, and Holger Müller. Embedded control system for mobile atom interferometers. *Review of Scientific Instruments*, 90(7):073103, 2019.
- [96] A. Bertoldi, C.-H. Feng, H. Eneriz, M. Carey, D. S. Naik, J. Junca, X. Zou, D. O. Sabulsky, B. Canuel, P. Bouyer, and M. Prevedelli. A control hardware based on a field programmable gate array for experiments in atomic physics. *Review of Scientific Instruments*, 91(3):033203, 2020.
- [97] Elia Perego, Marco Pomponio, Amelia Detti, Lucia Duca, Carlo Sias, and Claudio E. Calosso. A scalable hardware and software control apparatus for experiments with hybrid quantum systems. *Review of Scientific Instruments*, 89(11):113116, 2018.
- [98] Sean Donnellan, Ian R. Hill, William Bowden, and Richard Hobson. A scalable arbitrary waveform generator for atomic physics experiments based on field-programmable gate array technology. *Review of Scientific Instruments*, 90(4):043101, 2019.
- [99] Aviv Keshet and Wolfgang Ketterle. A distributed, graphical user interface based, computer control system for atomic physics experiments. *Review of Scientific Instruments*, 84(1):015105, 2013.
- [100] Woongryol Lee, Mikyung Park, Seongheon Seo, and Hyungshin Kim. New design approach of fpga based control system and implementation result in kstar. *Fusion Engineering and Design*, 88(6):1338 – 1341, 2013. Proceedings of the 27th Symposium On Fusion Technology (SOFT-27); Liège, Belgium, September 24-28, 2012.

- [101] Paweł Kulik, Grzegorz Kasprowicz, and Michał Gaska. Driver module for quantum computer experiments: Kasli. In *Photonics Applications in Astronomy, Communications, Industry, and High-Energy Physics Experiments 2018*, volume 10808, page 1080845. International Society for Optics and Photonics.
- [102] Xilinx. UG1144 petalinux tools documentation. [https://www.xilinx.com/support/documentation/sw\\_manuals/xilinx2020\\_2/ug1144-petalinux-tools-reference-guide.pdf](https://www.xilinx.com/support/documentation/sw_manuals/xilinx2020_2/ug1144-petalinux-tools-reference-guide.pdf), 2020, accessed January 28, 2021.
- [103] Yocto Project. Open source embedded linux build system package metadata and sdk generator. <https://www.yoctoproject.org/>, 2020, accessed January 28, 2021.
- [104] Tao Xue, Hongming Li, Guanghua Gong, and Jianmin Li. Design of epics ioc based on rain1000z1 zynq module\*. *Proceedings of ICALEPCS2015, Melbourne, Australia*, 2015.
- [105] Sangil Lee, Changwook Son, and Hyojae Jang. Distributed and parallel real-time control system equipped fpga-zynq and epics middleware. pages 1–4, 06 2016.
- [106] Xilinx. PYNQ python productivity for zynq. <https://github.com/xilinx/pynq>, accessed January 26, 2021.
- [107] Avnet. Microzed documentation. <http://zedboard.org/support/documentation/1519>, accessed January 26, 2021.
- [108] Xilinx. Document DS190, XC7000 series datasheet. [https://www.xilinx.com/support/documentation/data\\_sheets/ds190-Zynq-7000-Overview.pdf](https://www.xilinx.com/support/documentation/data_sheets/ds190-Zynq-7000-Overview.pdf), 2018, accessed January 26, 2021.
- [109] Analog Devices. ADCMP552 datasheet. [https://www.analog.com/media/en/technical-documentation/data-sheets/ADCMP551\\_552\\_553.pdf](https://www.analog.com/media/en/technical-documentation/data-sheets/ADCMP551_552_553.pdf), accessed February 3, 2021.
- [110] Torex. XCL214 datasheet. <https://www.torexsemi.com/file/xcl213/XCL213-XCL214.pdf>, accessed February 2, 2021.
- [111] ST Microelectronics. STM6779 supervisor datasheet. <https://www.st.com/resource/en/datasheet/stm6720.pdf>, 2020, accessed January 28, 2021.
- [112] Xilinx. Zynq-7000 SoC datasheet. page 8, [https://www.xilinx.com/support/documentation/data\\_sheets/ds187-XC7Z010-XC7Z020-Data-Sheet.pdf](https://www.xilinx.com/support/documentation/data_sheets/ds187-XC7Z010-XC7Z020-Data-Sheet.pdf), 2020, accessed January 28, 2021.
- [113] Texas Instruments. SN74S244DWG4 datasheet. <https://www.ti.com/lit/ds/symlink/sn74s244.pdf>, 2016, accessed January 26, 2021.

- [114] Xilinx. Xilinx user guide UG471 ver 1.10. [https://www.xilinx.com/support/documentation/user\\_guides/ug471\\_7Series\\_SelectIO.pdf](https://www.xilinx.com/support/documentation/user_guides/ug471_7Series_SelectIO.pdf), 2018, accessed January 26, 2021.
- [115] Kicad. PCB calculator user manual. [https://docs.kicad.org/5.1/en/pcb\\_calculator/pcb\\_calculator.html](https://docs.kicad.org/5.1/en/pcb_calculator/pcb_calculator.html), 2019, accessed January 26, 2021.
- [116] B. M. Oliver. Time Domain Reflectometry. *HP Journal*, 15(6), 1964.
- [117] Ivan Idris. *Learning NumPy Array*. Packt Publishing, 2014.
- [118] SpinCore. Pulseblaster manual. page 27, [http://spincore.com/CD/PulseBlaster/PCI/PB24/PB\\_Manual.pdf](http://spincore.com/CD/PulseBlaster/PCI/PB24/PB_Manual.pdf), 2020, accessed January 28, 2021.
- [119] G. H. Mealy. A method for synthesizing sequential circuits. *The Bell System Technical Journal*, 34(5):1045–1079, 1955.
- [120] Edward F. Moore. Gedanken-experiments on sequential machines. In Claude Shannon and John McCarthy, editors, *Automata Studies*, pages 129–153. Princeton University Press, Princeton, NJ, 1956.
- [121] Kenneth Earl Wright II. *Manipulation of the Quantum Motion of Trapped Atomic Ions via Stimulated Raman Transitions*. PhD thesis, University of Maryland, 2017.
- [122] JQI. Jqi automation for experiments (jane). <https://github.com/JQIamo/jane>, 2021, accessed January 26, 2021.
- [123] C.J. Foot and D.P.C.J. Foot. *Atomic Physics*. Oxford Master Series in Physics. OUP Oxford, 2005.
- [124] Klaus Hueck, Niclas Luick, Lennart Sobirey, Jonas Siegl, Thomas Lompe, Henning Moritz, Logan W. Clark, and Cheng Chin. Calibrating high intensity absorption imaging of ultracold atoms. *Opt. Express*, 25(8):8670–8679, Apr 2017.
- [125] W. Ketterle, D. S. Durfee, and D. M. Stamper-kurn. Making, probing and understanding bose-einstein condensates. In *PROCEEDINGS OF THE INTERNATIONAL SCHOOL OF PHYSICS "ENRICO FERMI", COURSE CXL, EDITED BY M. INGUSCIO, S. STRINGARI AND C.E. WIEMAN (IOS)*, page 67. Press, 1999.
- [126] S. Nagel. *Ultracold Collisions in Atomic Strontium*. PhD thesis, Rice University, Houston, TX, 2008.
- [127] D. S. Barker, E. B. Norrgard, J. Scherschligt, J. A. Fedchak, and S. Eckel. Light-induced atomic desorption of lithium. *Physical Review A*, 98:043412, 2018.

- [128] E. B. Norrgard, D. S. Barker, J. A. Fedchak, N. Klimov, J. Scherschligt, and S. P. Eckel. Note: A 3D-printed alkali metal dispenser. *Review of Scientific Instruments*, 89:056101, 2018.
- [129] S. Eckel, D. S. Barker, J. A. Fedchak, N. N. Klimov, E. Norrgard, J. Scherschligt, C. Makrides, and E. Tiesinga. Challenges to miniaturizing cold atom technology for deployable vacuum metrology. *Metrologia*, 55:S182, 2018.
- [130] J. Scherschligt, J. A. Fedchak, D. S. Barker, S. Eckel, N. Klimov, C. Makrides, and E. Tiesinga. Development of a new UHV/XHV pressure standard (cold atom vacuum standard). *Metrologia*, 54:S125, 2017.
- [131] A. Sitaram, P. K. Elgee, G. K. Campbell, N. N. Klimov, S. Eckel, and D. S. Barker. Confinement of an alkaline-earth element in a grating magneto-optical trap. *Review of Scientific Instruments*, 91(10):103202, 2020.
- [132] Liang Hu, Enlong Wang, Leonardo Salvi, Jonathan N Tinsley, Guglielmo M Tino, and Nicola Poli. Sr atom interferometry with the optical clock transition as a gravimeter and a gravity gradiometer. *Classical and Quantum Gravity*, 37(1):014001, nov 2019.
- [133] T. E. Parker. Invited Review Article: The uncertainty in the realization and dissemination of the SI second from a systems point of view. *Review of Scientific Instruments*, 83:021102, 2012.
- [134] K. I. Lee, J. A. Kim, H. R. Noh, and W. Jhe. Single-beam atom trap in a pyramidal and conical hollow mirror. *Optics Letters*, 21(15):1177, 1996.
- [135] William Bowden, Richard Hobson, Ian R. Hill, Alvise Vianello, Marco Schioppo, Alissa Silva, Helen S. Margolis, Patrick E.G. Baird, and Patrick Gill. A pyramid MOT with integrated optical cavities as a cold atom platform for an optical lattice clock. *Scientific Reports*, 9(1):1–9, 2019.
- [136] S. Pollock, J. P. Cotter, A. Laliotis, and E. A. Hinds. Integrated magneto-optical traps on a chip. *Optics Express*, 17(16):14109, 2009.
- [137] M. Vangeleyn, P. F. Griffin, E. Riis, and A. S. Arnold. Single-laser, one beam, tetrahedral magneto-optical trap. *Optics Express*, 17(16):13601, 2009.
- [138] M. Vangeleyn, P. F. Griffin, E. Riis, and A. S. Arnold. Laser cooling with a single laser beam and a planar diffractor. *Optics Letters*, 35(20):3453, 2010.
- [139] J. Lee, J. A. Grover, L. A. Orozco, and S. L. Rolston. Sub-Doppler cooling of neutral atoms in a grating magneto-optical trap. *J. Opt. Soc. Am. B*, 30(11):2869, 2013.
- [140] C. C. Nshii, M. Vangeleyn, J. P. Cotter, P. F. Griffin, E. A. Hinds, C. N. Ironside, P. See, A. G. Sinclair, E. Riis, and A. S. Arnold. A surface-patterned chip as a strong source of ultracold atoms for quantum technologies. *Nature Nanotechnology*, 8(5):321, 2013.

- [141] S. B. Koller, J. Grotti, St. Vogt, A. Al-Masoudi, S. Dörscher, S. Häfner, U. Sterr, and Ch. Lisdat. Transportable Optical Lattice Clock with  $7 \times 10^{-17}$  Uncertainty. *Physical Review Letters*, 118:073601, 2017.
- [142] Commercial fabrication facilities, equipment, materials or computational software are identified in this paper in order to adequately specify device fabrication, the experimental procedure and data analysis. Such identification is not intended to imply endorsement by the National Institute of Standards and Technology, nor is it intended to imply that the facility, equipment, material or software identified is necessarily the best available.
- [143] J. P. Cotter, J. P. McGilligan, P. F. Griffin, I. M. Rabey, K. Docherty, E. Riis, A. S. Arnold, and E. A. Hinds. Design and fabrication of diffractive atom chips for laser cooling and trapping. *Applied Physics B*, 122(6):172, 2016.
- [144] Kurt Richard Vogel. *Laser cooling on a narrow atomic transition and measurement of the two-body cold collision loss rate in a strontium magneto-optical trap*. PhD thesis, University of Colorado, 1999.
- [145] Xinye Xu, Thomas H. Loftus, John L. Hall, Alan Gallagher, and Jun Ye. Cooling and trapping of atomic strontium. *J. Opt. Soc. Am. B*, 20(5):968–976, May 2003.
- [146] Simon Stellmer, Meng Khoon Tey, Bo Huang, Rudolf Grimm, and Florian Schreck. Bose-einstein condensation of strontium. *Phys. Rev. Lett.*, 103:200401, Nov 2009.
- [147] David E. Fagnan, Jicheng Wang, Chenchong Zhu, Pavle Djuricanin, Bruce G. Klappauf, James L. Booth, and Kirk W. Madison. Observation of quantum diffractive collisions using shallow atomic traps. *Phys. Rev. A*, 80:022712, Aug 2009.
- [148] S. D. Gensemer, V. Sanchez-Villicana, K. Y. N. Tan, T. T. Grove, and P. L. Gould. Trap-loss collisions of  $^{85}\text{Rb}$  and  $^{87}\text{Rb}$  : dependence on trap parameters. *Phys. Rev. A*, 56:4055–4063, Nov 1997.
- [149] Y. N. Martinez de Escobar, P. G. Mickelson, M. Yan, B. J. DeSalvo, S. B. Nagel, and T. C. Killian. Bose-einstein condensation of  $^{84}\text{Sr}$ . *Phys. Rev. Lett.*, 103:200402, Nov 2009.
- [150] J. P. McGilligan, P. F. Griffin, E. Riis, and A. S. Arnold. Phase-space properties of magneto-optical traps utilising micro-fabricated gratings. *Opt. Express*, 23(7):8948, 2015.
- [151] Ole Kock, Wei He, Dariusz Świerad, Lyndsie Smith, Joshua Hughes, Kai Bongs, and Yeshpal Singh. Laser controlled atom source for optical clocks. *Scientific Reports*, 6(1):37321, Nov 2016.
- [152] Alexander Yulaev, Wenqi Zhu, Cheng Zhang, Daron A. Westly, Henri J. Lezec, Amit Agrawal, and Vladimir Aksyuk. Metasurface-Integrated Photonic Platform

- for Versatile Free-Space Beam Projection with Polarization Control. *ACS Photonics*, 6(11):2902–2909, 2019.
- [153] Sangsik Kim, Daron A. Westly, Brian J. Roxworthy, Qing Li, Alexander Yulaev, Kartik Srinivasan, and Vladimir A. Aksyuk. Photonic waveguide to free-space Gaussian beam extreme mode converter. *Light: Science and Applications*, 7(1), 2018.
- [154] E. Imhof, B. K. Stuhl, B. Kasch, B. Kroese, S. E. Olson, and M. B. Squires. Two-dimensional grating magneto-optical trap. *Physical Review A*, 96:033636, 2017.
- [155] Jason Hogan, David Johnson, and Mark Kasevich. Light-pulse atom interferometry. *Proc. Int. School Phys. Enrico Fermi*, 168, 07 2008.
- [156] G. Tino, Luigi Cacciapuoti, Kai Bongs, Christian Bordé, Philippe Bouyer, Hansjoerg Dittus, Wolfgang Ertmer, Axel Görlitz, M. Inguscio, Arnaud Landragin, Pierre Lemonde, C. Lammerzahl, A. Peters, E. Rasel, Jakob Reichel, C. Salomon, Stephan Schiller, W. Schleich, K. Sengstock, and Martin Wilkens. Atom interferometers and optical atomic clocks: New quantum sensors for fundamental physics experiments in space. *Nuclear Physics B - Proceedings Supplements*, 166:159–165, 04 2007.
- [157] Juan A. Muniz, Matthew A. Norcia, Julia R. K. Cline, and James K. Thompson. A robust narrow-line magneto-optical trap using adiabatic transfer, 2018.
- [158] S. Snigirev, A. J. Park, A. Heinz, I. Bloch, and S. Blatt. Fast and dense magneto-optical traps for strontium. *Phys. Rev. A*, 99:063421, Jun 2019.
- [159] J. Dalibard and C. Cohen-Tannoudji. Dressed-atom approach to atomic motion in laser light: the dipole force revisited. *J. Opt. Soc. Am. B*, 2(11):1707–1720, Nov 1985.
- [160] D. J. Heinzen and D. J. Wineland. Quantum-limited cooling and detection of radio-frequency oscillations by laser-cooled ions. *Phys. Rev. A*, 42:2977–2994, Sep 1990.
- [161] Peter Horak, Gerald Hechenblaikner, Klaus M. Gheri, Herwig Stecher, and Helmut Ritsch. Cavity-induced atom cooling in the strong coupling regime. *Phys. Rev. Lett.*, 79:4974–4977, Dec 1997.
- [162] Christopher Corder, Brian Arnold, Xiang Hua, and Harold Metcalf. Laser cooling without spontaneous emission using the bichromatic force. *J. Opt. Soc. Am. B*, 32(5):B75–B83, May 2015.
- [163] Christopher Corder, Brian Arnold, and Harold Metcalf. Laser cooling without spontaneous emission. *Phys. Rev. Lett.*, 114:043002, Jan 2015.
- [164] Matthew A Norcia, Julia R K Cline, John P Bartolotta, Murray J Holland, and James K Thompson. Narrow-line laser cooling by adiabatic transfer. *New Journal of Physics*, 20(2):023021, feb 2018.

- [165] John P. Bartolotta, Matthew A. Norcia, Julia R. K. Cline, James K. Thompson, and Murray J. Holland. Laser cooling by sawtooth-wave adiabatic passage. *Phys. Rev. A*, 98:023404, Aug 2018.
- [166] S. Bondza, C. Lisdat, S. Kroker, and T. Leopold. Two-color grating magneto-optical trap for narrow-line laser cooling. *Phys. Rev. Applied*, 17:044002, Apr 2022.
- [167] John P. Bartolotta and Murray J. Holland. Sawtooth-wave adiabatic passage in a magneto-optical trap. *Phys. Rev. A*, 101:053434, May 2020.
- [168] DSB and Z. Smith. JQIamo/bipolar-mosfet-board: External Componentes and Bugfixes, July 2019.
- [169] Thomas Wilkason, Megan Nantel, Jan Rudolph, Yijun Jiang, Benjamin E. Garber, Hunter Swan, Samuel P. Carman, Mahiro Abe, and Jason M. Hogan. Atom interferometry with floquet atom optics, 2022.
- [170] Mauro Chiarotti, Jonathan N. Tinsley, Satvika Bandrupally, Shamaila Manzoor, Michele Sacco, Leonardo Salvi, and Nicola Poli. Practical limits for large-momentum-transfer clock atom interferometers, 2022.
- [171] Jan Rudolph, Thomas Wilkason, Megan Nantel, Hunter Swan, Connor M. Holland, Yijun Jiang, Benjamin E. Garber, Samuel P. Carman, and Jason M. Hogan. Large momentum transfer clock atom interferometry on the 689 nm intercombination line of strontium. *Phys. Rev. Lett.*, 124:083604, Feb 2020.